Capture into mean motion resonance

Kaltrina Kajtazi

Lund Observatory
Lund University

2021-EXA186

Degree project of 60 higher education credits (for a degree of Master)
September 2021

Supervisor: Antoine Petit

Lund Observatory
Box 43
SE-221 00 Lund
Sweden

Abstract

Orbital or mean motion resonance (MMR) occurs when the orbital period ratio between two planets is close to a ratio of small integers. MMR can protect planets from collisions and affects the overall final architecture of the system. Observations of exoplanets have shown that the survival rate of MMR-chains is low, and most systems are near and just wide of an exact MMR. The most common chains are the 2:1 and 3:2 first order mean motion resonances. Theoretical studies have shown that it is easy to capture planets into MMR when considering convergent migration, a natural consequence of planet-disk interactions that leads to MMR capture. However, there are discrepancies when it comes to the survival rate. The first step is to better understand capture into MMR. In this project, we aim to investigate which and how, orbital initial conditions and migration parameters affect capture into MMR. Having a better view of the full parameter space and its effects, one can better constrain theoretical models. Which together with the already known aspects of resonance instabilities could be enough to correctly reproduce observations in the future.

In order to study each parameter, I conducted N-body integrations with Rebound on a planar three body system, with varied initial conditions of orbital, planetary and migration parameters. Firstly, in a controlled setting of constant damping timescales, then using a realistic prescription of planetary migration, Type I.

During this project I have seen that when varying both planetary mass and damping timescale of the semi-major axis, there is a dependency on mass for capture into MMR. These results confirmed that smaller planetary mass usually results in MMR with smaller separation. Moreover, the damping timescale can alter this; longer damping timescale leads to capture into the first encountered MMR. Whereas planets with short damping timescale cross multiple MMRs before settling into a tighter spaced MMR or becoming unstable. For the Type I migration setting, I find that capture into MMR has no dependency in planetary mass for larger planetary mass and initial surface density. For the largest masses there is no capture into MMR. However, capture into MMR depends on the initial surface density; larger values correspond to faster migration rate and capture into MMR with smaller separation, and more systems in the chaotic zone of overlapping resonances.

Furthermore, the numerical results agree with the previously derived analytical prescription, which determines if a capture is possible. The analytical criterion gives a slightly steeper dependency on planetary mass, than what numerical results here show for both constant and Type I migration.

Popular science summary

Astronomy, the study of the most fascinating aspects of our existence that goes back thousands of years, has constantly provided clues to the big questions such as where everything started from and our place in the universe. Over time Astronomy has evolved tremendously through countless contributions from different scientists. For example Tycho Brahe, Galileo Galilei and Johanes Kepler were the first ones to conduct and document scientific and detailed observations of the solar system. The latter formulated the famous three laws of planetary motion, paving the path for Newton's gravitational theory. Just to name a few pioniers of dynamics, a branch of astronomy that is important whenever one wants to investigate the evolution of a system whether it is planets, as studied in this project, or any other astronomical object.

Today we know that our solar system, however special, is only one of many planetary systems. Statistical studies of observations have shown that every Sun-like star in our galaxy is likely to host at least one planet of different compositions and sizes, some with perhaps good conditions for life. Planets are formed in a rather flat disk of leftover material from the formation of the star. Through different processes this material is assembled into planets, and the main force involved in further evolution is gravity. It is gravitational attraction from the star that bounds the planets in the elliptical orbits that they move along, also known as Keplerian motion. A period is the time it takes to complete one turn around the star on such an orbit. Beside the star, a planet feels the gravity from the other planets in the system. Moreover, it is gravitational interactions between a planet and the gas in the disk that make a planet migrate. A natural consequence of such interactions and vital for the phenomena of mean motion resonance that this project investigates.

Mean motion resonance (MMR) occurs when the orbital period ratio of two planets is a ratio of small integers. For example, the 2:1 MMR means the planet closer to the star finishes two periods while the planet further away finishes one. Which always moves around the star at a slower rate, because the gravitational attraction from the star weakens with distance.

Since planetary migration is a natural consequence of planet-disk interactions, theory leads us to believe that it is easy to capture planets into MMR. Theoretical studies produce higher percentage of systems in MMR then observations do. Out of the many planets detected around other stars, only roughly 5% are in MMR. This discrepency and the low survival rate is yet to be fully understood. This project will attempt to shed some light on the matter, by looking into what can affect MMR capture using numerical simulations of orbital evolution. For example, using constant evolution timescales we see that smaller mass planets are captured into MMR with smaller separation. Such a configuration can be less stable and may not survive. When using Type I, a realistic migration prescription, I show that for high initial surface density of the disk gas migration is fast, and the planets are again captured into a MMR with smaller separation. Although, capture into MMR does in this case not depend on planetary mass when the mass is large, contradicting the previously derived analytical prescription used to determine when capture occurs.

Acknowledgements

I would like to start by thanking my supervisor Antoine Petit, for all his help throughout the project, and all the science I have learned from you all this time. It has been a pleasure to work with someone very knowledgeable in the field and in computational aspects. It has been easy to communicate and receive help when needed. But at the same time have room to study both theory and numerical aspects on my own to be more independent.

I also want to heartly thank my family for all the support during this one-year long project filled with ups and downs: Fun science that I have wanted to do since early childhood and really enjoyed, while batteling health struggles especially in times of a pandemic.

Lastly, thank you to my friends who have helped by being audience to my practice defense seminars, giving feedback and for any tips they have shared from own experience.

Contents

List of Figures

List of Tables

Chapter 1 - Introduction

The existence of resonances, commensurate motion between two objects, and their importance in the evolution of a planetary system has been known for many decades. The interest to study mean motion resonances between adjacent planets, the simplest type of resonance and the focus of this thesis, increased when the first exoplanets were discovered[1]. Today there are over 4000 discovered exoplanets, many in multiplanetary systems, with an occurrence rate of on average at least one planet per star Petigura et al. (2018); Zhu and Dong (2021).

Planets are complex and intriguing astronomical objects with enough mass to sustain self-gravity and reach hydrostatic equilibrium[2], but not massive or warm enough to ignite nuclear fusion. The International Astronomical Union's scientific definition of a planet from 2006 states; the object must also have cleared its closest surroundings and orbit around a common center of mass with its host star, which due to the large difference in mass usually resides near or inside the star, to be called a planet (Sarma et al., 2006). Objects too small to be able to clear their neighbourhood are called dwarf planets. Whereas those objects that fulfill the other criteria but do not orbit a star, due to for example ejection, are called rogue planets. The three main types of planets are:

- Terrestrial or rocky like Earth, with the main layers being a rocky core, a mantle and a crust.
- Gas giants like Jupiter, big planets with no crust.
- Ice giants like Uranus, with a large water fraction.

In this project the interest is only in planets (not distinguished by type) orbiting a star and embedded in the protoplanetary disk. Such a disk surrounds the host star, contains the building blocks of planets and is important for the evolution of the system. Moreover, only the early stages of evolution will be investigated in order to study capture into mean motion resonance and the effects of initial conditions. While investigations of long-term evolution and how such chains break is left for a future project.

The mean motion corresponds to the orbital frequency; the angular frequency it takes to fulfill one orbit in absence of any perturbations (Morbidelli, 2002). Mean motion resonance,

---

[1] The first detected exoplanets, in 1992, orbit the pulsar PSR 1257+12 (Wolszczan and Frail, 1992).

[2] Hydrostatic equilibrium in simple terms means nearly round shape as opposed to for example asteroids, which have shapes that resemble big rocks rather than nearly spheres as planets do.

MMR, means commensurable orbital periods, with a period ratio of small integers between two adjacent planets. Gravitational interactions between the planets cause perturbations to the mean motion which add up when in MMR, causing angular momentum and energy exchange that changes the orbital elements, which in turn makes the system exit the exact MMR. However, when the circumstances are favourable the resonance can stabilize while librating around a fixed point (Morbidelli, 2002). For example, 2:1 is the outermost first order MMR, a commensurability where the inner planet finishes two full orbits while the outer finishes one; the ratio between the periods is then $2/1 = 2$. Mean motion resonance is an important aspect of a planetary system's evolution in terms of planetary dynamics. There are many examples of different types of resonances in our Solar system alone: Jupiter and Saturn that are near a 5:2 MMR, the three inner Galilean moons of Jupiter in 4:2:1 resonance and more examples among objects in the Kuiper- and the asteroid-belt (Armitage, 2020). Therefore, to fully understand planet evolution we must correctly represent MMR while using observations as a guideline for theoretical modeling.

Observations have provided many examples of multi-planetary systems outside the solar system, the most famous being the data from transit measurements by Kepler and K2.[3] The most commonly detected type of exoplanet is a super-Earth orbiting close to their host star, slightly smaller than Neptune in size and either rocky, gaseous or both (Fabrycky et al., 2012). Statistically it has been shown that one in three solar-type stars host such hot super-Earths often in multi-planetary systems (Fressin et al., 2013; Zhu and Dong, 2021). In general, larger planets are less abundant but increase in frequency with larger period and are strongly correlated to stellar metallicity. These planets have a wider range of eccentricities and a higher preference for exact MMR (Winn and Fabrycky, 2015; Petigura et al., 2018). Smaller planets are more common and often come in compact multi-planetary systems but have no significant correlation to stellar metallicity. The eccentricities of small planets come in a narrow range of small values, especially when in a multi-planetary system (Petigura et al., 2018; Zhu and Dong, 2021). Moreover, they seem to prefer near commensurability just wide of a MMR rather than exact, and are well aligned, as suggested by the theories of planetary formation in a protoplanetary disk (Mayor et al., 2011; Steffen, 2013; Winn and Fabrycky, 2015). However, for systems with large outer planets this is not always the case, because the large planet can excite the inner smaller planets away from alignment (Xuan and Wyatt, 2020). Those systems with low degree mutual inclinations also have a higher multiplicity of planets (Zhu et al., 2018). Moreover, from the Kepler data it is clear that the discovered multi-planetary systems are in general stable at low period ratios (Steffen, 2013).

In Fabrycky et al. (2014) the period ratios between planets in multi-planetary systems in the Kepler data were assembled into a histogram and discussed in detail. An updated version is shown in Figure 1.1, based on Petit (2019); Fabrycky et al. (2014). This shows

---

[3] Kepler and K2 are mission names of the NASA space telescope from 2009. K2 was a repurposed mission after a failure in the spacecraft. The space telescope uses the transit method, which detects planets that move between the observer and its host star, dimming the starlight with an amount depending on the size of the planet.

the frequency of systems in MMR, which has been shown to be low, and in most cases these systems lie near a MMR rather than exact commensurability. The peaks of the distribution are near the 2:1 and 3:2 MMR, making these two MMR-chains most common among exoplanets. Another feature is the cutoff after the 5:4 MMR, which suggests that there are very few systems in closer MMRs Winn and Fabrycky (2015).

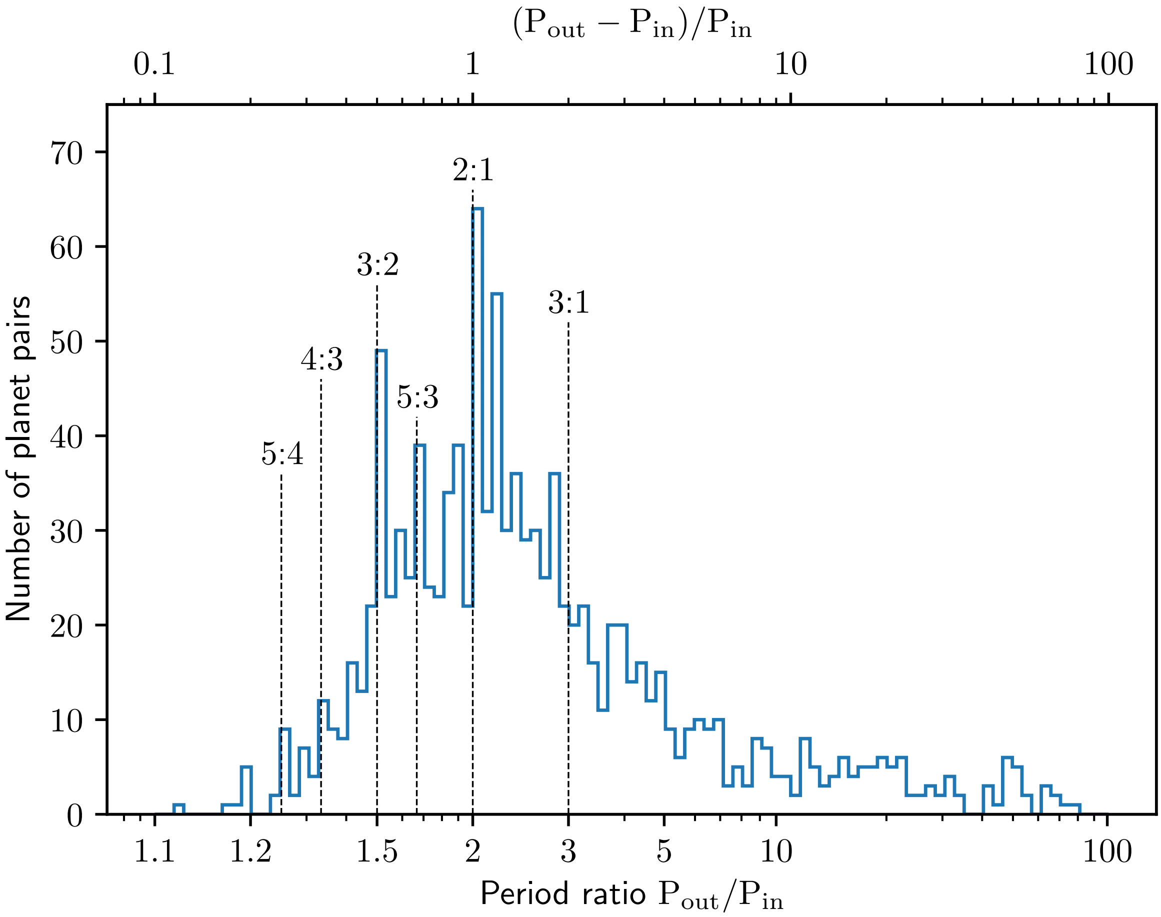

Figure 1.1: The frequency of multi-planetary systems in various period ratios. The data contains all confirmed planets provided by “The extrasolar planets encyclopedia” as of June 2021. The pileup of systems just wide of and the deficit just short of the exact commensurabilities are clearly visible. Moreover, most resonant systems are in 2:1 and 3:2 MMR. Same type of figure has been presented in other sources such as Fabrycky et al. (2014); Petit (2019).

In Fabrycky et al. (2014) they have also presented an important variable

$$\zeta_1 = 3\left(\mathrm{Round}\left[\frac{1}{\frac{P_2}{P_1}-1}\right] - \frac{1}{\frac{P_2}{P_1}-1}\right), \tag{1.1}$$

that indicates how close to an exact $k+1:k$ commensurability the systems observed are, based on the period ratio and resonance index k. Where P_1 and P_2 are the orbital periods of the inner and outer planet respectively. $\zeta_1 = 0$ refers to exact $k+1:k$ commensurability, beyond $\zeta_1 = \pm 1$ there are other MMRs, which we are not interested in for this thesis (Fabrycky et al., 2014). The region of interest is then the distribution closest to exact commensurabilities, around $\zeta_1 = 0$. Further away the system cannot be considered near a MMR anymore. A plot of ζ_1 is shown in Figure 1.2, a reproduction with the latest exoplanet data of the same figure from Fabrycky et al. (2014). One can clearly see the features of the observations as seen in Figure 1.1: The pileup of systems just wide of a MMR is visible at roughly $0 \gtrsim \zeta_1 < 0.25$, corresponding to values of period ratio slightly higher than that of exact MMR. The second feature is the deficit visible at roughly $-0.25 < \zeta_1 \lesssim 0$, corresponding to period ratios less than exact commensurability.

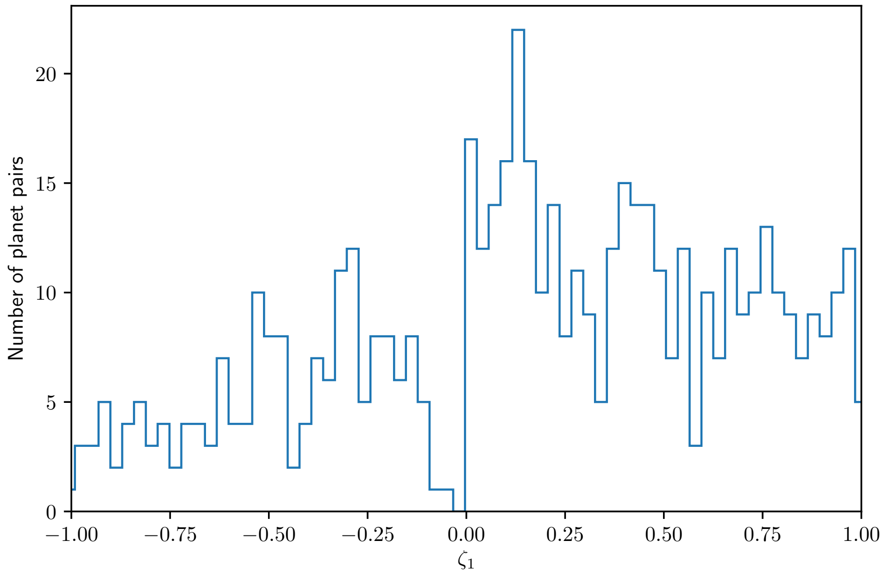

Figure 1.2: This figure with the latest data from "The extrasolar planets encyclopedia" and based on the work of Fabrycky et al. (2014), shows the frequency of systems wide of (positive ζ_1) and short of (negative ζ_1) a MMR. Here $\zeta_1 = 0$ indicates exact commensurabilities. Note that the equation has been flipped to represent the results in a more intuitive way, taking exact period ratio subtracted from actual period ratio. Thus, larger period ratio values mean positive ζ_1 instead of negative as in Fabrycky et al. (2014). This plot clearly shows that there is a pileup of systems at slightly higher values and a deficit at lower values than exact MMR.

These observations show that there are many systems near a MMR, however, many more are far away from a MMR. In theory planets form in protoplanetary disks, that surround the star. As the building blocks assemble into bigger bodies the interactions between the body and the disk gas become important. These gravitational interactions result in an exchange of energy and angular momentum which makes the body migrate: Inside the body's orbit the gas gives energy to it, while the portion outside the orbit extracts energy from it. The latter is usually more dominant resulting in a net loss of energy to the gas, thus the body migrates inwards towards the star. Such migration is vital for capture into a MMR. If the planets form and stay in the same place they can never be captured into a MMR. If they migrate away from each other, then again they cannot be captured into a MMR. The planets must thus migrate convergently in order to be possibly captured into any MMR (Tanaka and Ward, 2004; Cresswell and Nelson, 2008). The "migration leads to MMR"-model was first explored in detail by Goldreich and Sciama (1965), where they study the probability or preference for commensurability in the presence of migration effects. With this model in mind, looking at the observations it has been shown that only 5% of the systems are in or near a MMR, and so 95% of chains must break (Fabrycky et al., 2014). This low rate of MMR survival is not well-matched by theoretical studies.

There are two theoretical papers that study how migration leads to MMR Izidoro et al. (2017, 2019), by investigating the formation and evolution of super-Earth systems. In order to see the outcome of frequency, type of mean motion resonance and how this compares to observations. They confirm that these planets form and migrate during the disk lifetime, piling up and creating MMR-chains close to the inner disk edge. Moreover, they show that capturing planets into MMR with the use of the migration-model is easy. The systems enter MMRs early on and the instability that can break them permanently occurs right after disk removal, but does not affect all systems. Factors that can make a system more prone to instabilities were found to be: compact systems, less massive planets and a higher number of planets (Izidoro et al., 2017, 2019). The second paper, Izidoro et al. (2019), is an updated version of the same study, which investigates three different models of planet formation with different initial planet embryo separations, radial distribution and pebble flux[4]. This study gives a better match to observations for the population of systems that become unstable after disk removal, but not sufficient. Both papers conclude that most MMR-chains must break, and that the theoretical models do not reproduce the same percentage of MMR occurrence rate as seen in observations. This discrepancy between theory and observations has long puzzled scientists and shows what constraints existing formation/evolution models lack. The problem is that we cannot explain what could make the resonance chains break at such a high rate. One possibility is that migration or initial planetary/orbital parameters, that affect resonance capture and survival after disk removal, are not yet well understood.

There have been a few suggestions as to what could disrupt MMRs and lead to a pileup of systems just wide of a MMR. One longstanding explanation is tidal dissipation (Delisle et al., 2014). It is a mechanism that decreases the eccentricity, which when low enough

---

[4] Pebbles are building blocks for the planet embryos, which are created via pebble accretion (Lambrechts and Johansen, 2012).

causes increase in the period ratio in order to conserve angular momentum. As these effects continue hand in hand, the system soon leaves exact MMR for wider orbits. The efficiency of tidal dissipation depends on the distance to the star and is faster for rocky planets than gaseous. Moreover, tidal effects are usually dominated by the dissipation on the inner planet (Delisle et al., 2014). This suggests that the systems near a MMR are not cases where MMR has not been reached before disk dispersal, rather the planets may have been in a MMR before the dissipation came into play. Furthermore, in Delisle and Laskar (2018) it was shown that the distribution of MMRs depends strongly on the distance from the host star. The pileup of systems just wide of a resonance is only seen for cases where $P_1 < 5$ days. This together with the deficit at smaller ratios than exact MMR, suggests that tidal dissipation is the only mechanism that explains the distance dependence and the only theory necessary to explain the features of the observations as seen in Figure 1.1 (Delisle et al., 2014; Delisle and Laskar, 2018).

This project will set up different N-body numerical simulations with Rebound, an N-body package for orbital planetary evolution (Rein and Liu, 2012), to explore the parameter space and investigate which of these affect capture into MMR and how they do so. Studying the capture into MMR is the first step towards understanding the observed low survival rate of MMR-chains. For example, setting up a wide range of planetary mass relative to the central star shows which MMR each mass leads to, and which are most likely stable. In other works such as Ogihara and Kobayashi (2013); Deck and Batygin (2015), it has been shown that a small mass means the outer planet migrates closer to the inner planet before it is captured into a MMR. For a small mass to be captured at larger separation, meaning a more distant MMR, the damping timescale must be longer. Therefore, the damping timescale will also be investigated.

The parameter space will at first be investigated using constant damping timescales, a controlled setting, to carefully study the parameters one by one. A realistic migration prescription, Type I migration suited for the mass range chosen, is then introduced to study the parameter space with physical cases that compare to observations and see how the two settings compare. Together with comparison to analytical results and other numerical works, this project will show different outcomes of MMR and what they entail with respect to initial conditions: How capture into MMR is affected by each parameter, both physical properties of the system and parameters of migration, which are more important and how do they affect each other. From this it might be possible to explain why the most common MMR among exoplanets are 2:1 and 3:2, and why the frequency of exoplanets in MMR is so low as presented in Fabrycky et al. (2014).

Chapter 2 - Theory

2.1 Planetary Dynamics

Before presenting detailed theory on mean motion resonance, one must go further back and present the basic dynamics of a stellar system and its definitions. The motion of a system with two bodies, is presented by the equation of motion from Newtonian gravitational theory

$$\frac{d^2\mathbf{u}}{dt^2} = -\frac{G(m_0 + m_1)}{||\mathbf{u}||^3}\mathbf{u}, \tag{2.1}$$

written in the frame of common center of mass also known as the barycentric frame. Here $\mathbf{u} = \mathbf{u_1} - \mathbf{u_0}$ with the central body at position $\mathbf{u_0}$ and mass m_0, while m_1 denotes the mass of the secondary body, G is the gravitational constant and $||\mathbf{u}||$ is the norm of the vector $\mathbf{u}$. The equation gives the relative motion of two objects described as an elliptic, hyperbolic or parabolic orbit spanning a 2D plane in the 3D real space; in this thesis the orbit type considered is the elliptic only, as the other two are unbound orbits. Conventionally the central body is chosen to be the more massive object, for example the star, whereas the secondary body is the smaller mass, for example a planet. In the barycentric reference frame the star is roughly at the common center of mass due to its much larger mass, and the choice of central body does not change the equation of motion (Morbidelli, 2002). Moreover, Equation (2.1) has an exact solution that depends only on initial velocity and position, and it is a mathematical representation of Kepler's three laws of planetary motion to a good agreement, as shown in length in Danby (1962). Keplerian motion is given by the shape of the ellipse via orbital elements of the object around the primary body, as Kepler deduced by observing real planets in the Solar system (Kepler, 1609; Morbidelli, 2002; De Pater and Lissauer, 2015):

1. Planets orbit in ellipses with the star at one of the foci.
2. The areal speed[1] of a planet is constant if the star is taken to be at origin, due to angular momentum conservation.
3. The orbital period or time of one revolution, P, is related to the semi-major axis, a, as $P^2 = \frac{4\pi^2 a^3}{G(m_0+m_1)}$.

---

[1] Rate at which area is swept by the planet on its orbit

The third law shows that revolution speed decreases with increasing distance to the star, in agreement with the theory that the host star, the most massive body in the system, holds all other bodies bound via its gravity, a long-range force that weakens with distance.

The orbital elements are, as shown in image a) of Figure 2.1:

- Semi-major axis, a, the distance from the center to the edge of the ellipse along the longer axis.
- Eccentricity, e, the ratio between distance from one focus to the center of the ellipse, ae, and the semi-major axis.
- Pericenter is the closest point to the central body (at one of the focus points)
- Apocenter is the furthest point from the central body.

The names of the last two definitions differ if the star is the Sun or if one refers to the Moon and the Earth system, but the definitions are the same. Moreover, a circular orbit has its focus at the center, meaning the distance to the focus is zero, and therefore $e = 0$ means a circular orbit. Whereas, $e = 1$ denotes a collisional elliptical orbit, because the central body is then at the edge of the ellipse since $ae = a$. In other words the eccentricity indicates how deformed an orbit is.

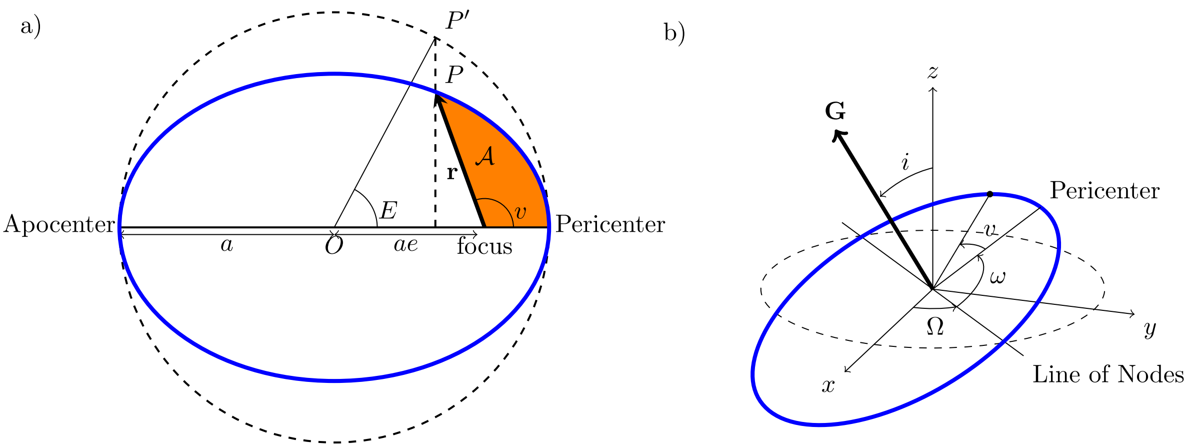

Figure 2.1: An illustration of a Keplerian orbit and its orientation in the real space, adapted from Petit (2019).

In Figure 2.1a) angle E, spanned by the body if in a circular orbit with the radius equal to the semi-major axis and tangent to the ellipse, evolves over time as

$$E - e\sin(E) = n(t - t_0) = M \tag{2.2}$$

$$n = \sqrt{G(m_0 + m_1)a^{-3}}, \tag{2.3}$$

where n is the mean motion and t_0 is the time for passage of the pericenter. This is known as the Kepler equation, a direct consequence of Kepler's second law, where the angle M corresponds to the area (the orange area in image a) of Figure 2.1) swept by the planet at a constant rate.

Now that we know the geometry of the orbit, the next step is to look at the position of the orbital plane in the real 3D space. For this one must introduce three other main angles. Firstly, i, the inclination of the orbit compared to the plane of a 3D coordinate reference frame, illustrated as a dashed ellipse in Figure 2.1 b), with origin at the central body. $i = 0$ means no inclination; the orbital plane is then the same as the plane of the reference frame. If $i \neq 0$ the orbit intersects the reference plane at two nodes and has a non-zero "z" component (the third coordinate axis of the reference frame), as indicated by the "Line of nodes" in the same image. The orbital plane is divided into two halves; the ascending node which refers to the part where the orbit intersects the reference plane while moving towards positive z, and the descending node where the orbit intersecting the reference plane for the second time while moving towards negative z direction (Morbidelli, 2002; De Pater and Lissauer, 2015). Secondly, the orientation or movement direction of the body is given by the angle Ω, which is called the longitude of ascending node and is determined by the position of the ascending node from the x-axis of the reference frame. Lastly, the argument of pericenter, ω, gives the orientation of the orbit in its plane and is determined as the angle between pericenter and the ascending node, see Figure 2.1 b).

All of these orbital elements are important when looking at any dynamics of a system, because they give the full position of the planet in real space. For example, when studying mean motion resonances one must visualize the change in semi-major axis due to migration, to determine if any resonances are encountered. Moreover, to study the parameter space and their impact on MMR capture one must know these elements and their definitions.

Furthermore, note that when $i = 0$ there is no line of nodes, since the orbit plane is the same as the reference plane, so no definition for ω or M exists. Moreover, when $e = 0$ there is no pericenter, the orbit is circular, the closest point equals the longest, so again M is not defined since there is no t_0. In order to include these two special cases naturally, one has introduced the pericenter longitude $\varpi = \omega + \Omega$ and mean longitude $\lambda = M + \omega + \Omega$, which are used in for example defining the resonance angles (Morbidelli, 2002).

Above the discussion has been on two-body systems. But in a multi-planetary system where MMR can exist, all the bodies in the system feel a gravitational force from the other bodies of the system too. Thus, the equation of motion changes to

$$\frac{d^2\mathbf{r_i}}{dt^2} = -\frac{G(m_0 + m_i)}{||\mathbf{r_i}||^3}\mathbf{r_i} + G\sum_{j=1,j\neq i}^{N} m_j \left(\frac{\mathbf{r_j} - \mathbf{r_i}}{||\mathbf{r_j} - \mathbf{r_i}||^3} - \frac{\mathbf{r_j}}{||\mathbf{r_j}||^3}\right), \tag{2.4}$$

which includes the impact from the star as in the two-body problem, and the forces from the other planets. Here the subscript i indicates the planet in question and j the other planets in the system. In the heliocentric frame the position vectors read as $r_{i,j} = u_{i,j} - u_0$ (Morbidelli, 2002). The first equation (2.1) simply gives the Keplerian motion; in the absence of perturbations the orbital elements are constant and M evolves linearly with time. In Equation (2.4), the other planets in the system cause perturbations in each other's Keplerian motion. Perturbations mean a very small change in the orbital elements with time, which can have a large impact over many orbits and cause deviation from Keplerian motion. The main perturbation from a body on another, which is important to consider in connection with MMR is shown in Figure 2.2. To the left of Figure 2.2 we see what happens to the orbital elements, where the semi-major axis and the eccentricity are changed and so the perturbed planet follows a new orbit. On the right image we see the macroscopic effects of the perturbation. That is, the orbit of the planet rotates continuously along the plane of motion (Morbidelli, 2002; De Pater and Lissauer, 2015). This is called precession of the orbital pericenter, which is given by the longitude of the pericenter. Perturbations will in general average out for the semi-major axis, while so-called secular perturbations will still cause orbital precession. Moreover, when the planets enter a MMR the perturbation due to the MMR will not allow averaging over a, instead the perturbations amplify.

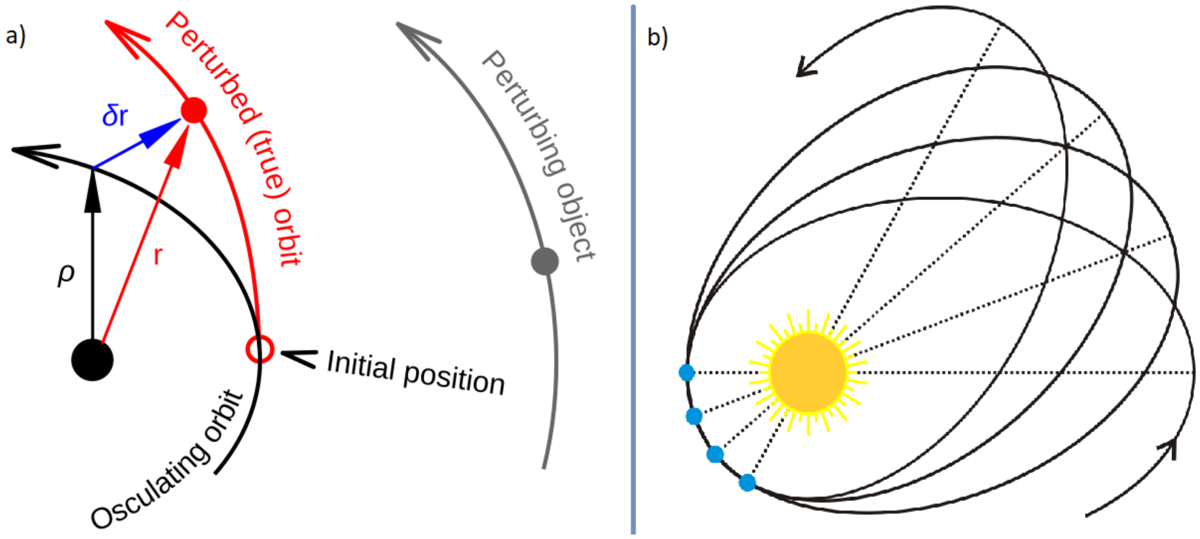

Figure 2.2: This figure shows the two main perturbations and their impact on a planet. Image a) shows the change in a and e causing the planet to follow a new ellipse as compared to the reference frame in black. Image b) shows the precession of the pericenter; the planet moves in a new ellipse in its plane for each revolution due to the rotation of the orbit. Source: Wikimedia Commons

The equations for the evolution of the orbital elements and by default the full motion of the planet, are to some extent intuitive but hard to work with. The three body problem cannot be solved analytically, but approximations such as the planar three-body problem, where all planets are aligned in the same plane, are useful in many cases. Otherwise, numerical integrations are the only way to properly study such systems and their dynamics in detail. Moreover, since this is a numerical study, analytical representations will not be treated. Nevertheless, there are many good sources on the topic and in connection to MMR, such as Morbidelli (2002); Ramos et al. (2015); Pichierri et al. (2018); Armitage (2020).

2.2 Mean motion resonance

In a multi-planetary system, gravitational perturbations between planets are negligible compared to the effects from the star. However, perturbations from other planets amplify when in a resonant configuration or if there are close encounters. Thus, making the perturbations non-negligible. The systems investigated here will be of two planets and a host star with no inclination, the planar three body problem approximation, and as such higher body MMR will not be addressed.

A system of two bodies is defined to be in a mean motion resonance when their period ratio is a ratio of small integers. The condition for MMR is given as

$$(k+q)n_1 - kn_2 \sim 0 \tag{2.5}$$

$$\text{or} \quad \frac{P_1}{P_2} = \frac{k+q}{k} \quad \text{and} \quad \frac{a_1}{a_2} = \left(\frac{k+q}{k}\right)^{2/3}, \tag{2.6}$$

where k, q are positive integers indicative of the commensurability order given as $k+q : k$, and P_1, P_2, a_1, a_2 are the periods and the semi-major axes of the inner and outer planet respectively. In this project the investigation focuses exclusively on first order mean motion resonances, for which $q = 1$. Moreover, k is also known as the resonance index, which is the number of revolutions of the outer planet around the host star (Morbidelli, 2002; Pichierri et al., 2018).

The resonance equation of motion can be approximated to only depend on the resonance angle for each planet

$$\theta_1 = (k+1)\lambda_1 - (k)\lambda_2 - \varpi_1 \tag{2.7}$$

$$\theta_2 = (k+1)\lambda_1 - (k)\lambda_2 - \varpi_2, \tag{2.8}$$

where λ_i is the mean longitude for respective planet and ϖ_i is the longitude of pericenter. In this form, where $q = 1$, the equation of θ holds for first order MMRs. The resonance angles track the motion of the planets via their mean longitudes, corrected with the longitude of the pericenter that takes into account the precession of the orbit introduced in Section 2.1. Because the precession is accounted for, the resonance angles are a good definition to identify MMR capture. The resonance angle would when plotted take all values between the full range 0 to 2π (circulate) when no resonance exists. Whereas when the system is in resonance, then θ oscillates slightly around the constant fixed value between 0 to 2π that corresponds to exact commensurability. If the resonance angle oscillates with large amplitude the MMR will break, at which point the angle again returns to take all values between $0 - 2\pi$. The oscillations of θ are due to the amplified perturbations which change the orbital elements, thus causing the system to exit and reenter exact commensurability. Oscillations (also called librations) occur on a timescale of their own, called the libration timescale. The timesacle is determined via the libration frequency of the resonance angle (Morbidelli, 2002; De Pater and Lissauer, 2015; Armitage, 2020).

Figure 2.3 shows the results of a numerical integration of the 2:1 MMR in the eccentricity and the semi-major axis plane. The gray lines are projections onto this plane of approximate analytical solutions of the motion of a resonant system, also called level curves. On these gray lines a quantity related to angular momentum is conserved, and the motion of the planets evolves along such a line. Therefore, motion in a MMR is parametrized by these level curves (Morbidelli, 2002; Ramos et al., 2015).

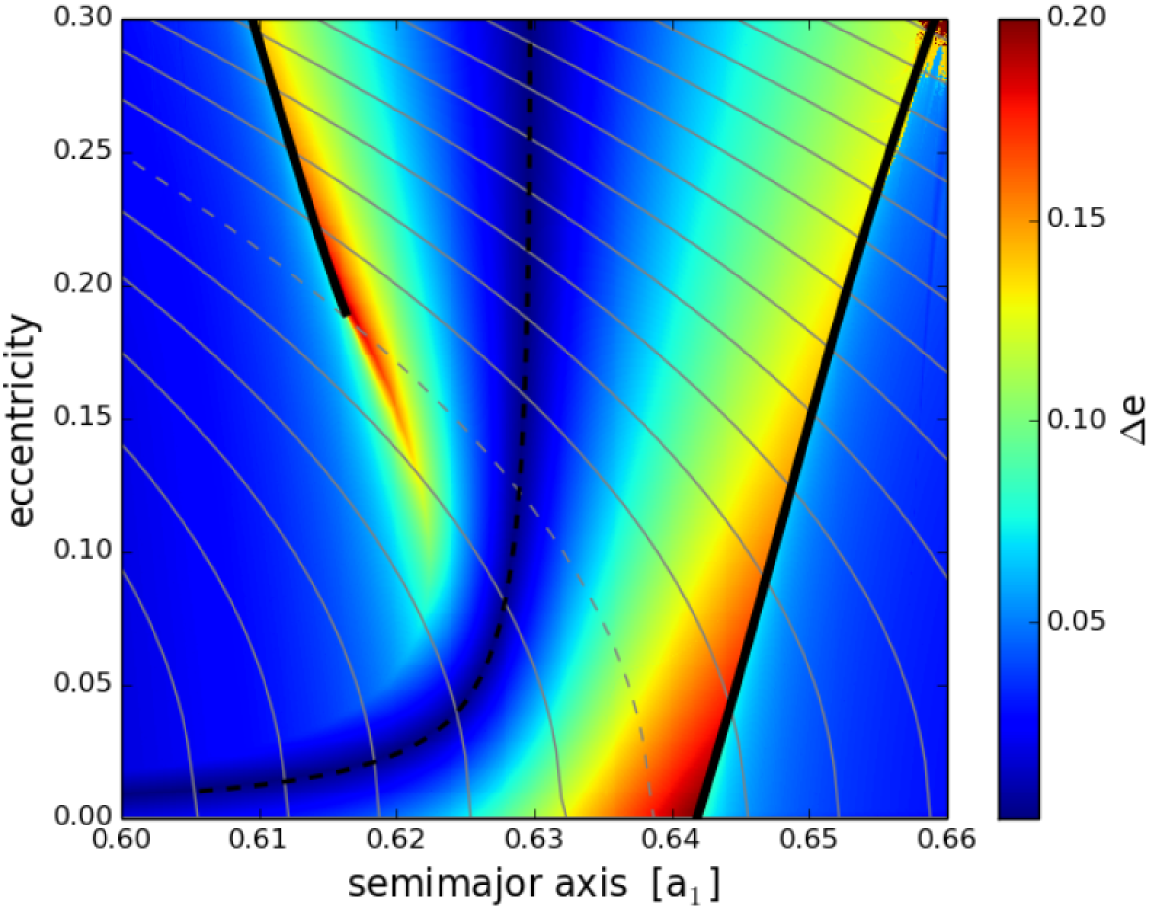

Figure 2.3: This figure illustrates the features of the outermost MMR, 2:1, in the (a, e) plane. The x-axis is given in units of the perturbed planets a, a_1. The shape of a MMR depends on the mass of the planet. Source: Ramos et al. (2015).

From the analytical model, which is an approximation to the full three body problem as shown in Figure 2.3 taken from Ramos et al. (2015), one can interpret a few more features of a MMR. Figure 2.3 is a stability map of a system with two Jupiter mass planets around the 2:1 MMR. The colour scale represents the maximum variation of eccentricity during the integration time, for a given initial semi-major axis and eccentricity. The dashed black line is the pericentric branch defined by the stable fixed points, around which the resonance angle oscillates when in resonance. The thick black lines are the inner and outer (the latter is located at lower a values and is shorter) separatrix stemming from the bifurcation point, the unstable fixed point at $\theta = \pi$ where it also connects to itself. The separatrix is first met at the dashed gray line, and so resonance capture can occur only for motion along level curves above this line. Thus, without the separatrix there is no resonance capture. The separatrix defines the MMR by separating the phase space into three regions; the inner and outer circulation regions and the libration region, whence the name. The outer circulation region corresponds to level curves below the critical line and below $e \sim 0.18$. The boundary is at the outer separatrix branch and no resonance can happen for an orbit out here. The inner circulation region corresponds to the level curves above the critical line and to the right of the inner separatrix branch where θ circulates. Again no resonance exists on orbits in this region. Resonance capture occurs only in the libration region inside the separatrix, see Figure 2.3. The separatrix spans the width of the libration region, also called the resonance width. The largest libration amplitude that still stays within the separatrix spans the full width (Morbidelli, 2002; Ramos et al., 2015; Deck and Batygin, 2015).

2.2.1 Resonance overlap

Earlier in this chapter it was said that motion occurs along the level curves of the approximate analytical model of resonant motion. However, in the presence of migration, which is a universal mechanism in planetary dynamics and vital for MMR capture (Goldreich and Sciama, 1965), as the planets converge they will move from one level curve to another. That is, a system can start motion at a level curve below or above the critical value (dashed gray curve in Figure 2.3) and move towards it, where the separatrix is first encountered and capture into the MMR can happen (Mustill and Wyatt, 2011; Batygin, 2015). Moreover, the distance along a level curve within the separatrix is the width of a MMR, see Figure 2.3.

The width of mean motion resonances increases with increasing resonance index. The reason being that the libration amplitude increases when the planets get closer, because the strength/impact of the perturbations increases as the periods and so the period ratio decreases. That is, the separation between the resonances shrinks with resonance index while the resonance width increases due to stronger libration. This combination causes the resonance regions to overlap between adjacent resonances as resonance index increases, creating a chaotic zone. In this zone the motion becomes chaotic, and the resonance soon breaks (Wisdom, 1986; Deck et al., 2013; De Pater and Lissauer, 2015). In many studies the width (half width, since the overlap surrounds the planet on both sides radially) has been shown to depend on the planet to star mass ratio

$$\epsilon_p = \frac{m_1 + m_2}{M_*}. \tag{2.9}$$

For a resonance index higher than $k_{overlap}$ defined as

$$k_{overlap} \sim 0.455 \epsilon_p^{-2/7}, \tag{2.10}$$

MMRs overlap. This point corresponds to a minimum period ratio and separation

$$\frac{P_2}{P_1} \lesssim 1 + 2.2\,(\epsilon_p)^{2/7}\,, \tag{2.11}$$

$$\frac{a_2 - a_1}{a_1} \lesssim 1.46\,(\epsilon_p)^{2/7}\,. \tag{2.12}$$

Equation 2.10 says that overlap occurs when the separation between two resonances is the same as the sum of half the width of both resonances (Wisdom, 1986; Deck et al., 2013). This criterion can be used to determine the stability of a MMR. Here it is used to define systems that fulfill the criterion, which are chaotic and unstable over time in their MMR. In order to find such a criterion for the overlap, one must determine the width of the resonance.

When overlap first appears it is weaker, and so the parts of a MMR region that overlap are the separatrix and outer parts of the resonance region. This region comprises higher libration amplitude orbits around the fixed point, which reach the separatrix. Only the centermost region of the resonance island can hold a system in stable resonance. However, more of the resonance width overlaps as the period ratio decreases or the resonance index increases further, until even the fixed point itself becomes unstable (Deck et al., 2013; Pichierri et al., 2018). At this point overlap dominates and no resonant orbits are available. The resonance index when that happens depends on the masses in the system (Deck et al., 2013; Ramos et al., 2015).

Furthermore, in Mustill and Wyatt (2012); Deck et al. (2013) the dependence of the structure of overlap on eccentricity, the planetary mass ratio and ϵ_p was investigated, showing that only e and ϵ_p have an effect: Larger values of ϵ_p means more extreme overlap and the stable regions of a resonant island are non-existent from the first period ratio that overlap appears, top panel of Figure 2.4. The resonance regions are more pronounced as the planetary mass is lower relative to the star. The same can be said for the eccentricity, as expected because the width of resonance increases with increasing ϵ_p and e (Deck et al., 2013; Ramos et al., 2015).

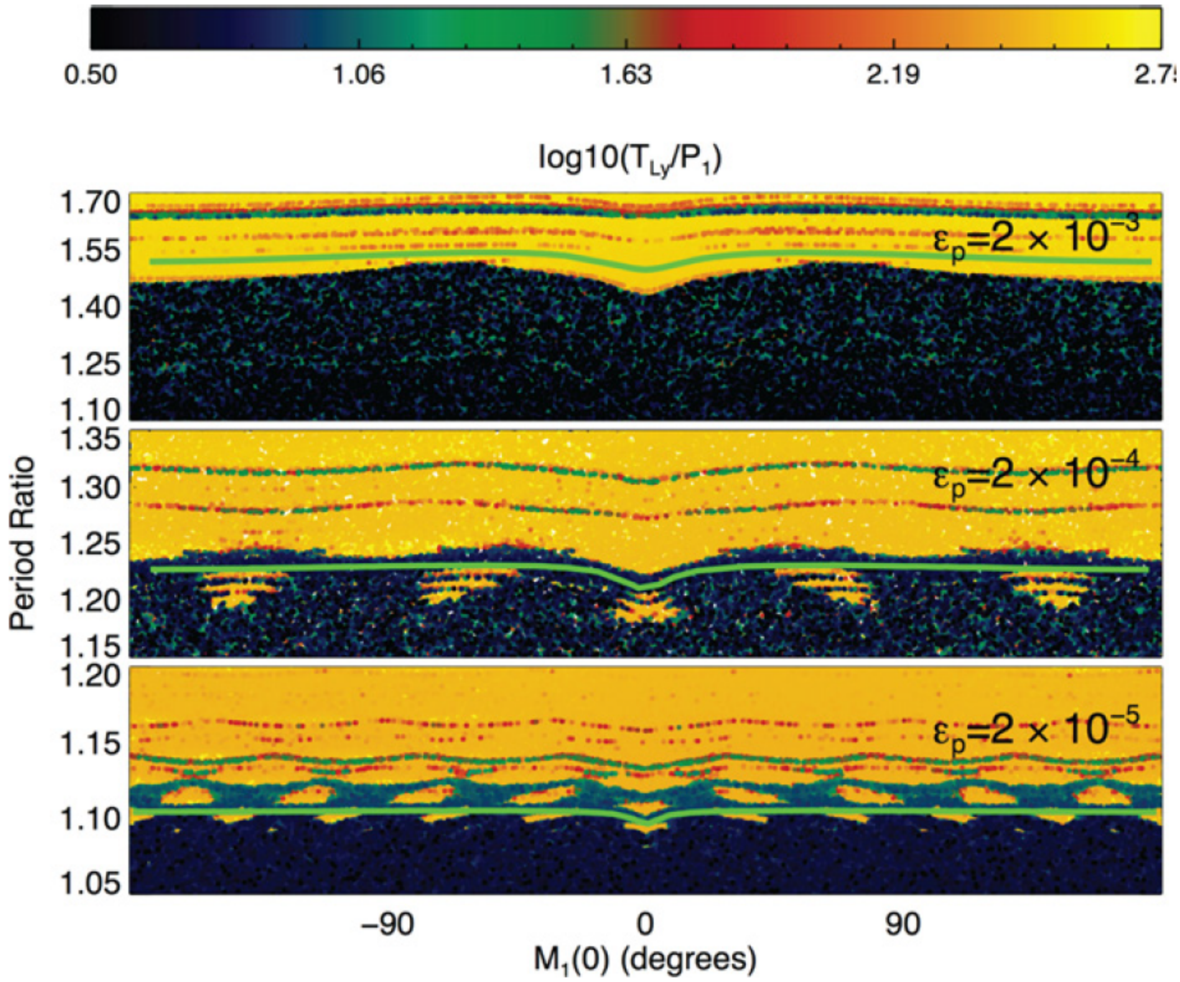

Figure 2.4: This figure shows the stable regions of the resonance island, in yellow, and the overlapping regions in blue. Period ratio on the y-axis, which shrinks with resonance index, and the mean anomaly, M_1, of the inner planet on the x-axis. Each panel is a different ϵ_p-value. The top panel shows a case of large ϵ_p where there are no resonant regions in the chaotic zone. Smaller ϵ_p (middle panel) shows that there are resonant orbits engulfed inside the chaotic zone. Moreover, such orbits are more pronounced for even smaller ϵ_p (bottom panel). Source: Deck et al. (2013)

In Deck et al. (2013) it was also shown that the overlap criterion is a better indicator of chaotic motion than the Hill criterion (Gladman, 1993). The latter says that a system is collisionally stable if it fulfills the Hill stability criterion: a separation larger than $2.4\epsilon_p^{1/3}$. The Hill stability limit is shown in Figure 2.4 as a green solid line. It turns out, there are initial conditions that can make a system chaotic due to overlap of resonances in a region where the system at the same time is Hill stable. For lower mass planets the chaotic zone stretches well into the Hill stability region. Thus, orbits at the edge of the overlap region can stay stable for a long time because they fulfill the Hill criterion despite being chaotic.

2.2.2 Adiabatic capture

Mean motion resonances affect the architecture of a planetary system, whether it is long-term stable or breaks. Moreover, the dissipative forces behind migration, play a close role with MMR in the dynamical evolution of a planetary system: without convergent migration, a natural consequence of planet-disk interactions, no capture into MMR can occur. If the planets' orbits diverge, no resonant configurations are likely to be established, even if the period ratio initially is less than 2 (Batygin and Morbidelli, 2013). Furthermore, MMR in turn can save a system from destruction, by locking the planets in a commensurability and preventing collisions. While in a MMR the planets have a closest approach distance which is smaller than it can be for planets not in a MMR while remaining stable (Pichierri et al., 2018). It is also worth noting that even a system in resonance can continue to migrate together. Thus, another mechanism must be involved in order to stop planet migration and prevent accretion onto the star (Cresswell and Nelson, 2008; Ramos et al., 2017; Ataiee and Kley, 2021).

As mentioned, when planets migrate they move from one level curve to another, approaching a MMR if migration is convergent. MMR is then reached for a critical value of such level curves presented as a dashed grey curve in Figure 2.3. Capture is thus possible above a critical value of eccentricity and inside the libration region, when the libration timescale, τ_{lib} found through the libration frequency of θ, is shorter than the time it takes to cross the resonance width due to migration. In such a case the migration is slow enough that the planet will not pass the resonant width and exit the resonant region before stable capture can happen (Batygin and Morbidelli, 2013; Batygin, 2015). This regime where migration is slow enough with respect to the resonance timescale is sometimes referred to as the adiabatic regime. The aspects of adiabatic capture into MMR, were investigated in detail in Batygin (2015). Their criterion for adiabatic capture is used in the results of this project to determine probability for capture; if the criterion is fulfilled capture is possible.

The criterion for adiabatic threshold needs only the libration timescale and migration timescale to determine if capture is possible given as

$$\frac{\tau_{lib}}{\Delta t} \approx \frac{P_2}{4}\frac{1}{\tau_a}\left(\frac{M_*}{m_1+m_2}\right)^{4/3}\frac{(k-1)^{-2/9}}{\left(\sqrt{3}|f_{res}^{(1)}|\right)^{4/3}} \leq 1, \tag{2.13}$$

from Batygin (2015). Here P_2 is the orbital period of the outer planet at capture and τ_a is the relative migration timescale between the two planets

$$\frac{1}{\tau_a} = \frac{1}{\tau_{a2}} - \frac{1}{\tau_{a1}}, \tag{2.14}$$

M_* is the central mass while $m_{1,2}$ is the mass of the respective planet and $f_{res}^{(1)}$ is a function of the resonance index

$$f_{fres}^{(1)} \approx -0.46 - 0.802k, \tag{2.15}$$

in approximate form from Deck et al. (2013). The criterion says: $\tau_{lib} \leq \Delta t \Rightarrow \tau_{lib}/\Delta t \leq 1$ for capture to occur, where Δt is the timescale to cross the resonance width due to migration.

If planets migrate faster past the resonance width than the libration rate, the system will not be captured in a MMR. However, it does not mean that no capture can occur at all. The planets can continue to migrate towards the star and be captured in a closer resonance, with smaller spacing. Because at smaller separation the libration timescale decreases, since librations increase due to stronger perturbations, thus matching the migration rate and eventually surpassing it. When that happens, depends on the parameters of the system and of the migration. Sometimes planets migrate through several MMRs before being captured into one. Moreover, the libration timescale decreases as the planets come closer to the star (or if the inner planet is fixed at inner disk edge, the closest it can be to the star). Thus, aiding the capture into MMRs even if the migration rate is fast. To some extent, the system being closer to the star, or the inner planet being fixed at the inner disk edge, should mean that such systems are more likely to be captured into a lower resonance index than planets starting further away but with the same initial parameters and migration rate.

We now know that planets migrate, possibly through many MMRs, until they are captured into one where the adiabatic condition $\tau_{lib}/\Delta t \lesssim 1$ is fulfilled. The adiabatic criterion gives important information about the behaviour of MMR capture. It can tell us if capture is possible for any set of given initial parameters and how each parameter is affected by the other ones included in the condition. Equation (2.13) takes into account the masses in the system and the timescale for the change of semi-major axis via migration (adiabatic criterion is not affected by eccentricity). Thus, for a given set of values of these parameters one can find out in which k a system is captured. To do so one must solve Equation (2.13) for k

$$k \gtrsim \left(\frac{P_2}{4}\frac{1}{\tau_a}\right)^{9/14}\left(\frac{1}{0.802\sqrt{3}}\right)^{6/7}\epsilon_p^{-6/7} \approx 0.31\left(\frac{P_2}{\tau_a}\right)^{9/14}\epsilon_p^{-6/7}, \tag{2.16}$$

where the parts related to k have been approximated further; $k-1 \approx k$ and $|f_{res}^{(1)}| \approx 0.802k$. Thereby, this rewriting indicates what to expect from numerical simulations when initial conditions are investigated. One can also solve the equation for ϵ_p

$$\epsilon_p \gtrsim \left(\frac{P_2}{4}\frac{1}{\tau_a}\right)^{3/4}\frac{(k-1)^{-1/6}}{\sqrt{3}|f_{res}^{(1)}|} \approx 0.25\left(\frac{P_2}{\tau_a}\right)^{3/4}k^{-7/6}, \tag{2.17}$$

which instead reveals how ϵ_p relates to τ_a and k. Thus, it can be plotted as a function of k for a given τ_a, together with numerical results to see if the two methods of studying MMR capture give the same results. Lastly, one can solve for τ_a

$$\tau_a \gtrsim \frac{P_2}{4}\left(\frac{1}{\epsilon_p}\right)^{4/3}\frac{(k-1)^{-2/9}}{(\sqrt{3}|f_{res}^{(1)}|)^{4/3}} \approx 0.16 P_2 \epsilon_p^{-4/3}k^{-14/9}, \tag{2.18}$$

to see how the migration timescale relates to ϵ_p and k, since this parameter is also investigated in this project. From these versions of the adiabatic condition we can expect the following behaviour: $k \propto \epsilon_p^{-6/7}\tau_a^{-9/14}$, $\epsilon_p \propto \tau_a^{-3/4}k^{-7/6}$ and $\tau_a \propto \epsilon_p^{-4/3}k^{-14/9}$.

2.3 Protoplanetary disk

The dominant theory of the origin of planets in our solar system starts with a disk around the Sun, believed to contain the building blocks of planets in an otherwise gaseous environment, called a protoplanetary disks or PPD. Such disks are observed around young stars, during the first 5-6 Myr of their evolution. Disks are detected and observed thanks to the excess of infrared flux coming from the dust surrounding the young star, also called YSO (young stellar objects). The slope of the spectral energy distribution (SED) is used to define the four classes of the first stages of a YSO. SED is a measurement of the flux of a light source as a function of wavelength in the infrared region (Lada, 1987). This section will, in short, explain the formation of disks and their nature for a complete context to the project, starting from the first step — molecular clouds. For more details on everything mentioned here and more refer to e.g. Armitage (2020).

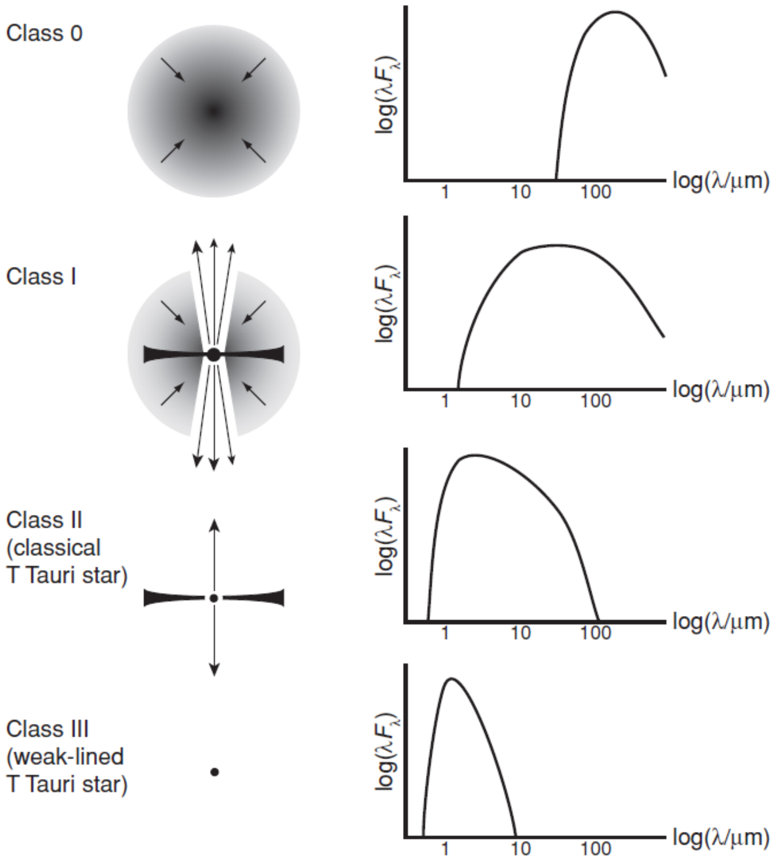

Figure 2.5: An illustration of the different YSO classes and their characteristic SED measurements. Source: Armitage (2010)

In star forming galaxies there are many inhomogeneous cold clouds of molecular gas in the interstellar medium, called molecular clouds. These clouds have denser regions, molecular cloud cores, where the gravity gradient is larger, which causes collapse of the gas into a protostar (Armitage, 2020). Moreover, since the cloud is inhomogeneous there is always a small-scale rotation, meaning non-zero angular momentum, which prevents the neighbouring more diffuse lower density gas from collapsing onto the dense center that is the protostar. Instead, this material surrounds the protostar as an optically thick rotating gas envelope that slowly falls into a disk shaped structure, with initial properties that are the same as the formation environment (De Pater and Lissauer, 2015). This is the first class of the early evolution of a YSO, Class 0 as shown in the top image of Figure 2.5. The SED here shows flux at long wavelengths only, the light that has been reprocessed by the gaseous envelope. In the Class I stage, light flux indicating a disk is first visible through openings in the envelope, which continues to fall in. The next stage, Class II, is when the envelope of gas has all been accreted onto the disk, as shown in the third image in Figure 2.5. SED measurements here show the sum of the radiation from the star and the infrared emission from the disk, together with excess of UV from hot gas accreting onto the star from the disk closest to it and mm flux from cold dust at the outer regions of the disk. The last stage of an YSO is Class III, where the disk has dissipated leaving only a young pre-main-sequence star, which on a Hertzsprung-Russell diagram would be above the main sequence with strong X-ray activity characteristic for a young star (Armitage, 2020). For this project the interest is in the Class II stage of YSOs, when the disk has fully formed but not dissipated and planets have had time to form.

The constraint on the lifetime of a PPD is mainly from measurements of the excess of IR-emission from the dust. Observations of clusters of young age, < 1 Myr, show a percentage of detected disks at almost 100%, whereas for older clusters it typically decreases to 50% and to zero for clusters 6Myr or older (Haisch et al., 2001). From these observations we can estimate that the lifetime of a disk is typically 3-5Myr, see figure 3.1 in Armitage (2020).

The mass of a disk is difficult to infer because most of the mass is molecular hydrogen, which cannot be directly observed. Other more indirect tracers are used, such as mm-continuum emission and deuterium, that can give an estimate of disk mass. Moreover, protoplanetary disks have in general been observed to be thin, the vertical density profile is determined by the hydrostatic balance between the pressure gradient and the vertical component of the stellar gravity. Thus, since the surface area of the disk is large enough to cool efficiently it results in a weaker pressure that cannot support gas against gravity at larger vertical distances. Therefore, the vertical distance, the thickness of the disk, is only a small fraction of the distance to the star radially. In other words disks have low aspect ratios ($\ll 1$), which is the ratio of the geometrical thickness or scale height to radius, and determines the shape of the disk over different radii (Armitage, 2010, 2020).

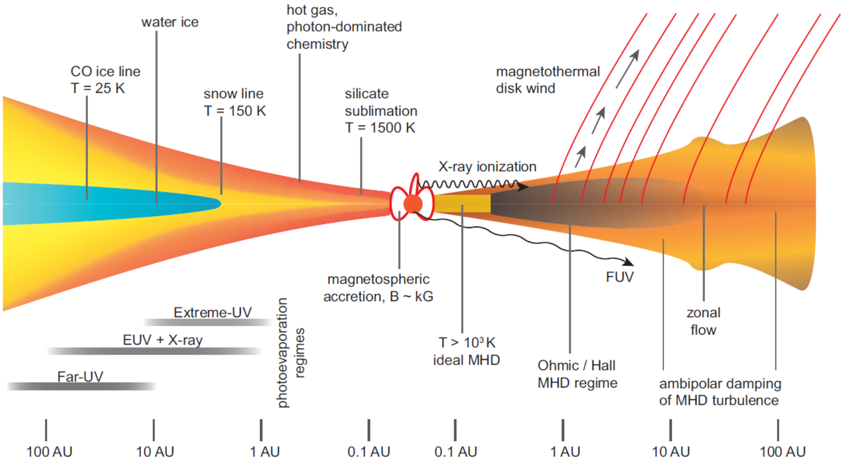

Figure 2.6: An illustration of the structure of a protoplanetary disk and transport of the angular momentum. Source: Armitage (2018)

The structure of a disk is complex with an inner edge at typically 0.1 AU and outer edge at roughly 30 AU for the most common analytical model, the Chiang-Goldreich model and a solar type star (Armitage, 2010; Brasser et al., 2018). At the inner disk edge the surface density is low and serves as a so-called planet trap, where migration stops at the inner disk edge or right before the edge is reached (Masset et al., 2006; Armitage, 2017; Brasser et al., 2018). A disk's radial surface density evolves smoothly over time via transport of angular momentum due to disk viscosity, with an efficiency parametrized by the Shakura-Sunyaev α-parameter, usually taken to be constant. The transport of angular momentum occurs as redistribution radially through the disk. That is, momentum is lost, which causes inwards motion and accretion onto the star, or momentum is gained causing outwards motion. Moreover, because global angular momentum must be conserved, when there is loss of momentum there must be gain of momentum elsewhere. However, the angular momentum can also be lost entirely from the disk via dispersion, ejection or exchange to a large body embedded in the disk, such as a planet (Armitage, 2017, 2020). The surface density and aspect ratio are given by

$$\Sigma = \Sigma_0 r^{-s}, \tag{2.19}$$

$$h = h_0 \left(\frac{r}{r_0} \right)^{\beta}, \tag{2.20}$$

where s gives the disk profile and β is the flaring index. In this project we choose to follow the same format as in Pichierri et al. (2018).

Lastly, disk dispersal is attributed to different heating mechanisms such as stellar radiation and, close to the star, accretion heating (dissipation of gravitational potential energy as gas accretes onto the star), which are the main processes in most disks (Armitage, 2010, 2018). See Figure 2.6 for a detailed illustration of disk structure and transport mechanics.

2.4 Type I migration

Planets migrate when they exchange angular momentum or energy with another object in a system through any process that enables this. The main mechanism that makes a planet migrate efficiently is migration through exchange of angular momentum with the gas in the protoplanetary disk due to gravitational interactions. There are two main types of such migration, Type I and Type II. The latter only holds for planets massive enough, Jupiter mass and larger, that open gaps in the disk. This project investigates capture into MMR for masses smaller than that, which do not disrupt the disk gas in long term, thus the only migration to consider is the Type I migration. Such migration can significantly change the orbital elements of a system, and thus also the final architecture.

Firstly, exchange of momentum with the gas in the disk causes either increase or decrease of the semi-major axis. For such an exchange to occur the surrounding disk must not be axisymmetric. The disk is not axisymmetric because the planet influences its vicinity through gravitational torques moving the gas particles, which causes the buildup of asymmetric so-called density wakes. These are two asymmetric waves inside and outside the orbit of the planet, with higher gas density than the rest of the disk around the planet. These in turn exert a torque on the planet, which is unequal in magnitude and opposite in sign due to conservation of total angular momentum (Goldreich and Tremaine, 1980; Ward, 1997). The gas both interior and exterior to the planetary orbit follows orbits resonant with the planet, which drive the density wakes. The interior portion of the resonant gas exerts a positive torque while the outer part exerts a negative torque (Goldreich and Tremaine, 1980; Armitage, 2020; McNally et al., 2020). Usually, the outer portion of the wave is dominant, resulting in a negative net torque; angular momentum is transferred from the planet to the gas, thus the planet will migrate inwards. Whereas when the opposite is true angular momentum is exchanged from the gas to the planet, increasing its energy and causing outwards movement (Goldreich and Tremaine, 1980; Armitage, 2018).

In Figure 2.7 one can see the overdensity wakes that are induced by the presence of a planet and driven by the resonant gas, for visualization.

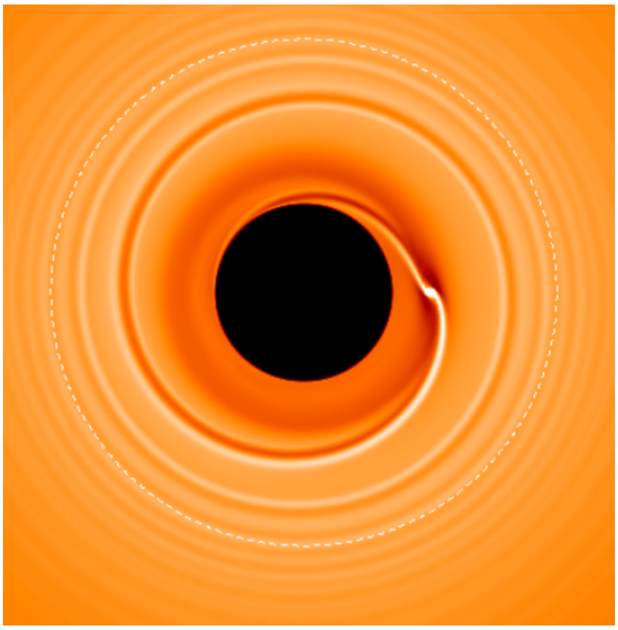

Figure 2.7: This figure is a numerical illustration of the density wakes, of higher gas density about the planet's orbit, that are responsible for the torques on the planet and thus Type I migration. Source: Armitage (2020)

This type of migration can cause changes in the eccentricity and inclination, which are both usually dampened no matter the direction of the migration and when the planet is embedded in the disk (Goldreich and Tremaine, 1980). Any type of migration, even Type I, where migration occurs due to interactions with the disk, will abruptly halt when there is no more disk, or the disk has been depleted so much that no efficient exchange of momentum can occur.

Planetary migration via interactions with the disk in such way as mentioned above, is important for planets/bodies roughly the mass of Mars and larger. Smaller bodies exert little to no torque on the disk, thus have negligible interaction with the disk gas. This also means that planetary migration is dependent on planetary mass (Ward, 1997; McNally et al., 2020). Thus, in a system of two planets with different masses, even if the difference is small, the planets will migrate at different rates. Moreover, because the torque on the planet depends on the distance to the gas and the availability of it, the timescale of such migration also depends on the surface density of the disk and on the position of the planet in the disk (Tanaka and Ward, 2004),

$$\tau_{wave} = \frac{M_*^2}{m\Sigma a^2}\frac{h^4}{n}. \tag{2.21}$$

How the orbital parameters of the planet then evolve also depends on the angular momentum transport in the disk, with viscosity parametrized by the viscous parameter α. The evolution of the parameters, not showing i since it is not used, were first introduced with similar expressions, in Goldreich and Tremaine (1980). In this project we follow Pichierri et al.

(2018) with similar τ_a and τ_e timescales

$$\tau_a = \frac{\tau_{mig}}{2} = \frac{\tau_{wave} h^{-2}}{2.7 + 1.1s} f_{ei,a}, \tag{2.22}$$

$$\tau_e = \frac{\tau_{wave}}{0.780} f_{ei,e}, \tag{2.23}$$

at which a and e respectively evolve. These timescale equations were also introduced in Ward (1997); Cresswell and Nelson (2008). Here $f_{ei,a}$ is a function containing the dependency on e and i for τ_a and $f_{ei,e}$ is the same type of function but for τ_e. The $f_{ei,e}$ and $f_{ei,a}$ functions are taken from Cresswell and Nelson and are defined in Section 3.1.1. Moreover, s is the exponent of the surface density of the disk. The inclination is set to zero in the investigations of this project, both because it is easier to simulate coplanar simulations, and because the planets under investigation are embedded in the PPD with no inclination. Moreover, the inclination is dampened over a short timescale under the effects of migration, as is the eccentricity. From here on the timescales for the change of orbital elements will be referred to as damping timescales, since we only consider inward migration.

Furthermore, because of the inverse dependency on the surface density one can directly say that the timescale of Type I migration is long for low surface densities and short for high surface densities. The typical timescales for Type I migration are shorter than the typical lifetime of a disk. This poses a problem because it means that planets migrating inwards can fall into the star if not halted by another mechanism (Tanaka and Ward, 2004; Masset et al., 2006; McNally et al., 2020). A way to stop this inwards migration catastrophe is the inner disk edge. At this point as mentioned in Section 2.3 the surface density of gas abruptly decreases to roughly zero. At this point a positive corotation torque kicks in, directing the planet outwards away from the inner disk edge and the star, a process referred to as a planet trap (Masset et al., 2006; Ataiee and Kley, 2021).

Furthermore, it is worth mentioning that in Deck and Batygin (2015) it was shown that e-damping can result in unstable capture, meaning MMRs are rare when there is damping of eccentricity, which is naturally part of planetary migration. A criterion for instability due to this aspect was given in Deck and Batygin (2015) in terms of ϵ_p. However, this criterion is not fulfilled in the context of the 2:1 MMR and comparable masses. In such case it says that all captures are stable and permanent, which can be false due to other aspects of MMR dynamics this criterion does not take into account.

As indicated throughout this section and previous, the migration prescription affects MMR capture as well as making it possible. For these reasons and others to follow, studies on migration and MMR such as this one, are of great importance for the communal study of planetary dynamics and system evolution.

2.4.1 Adiabatic condition and Type I migration

In Subsection 2.2.2 it was shown how the adiabatic criterion can be used to find in which k a system of any given values of ϵ_p and τ is captured. In other words, for which MMR the adiabatic criterion is fulfilled. This subsection presents the relations between those variables for systems undergoing Type I migration, using the Equations (2.16) through (2.18). When including Type I migration the expected behaviour differs, since the migration is no longer a constant value. The migration now depends on the planet mass and the mean motion of the planet. Thus, we need to first find the relative migration timescale of a damping, for Type I migration

$$\begin{aligned}\frac{1}{\tau_a} = \frac{1}{\tau_{a2}} - \frac{1}{\tau_{a1}} &= \frac{(2.7+1.1s)\Sigma m_2 a_2^2 n_2}{M_*^2 h^2} - \frac{(2.7+1.1s)\Sigma m_1 a_1^2 n_1}{M_*^2 h^2} \\ &= \frac{(2.7+1.1s)\Sigma}{M_*^2 h^2}\left(m_2 a_2^2 \sqrt{\frac{GM_*}{a_2^3}} - m_1 a_1^2 \sqrt{\frac{GM_*}{a_1^3}}\right) \\ &= \frac{(2.7+1.1s)\Sigma}{M_*^2 h^2}\sqrt{GM_* a_1}\left(m_2\left(\frac{k+1}{k}\right)^{1/3} - m_1\right),\end{aligned} \tag{2.24}$$

where $a_2 = ((k+1)/k)^{2/3} a_1$ and $n = \sqrt{GM_*/a^3}$ were used to simplify the equation. Note that since τ_a is now given by parameters, one can solve for specific migration parameters if desired, such as Σ. Moreover, to make it easier to solve for both k and ϵ_p, one can fix the inner planet at for example the inner disc edge, which means $1/\tau_a = 1/\tau_{a2} - 1/\inf = 1/\tau_{a2}$. Doing so we get a simpler version of $1/\tau_a$ to insert into Equation (2.16)

$$\begin{aligned}k &\gtrsim \left(\frac{P_2}{4}\frac{(2.7+1.1s)\Sigma m_2 a_2^2 n_2}{M_*^2 h^2}\right)^{9/14}\left(\frac{1}{\epsilon_p}\right)^{6/7}\left(\frac{1}{0.802\sqrt{3}}\right)^{6/7} \\ &= \left(\frac{\pi}{2}\frac{(2.7+1.1s)\Sigma a_2^2}{M_* h^2(1+\zeta)}\right)^{9/14}\left(\frac{1}{\epsilon_p}\right)^{3/14}\left(\frac{1}{0.802\sqrt{3}}\right)^{6/7},\end{aligned} \tag{2.25}$$

where $n_2 = 2\pi/P_2$ and $m_2 = \epsilon_p M_*/(1+\zeta)$ with $\zeta = m_1/m_2 = 1$ for equal mass planets. In the same manner we solve for ϵ_p and Σ

$$\begin{aligned}\epsilon_p &\gtrsim \left(\frac{P_2}{4}\frac{(2.7+1.1s)\Sigma m_2 a_2^2 n_2}{M_*^2 h^2}\right)^{3/4}\frac{(k-1)^{-1/6}}{\sqrt{3}|f_{res}^{(1)}|} \\ &= \left(\frac{2\pi}{4}\frac{(2.7+1.1s)\Sigma a_2^2}{M_* h^2(1+\zeta)}\right)^{3}\frac{(k-1)^{-2/3}}{(\sqrt{3}|f_{res}^{(1)}|)^4} \\ &\approx \left(\frac{\pi}{2}\frac{(2.7+1.1s)\Sigma a_2^2}{M_* h^2(1+\zeta)}\right)^{3}\left(\frac{1}{0.802\sqrt{3}}\right)^{4} k^{-14/3},\end{aligned} \tag{2.26}$$

$$\begin{aligned}
\tau_a = \tau_{a2} = \frac{M_*^2 h^2}{(2.7+1.1s)\Sigma m_2 a_2^2 n_2} &\gtrsim \frac{P_2}{4}\left(\frac{1}{\epsilon_p}\right)^{4/3} \frac{(k-1)^{-2/9}}{(\sqrt{3}|f_{res}^{(1)}|)^{4/3}} \\
\Rightarrow \quad \frac{M_*^2 h^2}{(2.7+1.1s)\Sigma a_2^2} \frac{2\pi}{P_2} \frac{1+\zeta}{\epsilon_p M_*} &\gtrsim \frac{P_2}{4}\left(\frac{1}{\epsilon_p}\right)^{4/3} \frac{(k-1)^{-2/9}}{(\sqrt{3}|f_{res}^{(1)}|)^{4/3}} \\
\Rightarrow \quad \frac{M_* h^2 (1+\zeta)}{(2.7+1.1s)\Sigma a_2^2} &\gtrsim \frac{\pi}{2}\left(\frac{1}{\epsilon_p}\right)^{1/3} \frac{(k-1)^{-2/9}}{(\sqrt{3}|f_{res}^{(1)}|)^{4/3}} \\
\Sigma \lesssim \frac{2M_*^2 h^2 (1+\zeta)}{(2.7+1.1s)a_2^2 \pi} \epsilon_p^{1/3} \frac{(\sqrt{3}|f_{res}^{(1)}|)^{4/3}}{(k-1)^{-2/9}} &\approx \frac{2M_*^2 h^2 (1+\zeta)}{(2.7+1.1s)a_2^2 \pi} \epsilon_p^{1/3} (0.802\sqrt{3})^{4/3} k^{14/9}.
\end{aligned} \tag{2.27}$$

The equations above show what to expect from the simulations when using Type I migration: $k \propto \epsilon_p^{-3/14} \Sigma^{9/14}$, $\epsilon_p \propto k^{-14/3} \Sigma^3$ and $\Sigma \propto \epsilon_p^{1/3} k^{14/9}$.

Chapter 3 - Method

3.1 N-body simulations

N-body simulations can be used to solve different problems related to planetary dynamics. In order to study orbital evolution as done in this thesis one must integrate the orbits of the planets in the system, including both the Keplerian motion and the perturbations from each other planet in the system. The motion of the planets is then given by its acceleration

$$\dot{\mathbf{r}}_i = \mathbf{v}_i \qquad \dot{\mathbf{v}}_i = \mathbf{a}_i(\mathbf{r}), \tag{3.1}$$

where acceleration depends on the position and the velocity. The equations are solved numerically through the use of an integrator and mapping (Tamayo et al., 2020; Wisdom and Holman, 1991). The most common mapping scheme is the Wisdom-Holman mapping, where the total motion is separated into two terms: The Keplerian motion and the motion due to perturbations from every other planet in the system (Wisdom and Holman, 1991). In the same framework as the previous equation, the equation of motion for multiple planets is

$$\dot{\mathbf{r}}_i^{\text{Keplerian}} = \mathbf{v}_i^{\text{Keplerian}} \qquad \dot{\mathbf{v}}_i^{\text{Keplerian}} = \mathbf{a}_i^{\text{Keplerian}}(\mathbf{r}) \tag{3.2}$$

$$\dot{\mathbf{r}}_i^{\text{Interaction}} = 0 \qquad \dot{\mathbf{v}}_i^{\text{Interaction}} = \mathbf{a}_i^{\text{Interaction}}(\mathbf{r}, \mathbf{v}), \tag{3.3}$$

where the forces felt by the planets is given as contributions to the acceleration of each planet i, separated into the *Keplerian* and *Interaction* part. The integration is then conducted through two main steps; the first calculates the orbit evolution by the Keplerian motion, while in the second the evolution of the orbit due to the perturbations is added (Wisdom and Holman, 1991; Tamayo et al., 2020).

In this project the implementation of the Wisdom-Holman mapping, `WHfast`, from the `Rebound` library has been used. `Rebound` is an N-body integrator library written in C and is open-source licensed. The user can choose their own integration conditions such as integrator, timestep and integration length. Moreover, `WHfast` is a faster and more accurate implementation of the Wisdom-Holman mapping (Rein and Tamayo, 2015).

`WHfast` is a useful and powerful integrator, but does not treat close encounters between planets well. In close encounters the perturbation term is larger, and the motion is not nearly Keplerian. In such cases a Wisdom-Holman integrator gives large errors unless the timestep is very small (Rein and Tamayo, 2015). Another integrator used in `Rebound` which better treats close encounters is `IAS15` with adaptive timestep. It is a powerful 15th order

Gauss-Radau integrator that surpasses the symplectic ones (Rein and Spiegel, 2015). But it is not necessarily better for this project; it is more precise but slower. To further motivate the choice of `WHfast` a test was conducted with Type I migration using `Mercurius`, which is a hybrid integrator based on the `Mercury` algorithm. It saves computational time by using `WHfast` when appropriate and the more accurate integrator `IAS15` for close encounters when necessary (Rein et al., 2019). In this test the inner planet is fixed at the inner disk edge, while the outer migrates from 0.17 AU. The integration time is same as the migration timescale of the migrating planet. Figure 3.1 shows that there are no significant differences that motivate using `Mercurius` instead of the faster `WHfast`.

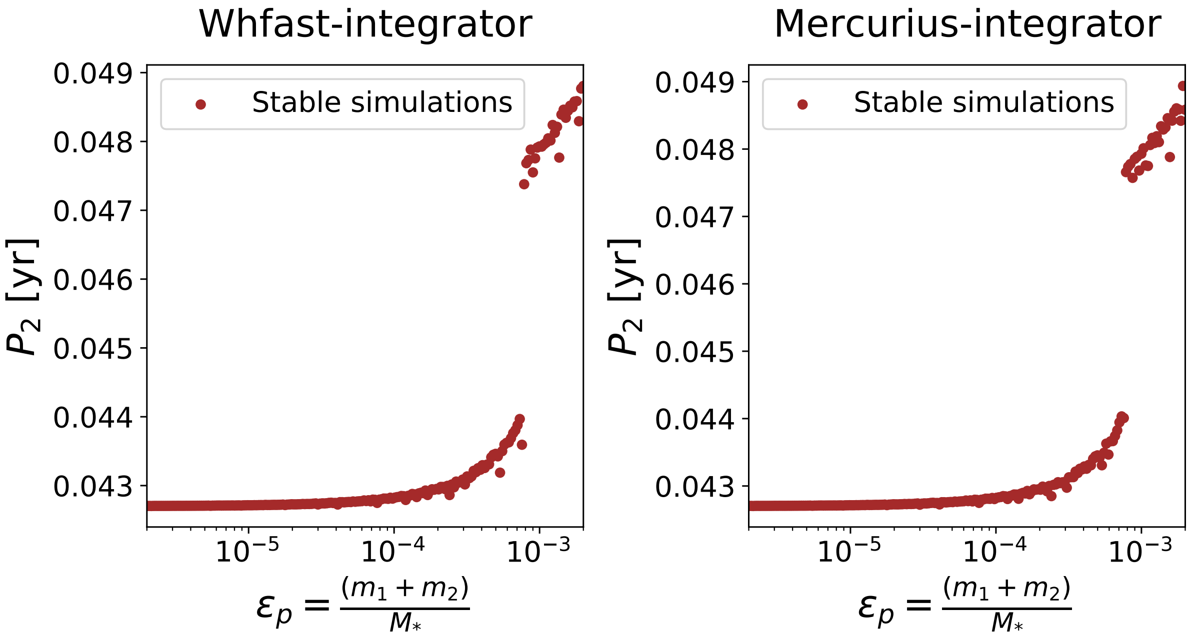

Figure 3.1: Period of the outer planet as function of ϵ_p for a two planet system, the outer migrating via Type I migration while the inner is fixed at the inner disk edge. The integration is done separately with `WHfast`, to the left, and `Mercurius` to the right. Here each point is a system with a different ϵ_p value over a range between $10^{-6} - 10^{-4}\mathrm{M}_{odot}$. There are no significant differences in the shape of the distribution. Thus, `WHfast` is a fine choice for this work.

3.1.1 Type I migration prescription

A complementary library to `Rebound` is `Reboundx`, a library designed to implement non-gravitational forces into the `Rebound` N-body simulations. Thereby, it was possible to code a prescription of both Type I migration and an inner disk edge, as force effects to the main orbital evolution in `Rebound` (Tamayo et al., 2020).

Firstly, the Type I migration prescription is given by the damping timescales of the orbital elements a, e and i given as τ_a, τ_e, and τ_i:

$$\tau_a = \frac{2\tau_{wave}h^{-2}}{2.7+1.1s}\left[P(e)+\frac{P(e)}{|P(e)|}\times\left(0.070\left(\frac{i}{h}\right)+0.085\left(\frac{i}{h}\right)^4-0.080\left(\frac{e}{h}\right)\left(\frac{i}{h}\right)^2\right)\right], \tag{3.4}$$

$$\tau_e = \frac{\tau_{wave}}{0.780}\times\left[1-0.14\left(\frac{e}{h}\right)^2+0.06\left(\frac{e}{h}\right)^3+0.18\left(\frac{e}{h}\right)\left(\frac{i}{h}\right)^2\right], \tag{3.5}$$

$$\tau_i = \frac{\tau_{wave}}{0.544}\times\left[1-0.30\left(\frac{i}{h}\right)^2+0.24\left(\frac{i}{h}\right)^3+0.14\left(\frac{e}{h}\right)^2\left(\frac{i}{h}\right)\right], \tag{3.6}$$

where τ_{wave} is given by equation (2.21) and $P(e)$ is a function of eccentricity given by

$$P(e) = \frac{1+\left(\frac{e}{2.25h}\right)^{1.2}+\left(\frac{e}{2.84h}\right)^6}{1-\left(\frac{e}{2.02h}\right)^4}. \tag{3.7}$$

These equations are based on the formalism of Cresswell and Nelson (2008). The timescales then contribute to the acceleration of the planets

$$\mathbf{a}_a = -\frac{\mathbf{v}}{\tau_a}, \tag{3.8}$$

$$\mathbf{a}_e = -2\frac{(\mathbf{v}\cdot\mathbf{r})\mathbf{r}}{r^2\tau_e}, \tag{3.9}$$

$$\mathbf{a}_i = -\frac{v_z}{\tau_i}\mathbf{k}, \tag{3.10}$$

that give the total motion, again based on Cresswell and Nelson (2008). Here $\mathbf{k}$ is a unit vector in the z-direction in which i is defined.

As one sees in these equations there are a few parameters to be calculated or determined. The disk surface density Σ and aspect ratio h are assumed to follow power laws

$$h = h_0\left(\frac{r}{1\text{ AU}}\right)^{\beta} \tag{3.11}$$

$$\Sigma = \Sigma_0\left(\frac{r}{1\text{ AU}}\right)^{-s}. \tag{3.12}$$

The migration conditions and their equations are based on Pichierri et al. (2018). The free parameters here are: s which gives the disk profile, m the planet mass, M_* the stellar mass, h_0 the scale height at 1AU, Σ_0 the surface density at 1AU and β the flaring index. In the simulations of this project the disk profile used is isothermal, which is given by $s = 1$ with a suitable flaring index of $\beta = 0.25$, based on Pichierri et al. (2018). M_* is always kept at $1\text{M}_\odot$ and the planetary mass is varied. For this type of disk profile and power law equations for the disk properties we will have inward migration (Batygin, 2015; Pichierri et al., 2018). For the determination of the other free parameters refer to Section 5 where a test is presented as motivation for the choice of values for Σ_0 and h_0 respectively [1].

Lastly, even though the inclination was implemented it was not used. No inclination is easier to simulate and enough in this study, and i is quickly dampened to zero by the migration anyway. Nevertheless, implementing it is important in case the code is to be used by other users who want to include inclination.

3.1.2 Inner disc edge implementation

As explained in Chapter 2 an inner disk edge is an important and realistic way to stop planet migration, which has a shorter timescale than disk lifetime. Thus, to ensure that the planets will survive the migration and be possibly captured into a MMR, migration of the inner planet must be stopped at the inner disk edge. Then the outer planet migrates into a MMR with the inner planet (Masset et al., 2006; Pichierri et al., 2018).

In theory as explained in Masset et al. (2006); Ataiee and Kley (2021) migration stops at the inner disk edge thanks to co-rotational torques of roughly equal strength and opposite sign to the migration torques that move the planet inwards. This is called a planet trap, but such torques are difficult to implement numerically. Therefore, a planet trap is implemented as a reversal of the inwards Type I migration torque, which is activated close to the inner disk edge only. The inner disk edge is given at a certain radius, but with a width about that exact radial location, d, given by the aspect ratio at this location, h_{edge}. Following Pichierri et al. (2018) the migration timescale is divided by the factor

$$\tau_{a,red} = \begin{cases} 1 & a \geq d(1 + h_{edge}) \\ 5.5 \times \cos\left(\frac{2\pi(d(1+h_{edge})-a)}{4h_{edge}d}\right) - 4.5 & d(1 - h_{edge}) \leq a \leq d(1 + h_{edge}) \\ -10 & 0 \leq a \leq d(1 - h_{edge}), \end{cases} \tag{3.13}$$

which becomes active and smoothly stops the planet as it reaches within the width of the inner disk edge and rendered non-effective before that, as indicated by a value of one. Here a is the semi-major axis of the planet's orbit (Pichierri et al., 2018).

This implementation also has its free parameters: d the exact inner disk edge location and h_{edge} the aspect ratio at the inner disk edge, both must be given when setting up the simulation [2]. The inner disk edge location is set to a value typical for solar-type stars supported by prior observations, as suggested in Pichierri et al. (2018); Brasser et al. (2018).

---

[1] A link to GitHub to show the implementation code, soon to be part of `Rebounx` for others to use: `https://github.com/Kaltrinak/Type-I-migration-implementation-in-C.git`

[2] The GitHub repository where the code for implementing an inner disk edge, soon to be part of `Reboundx`, can be viewed: `https://github.com/Kaltrinak/Inner_disk_edge_implementation_C.git`

Lastly, Figure 3.2 shows the evolution of the semi-major axis, where numerical results are compared to analytical. This is an integration of one planet undergoing Type I migration with an inner disk edge, as implemented in `Reboundx`. The analytical evolution of a is found by solving for a from

$$\dot{a} = \frac{a}{\tau_a} \propto a^x, \tag{3.14}$$

and with the model of disk used here then $x = 0$, which gives the following solution for a

$$a_{analytical} = \left(1 - \frac{t}{\tilde{\tau_a}}\right), \tag{3.15}$$

where $\tilde{\tau_a}$ are the variables in τ_a independent of a. Figure 3.2 shows that the numerical results agree with the analytical results, further suggesting that the integrator used, the prescription of Type I migration and that of the inner disk edge work well.

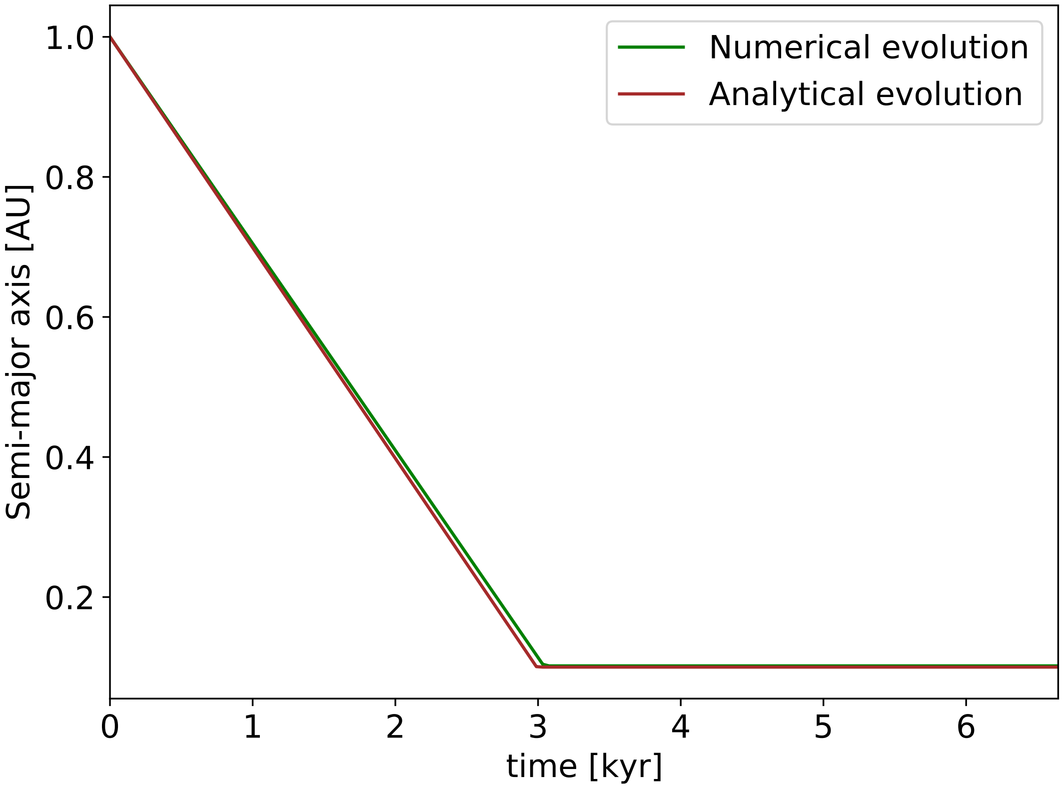

Figure 3.2: Simulated evolution of a compared to the analytical version. The simulation includes both implementation of the inner disk edge and Type I migration. Here one can see that the planet has been stopped at the inner disk edge at $d = 0.1$AU and the two curves agree well.

3.2 Numerical simulation setup

In this subsection the general conditions for the simulations are presented. Firstly, the systems simulated are a three body coplanar problem, with a central star of $1\mathrm{M}_\odot$ and two planets of equal but varying mass. The mass range will be evenly spaced in log-space between $0.33 - 330[\mathrm{M}_\oplus]$ or $10^{-6} - 10^{-3}[\mathrm{M}_\odot]$. According to Armitage (2020) a planet opens a gap in the disk and migrates via Type II migration if its mass relative to the stellar mass is above

$$\left(\frac{m_p}{M_*}\right)_{crit} \simeq \left(\frac{27\pi}{8}\right)^{1/2}\left(\frac{h}{r}\right)^{5/2}\alpha^{1/2}. \tag{3.16}$$

For typical disk models as used here, the viscosity parameter α is between 10^{-2} and 10^{-3}. Using $h/r = 0.05$, which is typical for protoplanetary disks, and for example $\alpha = 10^{-2}$, the critical mass for Type II migration is $m_p/M_* = 1.8 \cdot 10^{-4}$. In this project the mass range investigated goes to larger masses than this, to consolidate the observed trend in our simulations despite these values not being physical for Type I migration.

The general initial conditions for the orbital parameters are; $a_{init} = [0.1, 0.17]$ when inner planet is fixed at the inner disk edge, and $a_{init} = [1, 1.8]$ or $[0.5, 0.85]$ when both planets are set to migrate. In all simulations the outer planet is always located just outside the outermost first order MMR, 2:1, determined using $a_2 = ((k+1)/k)^{(2/3)}a_1$ for any given a_1 (solved from Equation 2.6). The initial eccentricity is always kept at zero (circular orbits). This is reasonable because planetary migration quickly dampens the eccentricity to zero anyway. Moreover, using initially circular orbits saves computational time at the start of the simulation. Furthermore, other works such as Ogihara and Kobayashi (2013) have shown that the critical value of τ_a for capture into MMR does not depend on initial eccentricities when the planets have comparable mass. The integration time is set at one τ_{a2} in units of years, which is enough to get the outer planet in a MMR no matter the mass. Moreover, the timestep of an integration is a percentage of the inner disk edge orbit, if any is used, otherwise the orbit of the inner planet when in MMR is appropriate. In this project the timestep is kept the same for all simulations at $P_d/20$, roughly 5% of the period at the inner disk edge. The inner disk edge is set at 0.1AU as suggested by Izidoro et al. (2017); Brasser et al. (2018) to be suitable for a solar type star and Type I migration. Table 3.1 summarizes all the initial conditions for easier access.

All investigations will be done separately for two cases. One is a controlled setting with constant damping timescales, where τ_a will be varied in log-space in the range $100 - 20000$yr, in order to see how capture for different ϵ_p is changed with damping timescale. The lower bound is low, but still gives a longer evolution time of a than the orbital period of either planet. The upper bound is large enough to show all the interesting science without a large computational cost or rendering the inner disk edge ineffective. The damping timescale of eccentricity is given as $\tau_e = \tau_a/100$ and kept the same for both planets. In Batygin and Morbidelli (2012); Deck and Batygin (2015) they showed that if τ_e and τ_a are comparable then no capture can occur, since e would not be dampened to zero before MMR encounter and τ_a is no longer independent of e and τ_e. As already explained the damping timescale of

i will not be included here. A coplanar setup is a reasonable approximation since migration quickly dampens inclination to zero and unlike eccentricity it does not in general increase when in a MMR. The other setting includes investigations with Type I migration, for which damping timescales are determined by the parameters of the equations in Subsection 3.1.1.

Lastly, for both settings the study will be separated into two cases: 1) The inner planet is fixed at the inner disk edge, thus the relative damping timescale is $\tau_a = \tau_{a2}$. 2) The inner planet migrates too. In this case $\tau_a = 1/(1/\tau_{a2} - 1/\tau_{a1})$ as presented in Deck and Batygin (2015).

Table 3.1: This table holds the main initial conditions, which were explained thoroughly in the text above.

Parameter		Parameter	
d [AU]	0.1	e_{init}	zero
a_{init} [AU]	Fixed inner planet [0.1, 0.17] Moving inner planet [1, 1.8] or [0.5, 0.85]	i_{init}	zero
t_{integ} [yr]	$2\tau_{a_2}$	τ_e	$\tau_a/100$
timestep [yr]	$P_d/20 = 1.6 \cdot 10^{-3}$	τ_i	zero
ϵ_p	0.33 to 330 $M_\oplus$ or 10^{-6} to 10^{-3} $M_\odot$		

Chapter 4 - Constant timescales

Firstly, according to for example Mustill and Wyatt (2011); Batygin (2015) MMR outcomes depend on planetary mass, migration rate and pre-encounter eccentricity. However, as mentioned in Section 3.2, some parameters that can seem important have been excluded from the investigations. These are i, e and their damping timescales. The first was directly excluded due to the coplanar approximation, which was chosen in order to make the investigations simpler. As for the latter, papers such as Ogihara and Kobayashi (2013); Pichierri et al. (2018), investigating the impact of τ_e and e on capture into specific MMRs, showed that both these parameters have negligble to no impact for planets with comparable mass and eccentricites below 0.01. The latter was also confirmed by Mustill and Wyatt (2011). This is not unexpected since e is quickly dampened to zero before encountering a MMR, with a timescale much shorter than the migration timescale, and e is not expected to be initially large for planets with no prior chaotic behaviour. Moreover, these parameters do not directly change the convergent migration so capture into MMR will happen and be more dependent on the planetary masses and the damping timescale of the semi-major axis. Thus, the initial eccentricity is kept at zero and τ_e is not investigated but kept at $\tau_{e1} = \tau_{e2} = \tau_{a2}/100$. Only ϵ_p, the planetary mass relative to the star, and τ_a, the relative migration timescale, are investigated in this setting.

Before moving on to the main results of this project, Figure 4.1 and 4.2 illustrate how the orbital elements and the resonance angles evolve over time and how convergent migration leads to MMR. For this simulation I choose $m_1 = m_2 = 5 \cdot 10^{-6}$, and migration timescales $\tau_{a1} = 20$kyr and $\tau_{a2} = 10$kyr. The other initial conditions are the same as given in Section 3.2 for the case of migrating planets. In Figure 4.1 it is clearly visible when the system enters a MMR, indicated by the increase in eccentricity and a commensurate period ratio. The orbital elements a and P decrease for both planets while in migration, but when stable capture into MMR occurs both a and P decrease at the same rate, meaning the planets migrate together towards the inner disk edge. Other studies such as Ogihara and Kobayashi (2013); Deck and Batygin (2015); Ataiee and Kley (2021) show similar orbital evolution. This system has passed through two MMRs, indicated by the small peaks in the e-plot, before being captured into the third encountered MMR, 4:3. The oscillations in the stable MMR are small at first and almost zero as the system stabilizes towards the equilibrium eccentricity of that MMR. This equilibrium value corresponds to the fixed point around which the resonant system librates Pichierri et al. (2018). Furthermore, we see here, and in general, that MMR encounter and eventually capture occurs early on, within the integration time of 20 kyr for all masses investigated, as also seen in for example Izidoro et al. (2017).

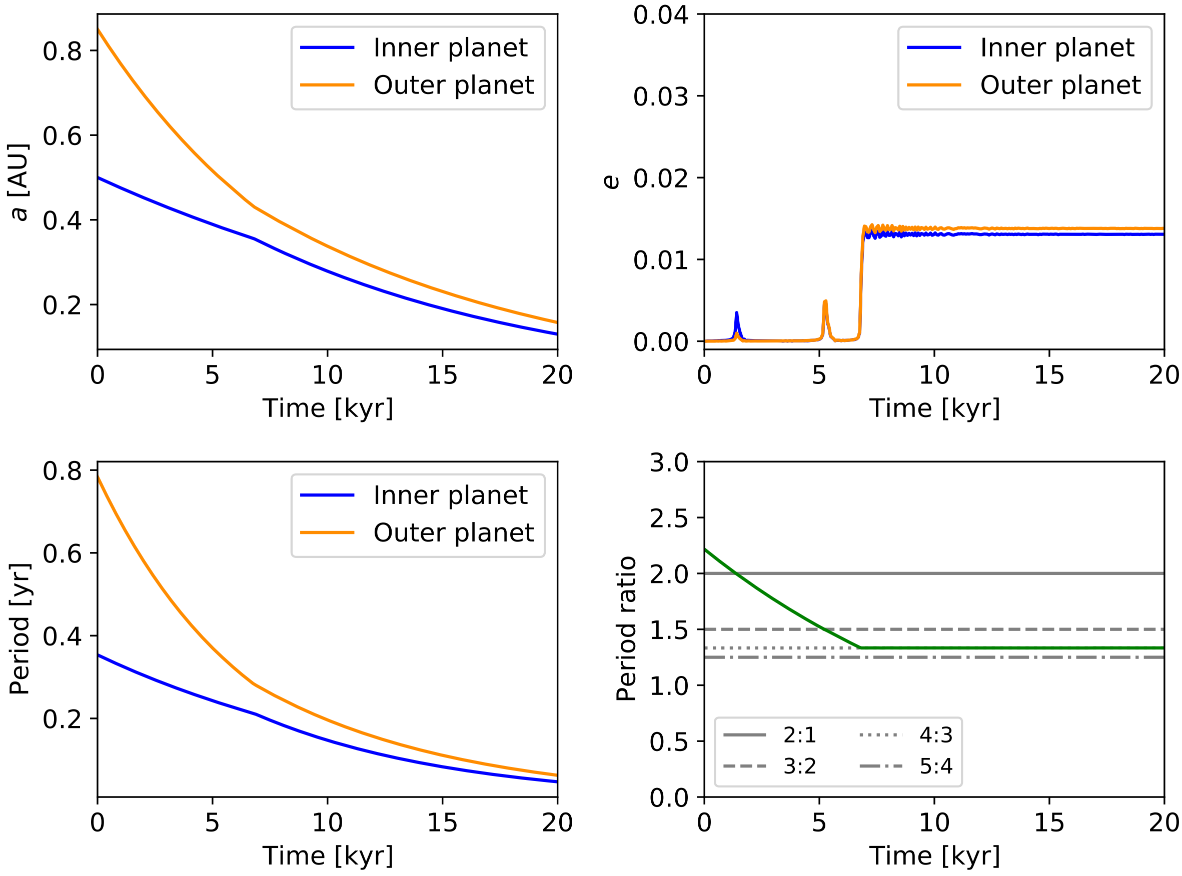

Figure 4.1: Evolution of a, e, orbital period and orbital period ratio over integration time, of a system with equal mass planets at a mass of $5 \cdot 10^{-6} \mathrm{M}_{\odot}$.

The plots in Figure 4.2 show the evolution of the resonance angles at the four outermost MMRs. Here we demonstrate the capture of the system in the 4:3 MMR and the stability in it. We see how the resonance angles for the 4:3 MMR evolve towards a fixed value when the system is captured into the MMR. In the other plots the resonance angles occupy the full range they are plotted over $(0 - 2\pi)$. There are attempts to centralize around a constant value at early integration time in both the 2:1 and 3:2 MMR, indicating that the system did pass these very quickly. In Mustill and Wyatt (2011) it was shown that for low e before MMR encounter librations are small in amplitude, supporting the findings here. Stability of the resonance is indicated by the amplitude of the oscillations around the fixed point. If unstable the amplitude is large and the MMR soon breaks (Deck and Batygin, 2015; Batygin and Adams, 2017). The passage through the first encountered MMRs illustrate that for these two MMRs, the time to cross the resonance width was much shorter than the libration timescale, due to the small mass and fast migration. Thus, the adiabatic condition was not fulfilled and capture did not occur until the condition was satisfied at the 4:3 MMR with larger width. Furthermore, once a system exits a MMR the orbital elements are again dampened due to migration until the next MMR is encountered. The process repeats until the encountered MMR is stable.

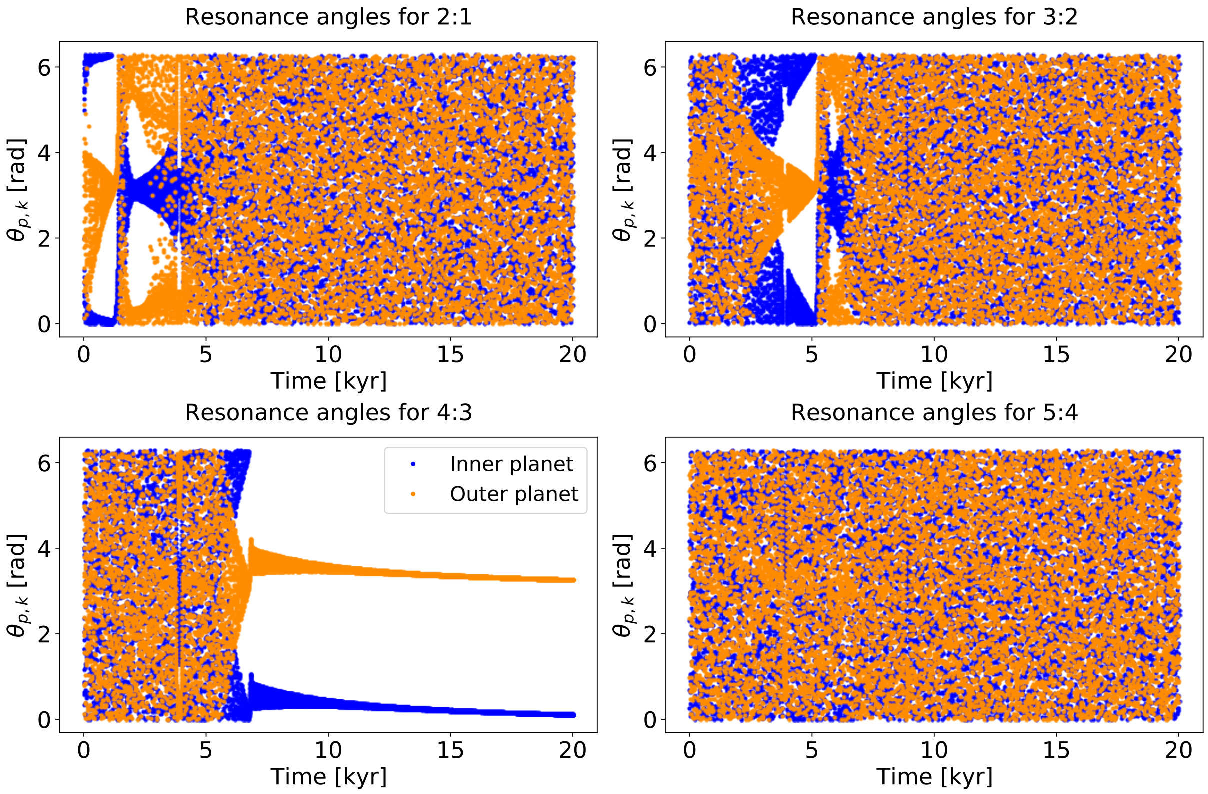

Figure 4.2: Evolution of the resonance angles θ, where index one always denotes the inner planet and index two the outer. This is the same system as above, captured in a 4:3 MMR.

The figures above are good for context and to understand how the model of MMR capture via migration works. However, they do not show how a parameter affects capture into MMR. Instead, we use the resonance index

$$k = \frac{1}{\frac{P_2}{P_1} - 1}, \tag{4.1}$$

a function of the period ratio, to identify if a system is trapped into a MMR and which. Then for any parameter one can find out at which MMR the system is captured. Plotting all the resonance indices this way enables us to explore a large range of values for the parameter and deduce overall trends, as opposed to only looking at specific MMRs and critical values for capture into that MMR (Ogihara and Kobayashi, 2013).

The first parameter to be tested was planetary mass to stellar mass ratio, ϵ_p. Varying the planetary masses, with a ratio of one and constant damping timescale lets us focus on the importance of ϵ_p alone first. Figure 4.3 shows how planetary mass impacts capture into MMR for the case of fixed inner planet with relative damping timescale $\tau_a = \tau_{a2} = 10$ kyr. In both Figures, 4.3 and 4.4 each red dot represents a system integrated with a different initial ϵ_p value from the full range investigated. The other initial conditions are given in Section 3.2. The analytical formulas for overlap of resonances and the adiabatic criterion are also included. Moreover, most of the systems in the region of $10^{-8} \geq \epsilon_p \lesssim 2 \cdot 10^{-7}$ are unstable and removed. We arbitrarily identify these as having a period ratio $1 < P_1/P_2$ or $P_1/P_2 < 0.3$, and/or orbital period $P_1 > 1.05$ yr. A period ratio of ≤ 0.3 means the planets were scattered to periods further away than their initial position, and a ratio above one means the planets have swapped place, since normally $P_2 > P_1$. $P_1 > 1.05$yr simply puts a higher limit on the orbital period of the inner planet, which should stay close to the inner disk edge and not be ejected above a period of ~ 1. Moreover, because I am plotting the resonance index, a continuous variable of the period ratio, the systems with commensurate period ratio will by definition stack at integer values. That is, all stable systems translate to capture into a MMR with index k. The transition between indices is clean and immediate for larger ϵ_p, until capture becomes probabilistic; for the same ϵ_p value there are two occupied resonance indices, and two resonances exist at the same time.

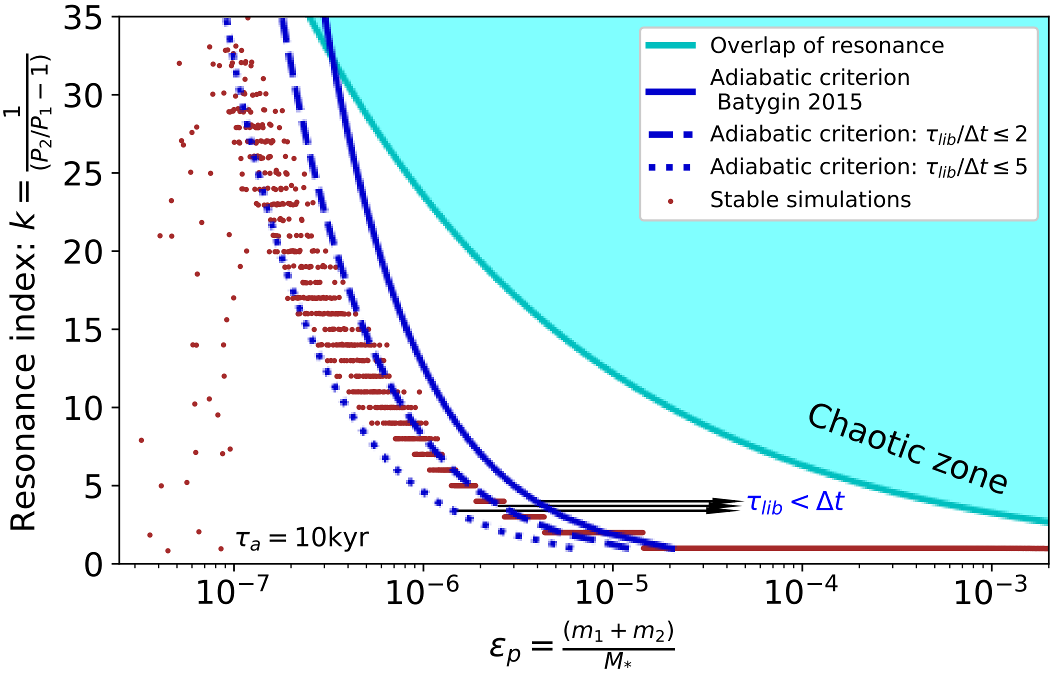

Figure 4.3: Resonance index as function of ϵ_p with $\tau_a = 10$kyr. Here the ϵ_p range is wider, $10^{-8} - 10^{-3}\mathrm{M}_\odot$, to illustrate the chaotic behaviour of smaller masses better. Although it is unrealistic that such small masses migrate at all.

From Figure 4.3 we see that in general smaller ϵ_p means capture into higher resonance index. Moreover, the transition to probabilistic capture occurs at $m \approx 2 \cdot 10^{-6}\mathrm{M}_\odot$, and the masses larger than roughly $10^{-6}\mathrm{M}_\odot$ are all captured at $k \leq 6$, with clear transitions between indices indicating certain capture. This can be attributed to the fact that the libration timescale decreases with decreasing period. In this case the system is as close as it can be to the star since the inner planet is fixed at the inner disk edge. Therefore, it is easier to capture the outer planet into lower resonance indices that do not overlap, for a wide range of masses. As explained in Subsection 2.2.1 and shown in Figure 2.4, smaller ϵ_p means overlap of resonances appears first at a higher resonance index. Whereas, the opposite is true for large ϵ_p, but still not until a period ratio of $\lesssim 1.5$ for the largest mass of 10^{-3}, which corresponds to the 3:2 MMR. The large masses in Figure 4.3 are captured into 2:1 which does not overlap for such masses. While the small masses, beyond $\approx 2 \cdot 10^{-6}\mathrm{M}_\odot$, are all captured at high k where the resonance widths overlap and motion is no longer deterministic (Mustill and Wyatt, 2012; Ogihara and Kobayashi, 2013).

The outliers with small ϵ_p values are systems that at the end of integration are captured into a MMR of lower k, even though the mass is small and would, when impacted by only migration, not be stable or captured at such large period ratios. Looking at the output of a few individual simulations in this region, the evolution of the period ratio over integration time, we saw two explanations for these systems (see Figure A.3 in Appendix A.1 for examples). Firstly, some of these systems are simply very chaotic. The planets jump from capture into one MMR to another, then the end of integration time they happened to be captured into a MMR with lower k value than suggested by the general trend. However, due to their chaotic behaviour these systems would continue to escape MMRs in the same manner if integrated longer. Thus, they are unstable systems that seem to be stable in a MMR by our definitions of k at the end of integration time. Secondly, some of these systems migrated directly to high a k MMR, as expected for low mass values, where overlap is completely dominant and stable motion cannot be maintained. With such small separations the orbits will cross, leading to instability and scattering towards larger periods, either at once or after a few orbits (Ogihara and Kobayashi, 2013; Pichierri et al., 2018). These systems thus end up restarting their journey from larger periods towards higher k MMR, but do not reach as high k agian before the end of integration. Instead, they are captured into a lower k MMR for the time being and are for this reason not filtered out by the criterion for stable systems. These behaviours were also seen in Batygin and Morbidelli (2013); Deck and Batygin (2015); Izidoro et al. (2017), and these systems cannot be taken as long term stable even if they seem stable now.

Furthermore, the stable systems on the "staircase" follow the trend suggested by the adiabatic model. However, the analytical criterion fails to follow the transitions. Systems stable in a MMR should be located to the right of the adiabatic curve and below the overlap curve. However, changing the equation for the adiabatic condition slightly to

$$\epsilon_p = \left(\frac{P_2}{8}\frac{1}{\tau_a}\right)^{3/4} \frac{(k-1)^{-1/6}}{\sqrt{3} f_{res}^{(1)}}, \tag{4.2}$$

where $\tau_{lib}/\Delta t \lesssim 2$ instead of one as in Equation (2.13), we get better agreement, and best for $\tau_{lib}/\Delta t \lesssim 5$. It is arbitrary to choose how much shorter the libration timescale is than the time it takes to cross the resonance width. The disagreement could also be attributed to the slope being too steep, due to unaccounted effects in the analytical model used to derive the adiabatic condition. Moreover, the f_{res} component was approximated as shown in Equation (2.15). However, this cannot be behind the difference. All we can say at the moment, without the time to go through the full theory of adiabatic migration, is that all the simulations on the steps of integer k fulfill the condition. However, the adiabatic condition curve needs to be tweaked a bit to match the transitions.

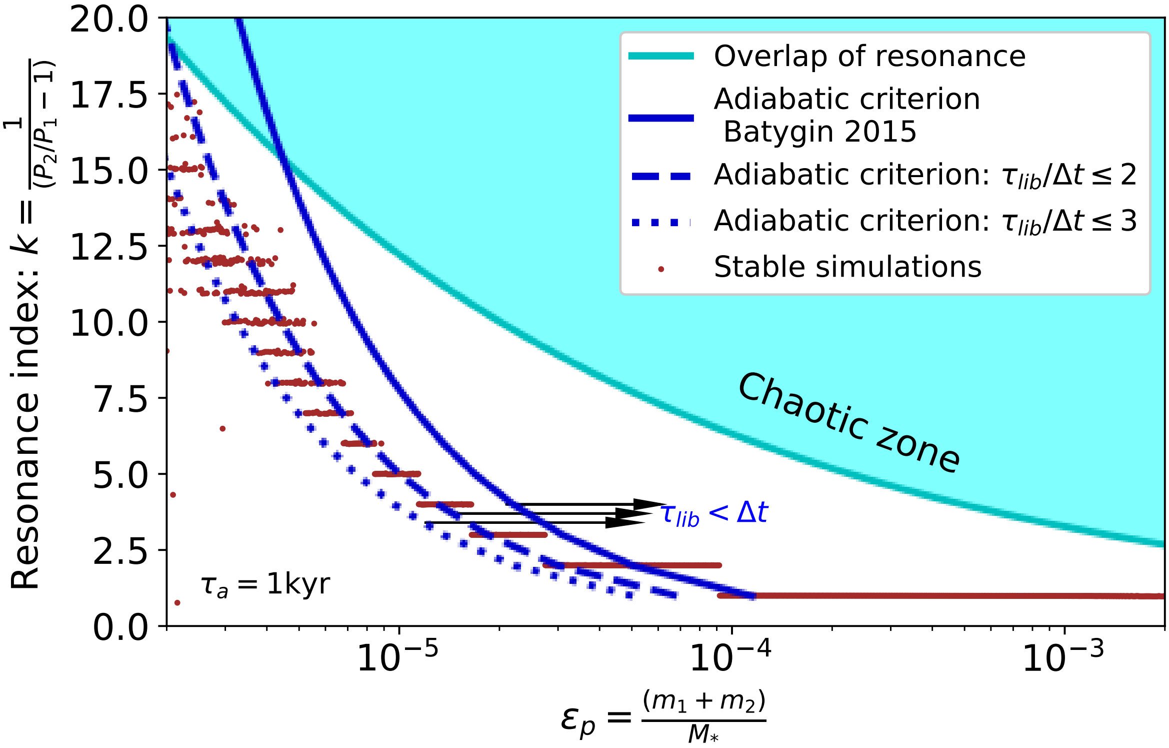

Figure 4.4: Resonance index as function of ϵ_p for a case of shorter damping timescale, $\tau_a = 1$kyr. The rest of the initial conditions are identical to the above figure.

Figure 4.4 shows how decreasing the migration timescale impacts capture into MMR for the usual set of masses $10^{-6} - 10^{-3}\mathrm{M}_{\odot}$. The capture behaviour is less clean, and the probabilistic capture starts for larger masses than in Figure 4.3, which is expected. Faster migration has larger libration amplitude that further complicates capture into MMR (Mustill and Wyatt, 2011). Shorter τ_a forces stable capture to occur at higher k, smaller periods, where $\tau_{lib} < \Delta t$ can be satisfied. Thus, only the larger planets can be stable in lower indices even though they too migrate faster in this case. If τ_a is short enough, capture becomes impossible, because the adiabatic condition cannot be satisfied even for large ϵ_p or low k. Of course, the opposite should then be true when τ_a is instead longer. In the latter case the libration timescale is shorter than Δt satisfying the adiabatic condition for all indices. Thus, all masses can be captured into lower indices, which is the opposite to what we see in Figure 4.4. If τ_a is long enough all masses should then be captured into the 2:1 MMR. Note that all this holds for any initial position, starting outside the 2:1 MMR as set up here, only the value for τ_a to produce such extreme scenarios is not the same. That is, attributed to the dependency on the orbital period of the outer planet of the libration timescale. Moreover, in both scenarios the values required are unrealistic: such short τ_a cannot be provided by any disk and the typical timescale of the Type I migration prescription, valid in this mass regime, is not longer than roughly 2Myr.

Furthermore, we again see cases of smaller masses that do not follow the trend and are not in a MMR, same as the outliers in Figure 4.3. Following the same reasoning these systems are chaotic and a consequence of scattering due to crossing orbits caused by overlapping MMRs. One more thing to note here is that the adiabatic condition again does not fit the simulations unless $\tau_{lib}/\Delta t \lesssim 3$. Note that the same investigation was done with the case where both planets migrate from a position $a_{init} = [0.5, 0.85]$ AU, which show the same qualitative behaviour. These plots can be found in Appendix A.

Lastly, inspired by what we have seen so far, a system can seem stable in a MMR with quite large oscillations. There are two fates for such a system. The first is the integration time was too short. Thus, when increased the MMR will visibly break and the planets continue to migrate into another MMR. As proven in Deck and Batygin (2015) systems spend more time in a MMR than in between, even with large oscillations. The escape time is comparable to τ_a rather than τ_e as first believed in order to explain the pileup of systems just wide of a MMR in observations. The second is the MMR does not break during the lifetime of the disk, but does so most likely as soon as the disk dissipates and the instability phase starts (Pichierri et al., 2018).

4.1 2D grids

Now that we have seen how orbital elements evolve with migration, that both ϵ_p and τ_a have important roles in the capture of a planetary system into MMR. The next step is to generalize the investigation of both parameters by integrating the systems with all combinations of τ_a and ϵ_p within a wide range of values. Doing so we can see general trends of how capture depends on both these parameters.

4.1.1 Capture at the inner disk edge

The first 2D grid, Figure 4.5, has dimensions 300x300 with ϵ_p between $10^{-6} - 10^{-3}\mathrm{M}_\odot$ and $\tau_{a2} = \tau_a$ varied between 100-20000yr. The lower limit of the τ_a range can seem low but is still roughly 3000 orbits for orbits at the inner disk edge. The upper limit does not need to be larger, because we expect the trend to continue unless something else is at play, and this way we save computational time. Moreover, capture into 2:1 would be guaranteed for longer τ_a as already discussed and shown by the trend in the grid. The colourmap is discrete because we know by the definition of k, that systems in MMR have integer values. Plotting in this manner makes it easier to see the trends. Worth noting is that systems close to a commensurate period ratio are also averaged to the closest integer k. To distinguish these, one can look at where they are in the grid and the individual simulation outputs. The 1D plots showed that such cases are usually found in the chaotic region.

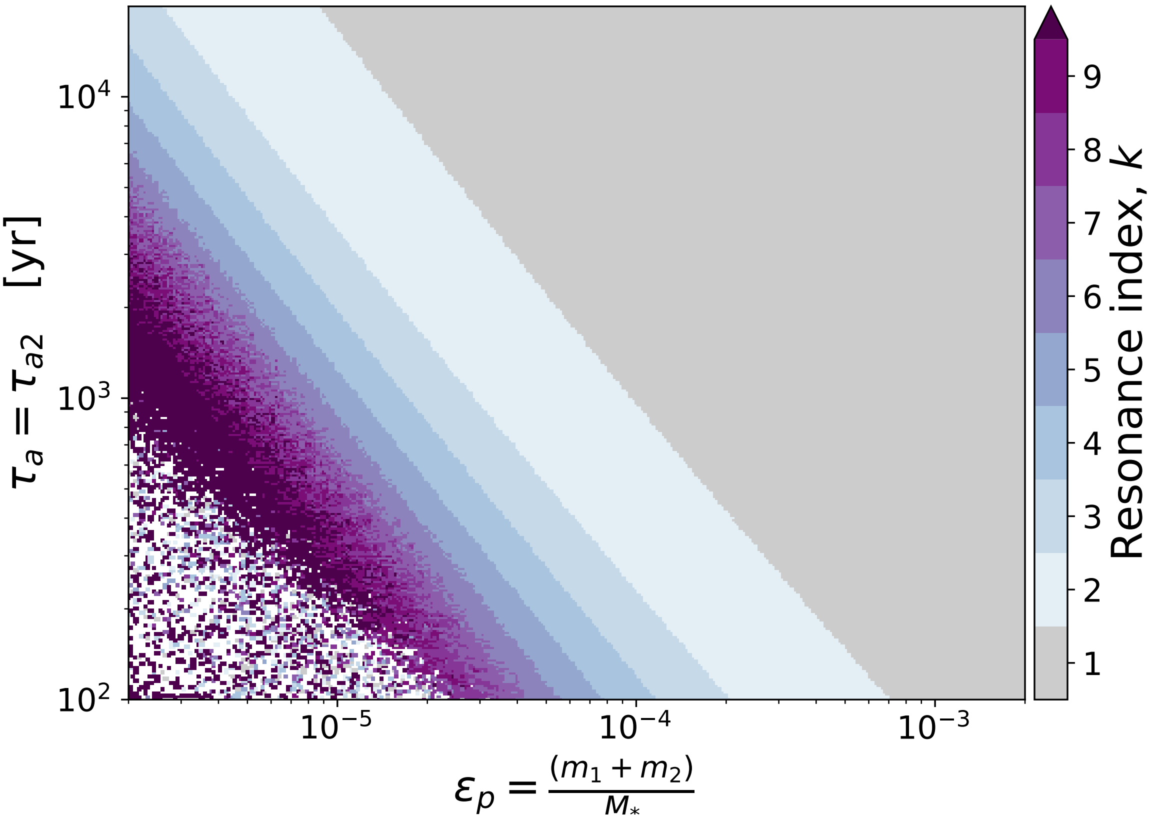

Figure 4.5: Resonance index of the MMR as a function of ϵ_p and τ_a. The white colour indicates that the system is not in a MMR and is unstable.

The first thing to notice is the confirmation of what has already been mentioned previously. That is, smaller planetary mass means capture into higher resonance index and that longer τ_a makes it possible for smaller masses to naturally be captured into lower k than otherwise possible. Most significantly, there is a linear trend which suggests a power law relationship between the two parameters in agreement with the adiabatic model from Batygin (2015). The slope of this trend is discussed in Section 4.3.

Moreover, we see how for the longer τ_a-values, k reaches only up to three, while shorter τ_a in comparison leads to stable capture at higher k even for larger ϵ_p. Increasing τ_a while keeping everything else the same, should at some value lead to capture at $k = 1$ for all masses. In the same principle we see how the opposite can be said for when damping timescale is short. For larger masses τ_a can be shortened further than for smaller masses, without becoming chaotic. However, the trend suggests that at some point of much shorter τ_a all masses will display chaotic motion and instability. The chaotic motion appears at $\tau_a \lesssim 3000$ years, the white portion, and increases in size when τ_a is further decreased.

4.1.2 Capture while migrating

Here we go from a controlled setup, as in the previous grid where we know most planets will be captured into a MMR, to a case of both planets migrating, presented in Figure 4.6. We investigate the problem with the same ϵ_p range but τ_a, is now varied over a wider range between 20-40000yr. The damping timescales are set as $\tau_{a1} = \tau_a, \tau_{a2} = \tau_a/2$ and the planets migrate from [1, 1.8] AU. Here the planets are captured while the inner planet is at slightly different positions for each combination of ϵ_p and τ_a.

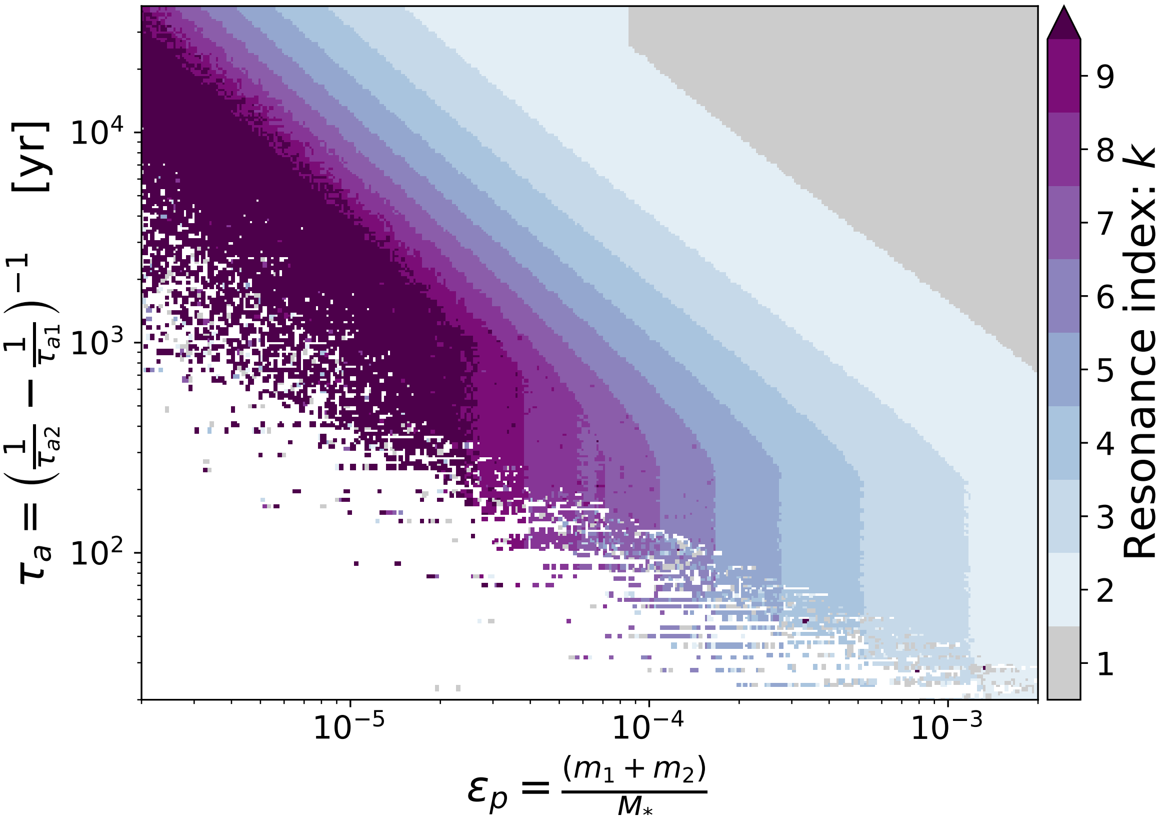

Figure 4.6: A similar 2D grid to the one in previous section, showing how τ_a and ϵ_p affect MMR capture. Here both planets are migrating from an initial position of [1, 1.8] AU.

Firstly, we again see a linear trend as in Figure 4.5. That is, the same qualitative behaviour is present in a case of both planets migrating towards the inner disk edge, which is the power law relationship between ϵ_p and τ_a. Again, we see that longer τ_a leads to stable capture in lower k MMRs that do not overlap. As τ_a is decreased more of the larger masses end up in higher k while the smaller masses enter the chaotic zone. The chaotic zone appears earlier, at longer τ_a, than in the case of capture at inner disk edge. Almost all systems are unstable when both τ_a and ϵ_p have small values (the white portion of the grid). Overall, k reaches higher values than for the same τ_a and ϵ_p-values in the controlled case. The main reason is that here the planets are trapped in a MMR while both migrating, meaning capture occurs at larger periods and not always at the inner disk edge, as in Figure 4.5. As shown in Equation (2.13) libration timescale depends on the period at capture. Thus, the libration timescale in general is longer at larger periods, and so the adiabatic condition is satisfied at a higher k MMR than for planets captured in a MMR at smaller periods.

Additionally, this setup effectively shows a “fixed” inner planet case at 1AU for long τ_a because it means little migration, especially for the inner planet, which here migrates at half the speed of the outer planet. Although this is not as effective as a proper planet trap, it still shows that a fixed inner planet at larger distance from the star means fewer systems at lower k. This confirms that closer to the star it is easier to capture into MMR and the motion is less chaotic, because smaller period corresponds to shorter libration timescale. This also helps explain why the chaotic motion starts at larger ϵ_p and longer τ_a than for the case of inner planet fixed at inner disk edge.

Moreover, we have quite a few outliers that seem to be in MMR but seemingly in the chaotic region. Looking at individual systems in a small portion of this region, we see that indeed these systems are chaotic. They reach high k (or small period ratio) from which the planets are scattered to larger periods where they again migrate towards high k. In many cases this happens a few times before the planets at the end of the integration time are captured in a lower k value. However, given their chaotic behvaiour over time, they are likely not stable in this MMR after disk removal. Moreover, some of these systems just seem to have been averaged to the closest integer k, since they had large enough period ratio and small P_1 to not be classified as unstable at the end of integration. These chaotic systems are found at larger ϵ_p and shorter τ_a or smaller ϵ_p and longer τ_a, which naturally are captured at higher k MMRs where overlap of resonances plays an important role. Another thing to explicitly mention is that most of the systems in the chaotic region are unstable and removed by our general criteria for instability (assigned a white colour). These systems are actually similar cases as the outliers in the 1D plots already discussed in detail at the beginning of this chapter, and the same type of outliers were also seen in the chaotic region of the above grid (see Figures A.4 and A.5 in Appendix A.1 for examples). Also, we see the same trend even among these systems; smaller masses are captured into higher k MMR than larger masses.

Furthermore, by inspecting the simulation output we have seen that when τ_a is short and ϵ_p is small, the planets are tightly packed at the inner disk edge. This is expected for shorter damping timescale, as the planets migrate further before capture (if any) can occur, especially for smaller mass. This was also seen for the Super-Earths in Izidoro et al. (2017, 2019) and in other studies e.g. Ogihara and Kobayashi (2013); Deck and Batygin (2015); Pichierri et al. (2018). These systems are also very likely to break their MMR after disk removal, especially if the number of planets is larger and the masses are small. One last thing to comment on this grid is the vertical transition from 2:1 to 3:2 at the longest τ_a values and $\epsilon_p \approx 2 \cdot 10^{-4}$, which could be overstable systems. That is, the planets escaped 2:1 for higher k after spending a long time captured in 2:1 (Deck and Batygin, 2015). Looking closer at a few examples of systems from this region of the grid, we can confirm that so seems to be the case (see Figure A.8 in Appendix A.2). Such behaviour does not follow the power law trend. The vertical transitions for all k at shorter τ_a are discussed in the following section. In Appendix A.4 I have also presented an example of a case with nonequal mass planets, where overstability is clearly present for most MMRs, to illustrate the behaviour even if not discussed or investigated in detail.

4.2 Hill stability and overlap

In Figure 4.6 there are systems governed by chaotic motion and perhaps instability, that still do not make the cut of unstable systems. These are the outliers that do not follow the power law trend but are captured into a MMR. These seem stable in a lower k MMRs, than their counterpart at the same ϵ_p but slightly longer τ_a, for example the 2:1 outliers for large ϵ_p. Larger masses being in 2:1 MMR is not strange. As seen in Ogihara and Kobayashi (2013) capture into 2:1 MMR can happen at shorter τ_a if the planetary masses are large. However, when τ_a is so short it is less likely that even larger masses are stable in 2:1 MMR naturally. I believe these are instead chaotic systems that scattered to lower k. This was confirmed by looking at individual simulations from a small part of this region, as explained in Subsection 4.1.2. To further show this is the case I have plotted the level curve of the overlap condition from Deck et al. (2013), on Figure 4.6. A system is chaotic if

$$\frac{a_2 - a_1}{a_1}\epsilon_p^{-2/7} \leq 1.46, \tag{4.3}$$

where the semi-major axes values are the final positions of the planets at the end of integration. In Figure 4.7 we attempt to visualize the overlap limit on our simulations. We thus overplot the level curve given by Equation 4.3, at the end of integration after smoothing over nearby simulations. We can then identify the main delimitation despite the scattering in the region and confirm that the outliers in MMR, below the overlap curve, are indeed a result of overlap of resonances. Note that eccentricity is very low and so it is not of concern that the overlap condition does not take eccentricity into account. Being in the chaotic zone means that these outliers will most likely not stay stable over time or after disk removal. Further, showing that the impact from planetary mass is weakened while at the mercy of chaotic motion due to overlap of resonances. Overlap of resonances can thus change the outcome to a final architecture that would otherwise not be natural for such ϵ_p and τ_a, as also supported by Wisdom (1986); Mustill and Wyatt (2011); Batygin and Morbidelli (2013); Deck and Batygin (2015)

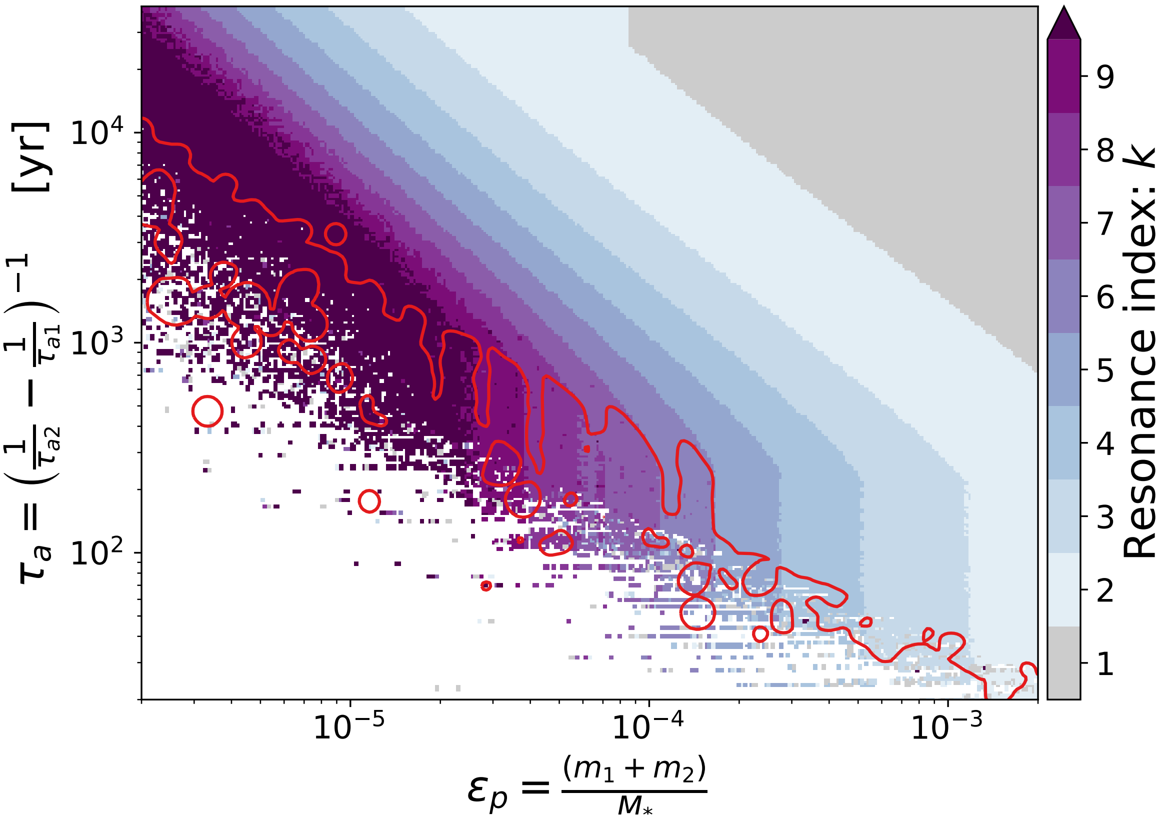

Figure 4.7: The dark red level curve marks out the chaotic zone of the 2D grid of migrating planets presented above.

Additionally, already here we see that some systems at the vertical transitions are chaotic, and therefore not expected to maintain the power law trend. That is, beyond the last stable MMR, the trend cannot be followed as those systems are in the chaotic zone.

The vertical transitions for larger masses are puzzling, as they are not chaotic and suggest that at some point the regime investigated no longer works in the expected way. Beyond this point again the power law trend is not followed. Instead, the power law trend abruptly stops in the form of a vertical transition independent of τ_a. This transition occurs at smaller ϵ_p for increasing k. The next idea to investigate is if these systems are unstable for any other reason, and that is Hill instability (Gladman, 1993), which occurs when

$$\frac{2(a_1 - a_2)}{a_1 + a_2} \left(\frac{\epsilon_p}{3}\right)^{-1/3} \leq 3.46. \tag{4.4}$$

This level curve is plotted in the same manner as that of the overlap criterion, where the semi-major axes are values at the end of integration (the final position of respective planet). Applying the criterion to the full sample in the same way as for the overlap condition, see

Figure 4.8, we see that most of the systems at the vertical transitions are Hill unstable. The power law trend is followed until a combination of τ_a and ϵ_p that is Hill unstable, at which point and beyond the evolution of the planets only depends on ϵ_p and the spacing between the planets. That is, as τ_a is so short that the planets migrate close before capture, there will be a point in terms of ϵ_p where the planets are too close given their large mass to be Hill stable. This point is reached at smaller ϵ_p for higher k, as the spacing further decreases with increasing k. Note also that some outliers are actually Hill stable at the end of integration. As shown in Pichierri et al. (2018), systems in MMR as opposed to non-resonant systems, can be stable beyond the traditional Hill stability limit used here. However, this holds only for smaller ϵ_p values or higher k.

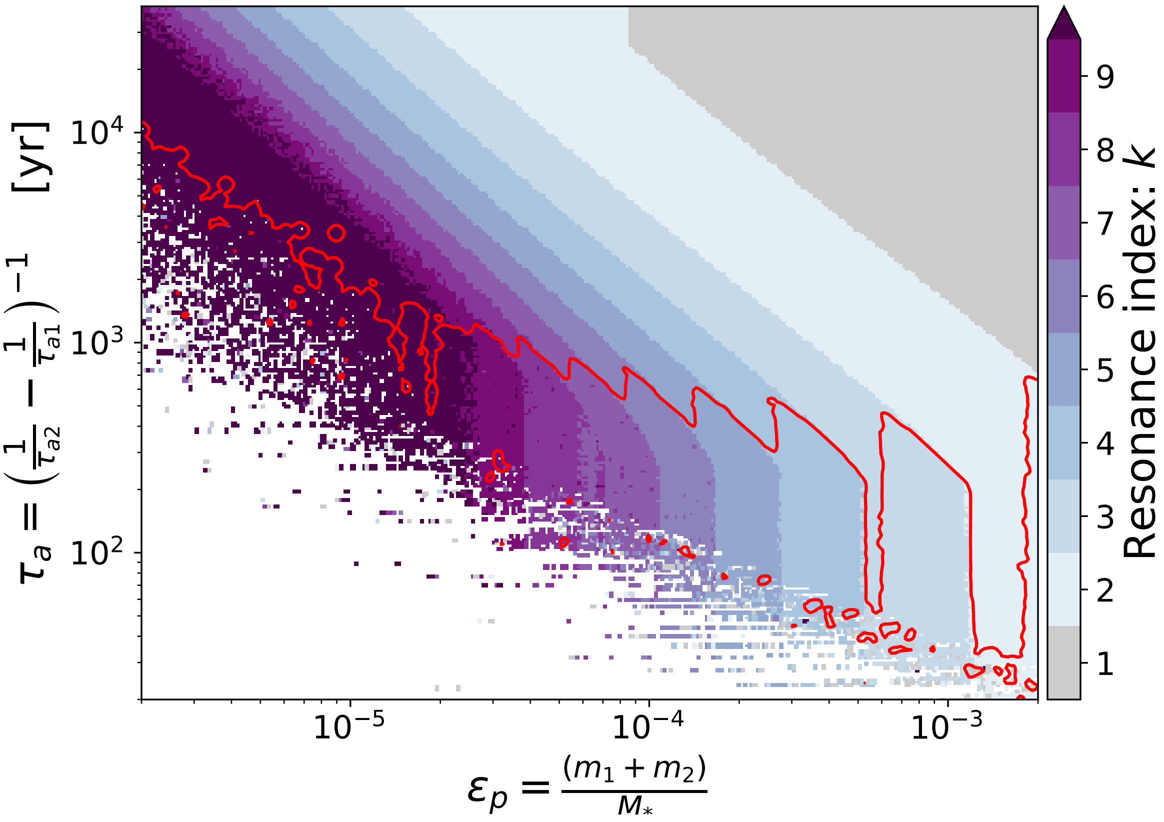

Figure 4.8: The bright red level curve marks out the Hill instability limit of the 2D grid in Figure 4.6, below which the systems are not Hill stable.

4.3 Fitting the linear trend

The grids in Subsections 4.1.1 and 4.1.2 summarize all trends to be seen in terms of ϵ_p and τ_a impacting capture into MMR. Now it is of interest to see what the slope at each k-value is and how it compares to the adiabatic condition. This slope gives how τ_a and ϵ_p relate to each other for a given k. To find the slope the transition between MMRs was found, as given in Figures A.11 and A.12 in Appendix A.3, and fitted using a least-square polynomial fit with `polyfit` for the transitions up to $k = 9$ at only the power law trend. For all cases higher k than that cannot be fitted due to unclear transitions. On a linear scale the equations of the fitted lines are of the form

$$\tau_a = B_k \epsilon_p^{A_k}. \tag{4.5}$$

The two coefficients A_k and B_k are given in Tables 4.1 and 4.2 for respective grid. The lines within the same grid with different k should have the same slope, but in numerical simulations where the transitions are not perfect that is not exactly possible. However, we can see that A_k is otherwise independent of k. Thus, A_k for the respective grid is based on the mode or the result from the clearest transition in k (the 2:1, 3:2 and 4:3). The higher k transitions give a less good fit, but the overall fit is good with low errors of 10^{-5} to 10^{-3} and agrees well among 4-5 values of k out of nine in total. The only dependency in k is in the B_k coefficient, thus we plot B_k as function of k (see Figures 4.9 and 4.10). These points are then fitted by a power law fit (using `polyfit` again) of the form

$$B_k = dk^b, \tag{4.6}$$

where $b = -2.37$ and -2.88 for respective grid (in the same order as the plots).

Table 4.1: Fitted coefficients of the dependency between τ_a and ϵ_p, for each resonance index up to index $k = 9$, for the 2D grid 4.5.

Fixed inner planet			
k	MMR	A_k	$\log_{10}(B_k)$
1	2:1	−1.21	−1.84
2	3:2	−1.21	−2.49
3	4:3	−1.23	−2.85
4	5:4	−1.24	−3.13
5	6:5	−1.26	−3.28
6	7:6	−1.29	−3.64
7	8:7	−1.33	−3.91
8	9:8	−1.29	−3.98
9	10:9	−1.29	−3.89

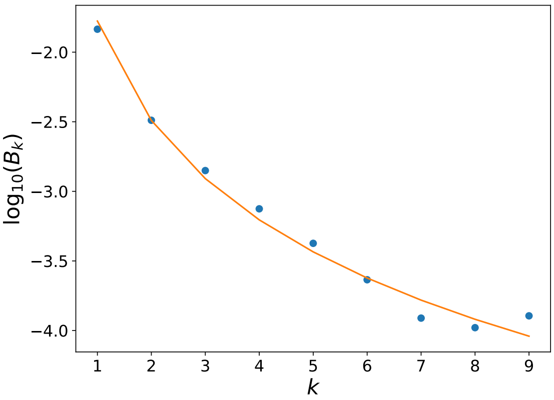

Figure 4.9: B_k as function of k in logarithmic scale, where we get the separation between resonances and how B_k depends on k.

Table 4.2: Fitted coefficients of the dependency between τ_a and ϵ_p, for each resonance index up to index $k = 9$, for the 2D grid 4.6.

Moving inner planet			
k	MMR	A_k	$\log_{10}(B_k)$
1	2:1	-1.14	-0.07
2	3:2	-1.20	-0.36
3	4:3	-1.23	-0.51
4	5:4	-1.26	-0.61
5	6:5	-1.27	-0.69
6	7:6	-1.29	-0.76
7	8:7	-1.30	-0.80
8	9:8	-1.33	-0.90
9	10:9	-1.34	-0.92

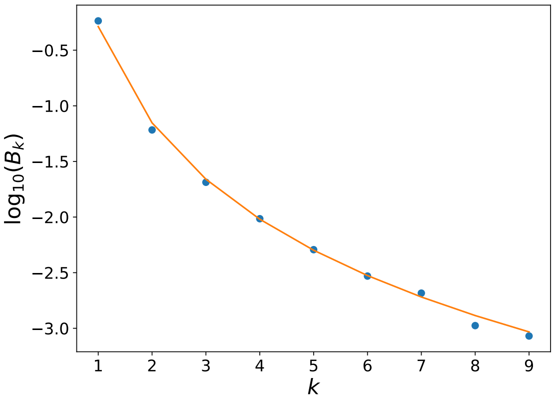

Figure 4.10: B_k as function of k, where we get the separation between resonances and how B_k depends on k.

These values could be obtained analytically but Batygin (2015) found steeper slopes, larger exponent of dependency on ϵ_p than shown here. That is, $\tau_a \propto \epsilon_p^{-4/3} k^{-14/9}$ as shown in Subsection 2.2.2. Ogihara and Kobayashi (2013) suggests the same dependency, $\tau_{lib}/\Delta t \propto \epsilon_p^{-4/3}$. The slopes found for each grid are all close to the one suggested in Batygin (2015); Ogihara and Kobayashi (2013), but it is not quite the same and the difference cannot be attributed to error margins or the approximation f_{res}. However, because the difference is so small it can be concluded that it does not fully disagree. That is, the adiabatic criterion from Batygin (2015) works for the constant setting, but either with a slightly smaller slope as seen here, or with a higher number than one, for c in $\tau_{lib}/\Delta t \lesssim c$ as seen in Figures 4.3 and 4.4. Investigating this by changing the slope in the adiabatic curves of Figure 4.3, confirms that the smaller slope works better. However, c still needs to change but to a value that makes more sense (see Figure 4.11). $\tau_{lib} < 0.75\Delta t$ is easier to satisfy than $\tau_{lib} < 5\Delta t$, because it does not require a very short τ_{lib} to fit the transitions well.

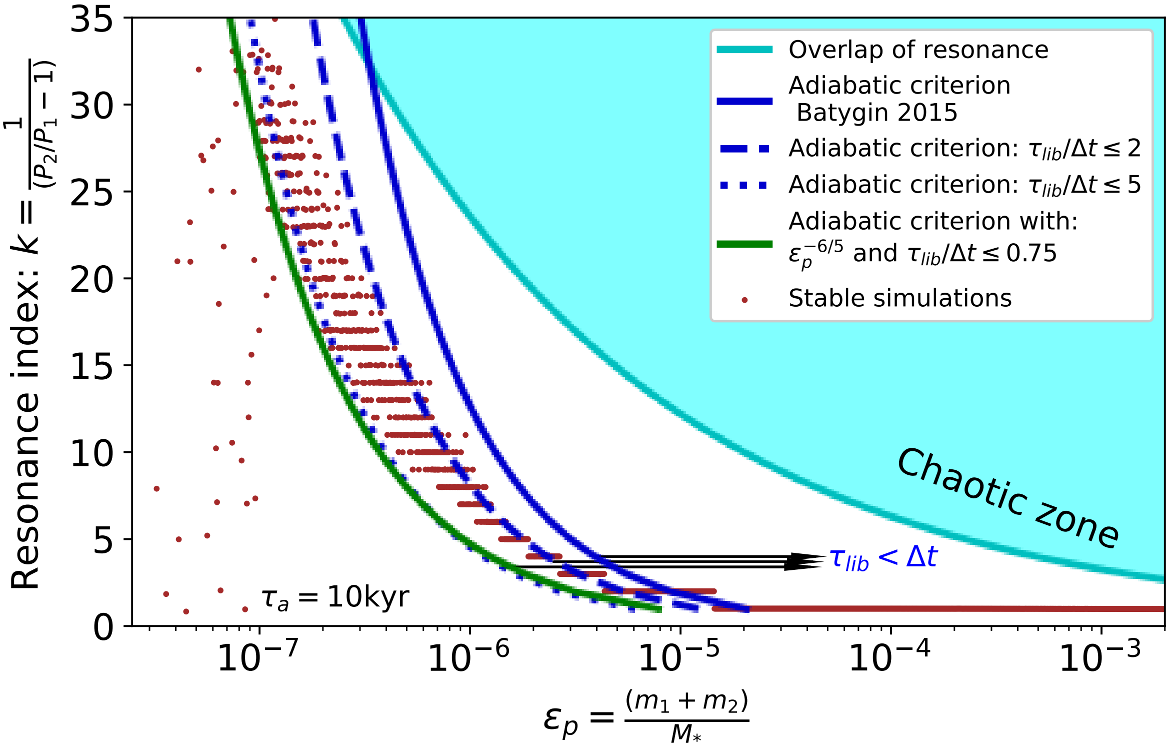

Figure 4.11: The same simulations as in Figure 4.3, but here I have included the adiabatic condition with the slope of $1.2 = 6/5$ as found by fitting the 2D grids.

Lastly, the investigations presented in this chapter show clearly that it is indeed easy to capture planets into a MMR and the outcome of capture can be drastically changed by tweaking the involved parameters ϵ_p and τ_a.

Chapter 5 - Type I migration

We aim at making the same type of investigations as in chapter 4 but in the context of type I migration: How the planetary mass and damping timescale impact MMR capture. However, since the damping timescale is no longer constant, instead given by Equation (2.23) it too depends on parameters of its own – planetary mass, orbital period, Σ_0 and h_0– which determine the magnitude of τ_a.

Firstly, we need to note that the orbital evolution has the same overall behaviour as in Figure 4.1 for constant migration, but on different timescales now that we are using type I migration prescription (Cresswell and Nelson, 2008; Ataiee and Kley, 2021). The speed of migration is mainly determined by Σ_0, h_0 and planet mass. The Type I migration prescription used here was described in Subsection 3.1.1. The planetary mass range is kept the same as for the controlled setting, while the damping timescales are changed by varying the migration parameters Σ_0 and h_0. The disk profile is isothermal with $s = 1$ and a flaring index $\beta = 0.25$ as suggested by Pichierri et al. (2018). Additionally, convergent migration is believed to be common and MMR encounter is guaranteed with this model, for low eccentricities (Cresswell and Nelson, 2008). If there is damping of eccentricity then capture into MMR does not depend on initial e, which will always be roughly zero at MMR encounter (Mustill and Wyatt, 2011; Ogihara and Kobayashi, 2013). Thus, initial eccentricity is again kept at zero.

The following investigation was conducted to see how the damping timescale changes with a few representative combinations of h_0 and Σ_0, see Figure 5.1. This was done in attempt to simplify the problem, instead of varying both h_0 and Σ_0.

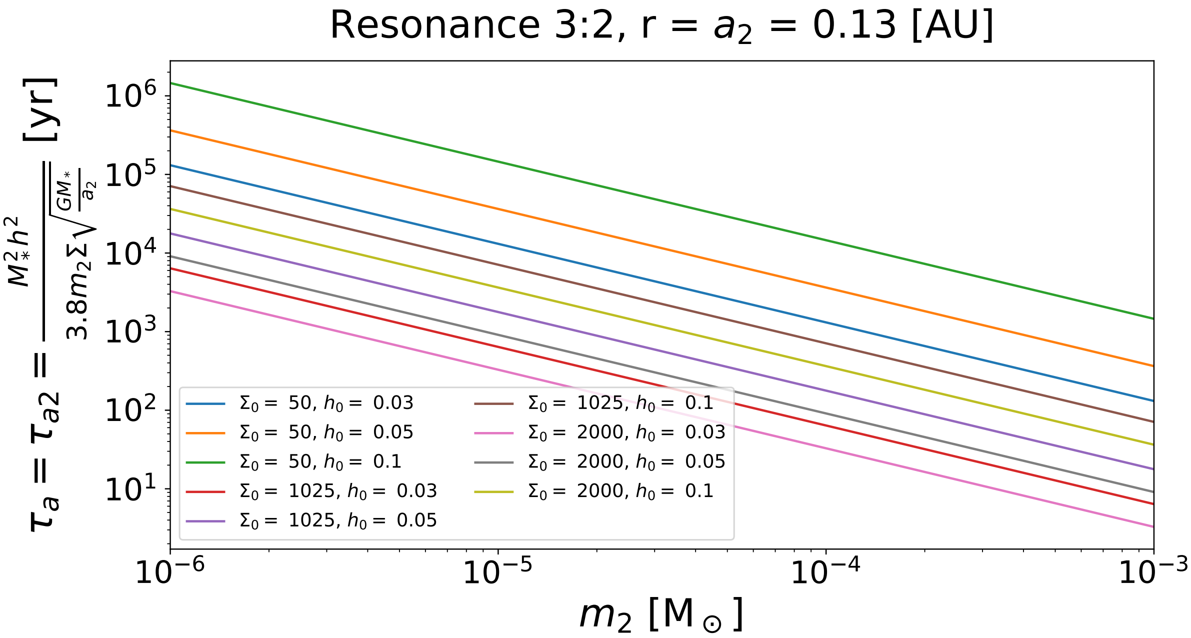

Figure 5.1: τ_a as function of ϵ_p for type I migration. Here we test how τ_a changes while varying the surface density at 1AU, Σ_0 in units of g/cm^2 and the aspect ratio, h_0 at 1 AU. The inner planet is here fixed at the inner disk edge so that $\tau_a = \tau_{a2}$. The distance from the star, r, is kept at 0.13AU which is at the 3:2 MMR.

The first thing to note is that for bigger planets Type I migration is faster, and it is less efficient for smaller planets (Cresswell and Nelson, 2008; Pichierri et al., 2018). Looking at the different surface densities, Σ_0, we see that a high value means faster type I migration, as expected by simply looking at the equation. In other words more gas means more angular momentum transfer and faster migration, especially if the planet mass is large as well. However, if the aspect ratio at 1AU, h_0, is large while keeping the same Σ_0, then τ_a is long with the same overall behaviour over the full mass range, as expected by the equation. Moreover, we see that increasing Σ_0 gives the same results as decreasing h_0. In this spirit one can choose to keep h_0 constant at a reasonable value and vary Σ_0 over a wide range. In this project it is again not of interest to stay realistic. Instead, we want to see the full dynamical range and different scenarios. For this reason Σ_0 will be varied over a wide range, with $h_0 = 0.033$ based on Pichierri et al. (2018). In the same paper $h_0 = 0.05$ at 5.2AU as supported by observations (Bell et al., 1997), meaning $h_0 = 0.033$ at 1AU.

As in the previous chapter, the first thing to look at is the planetary mass by plotting the resonance index as function of ϵ_p, as shown in Figure 5.2 for five different values of Σ_0, with otherwise same conditions as explained in Section 3.2.

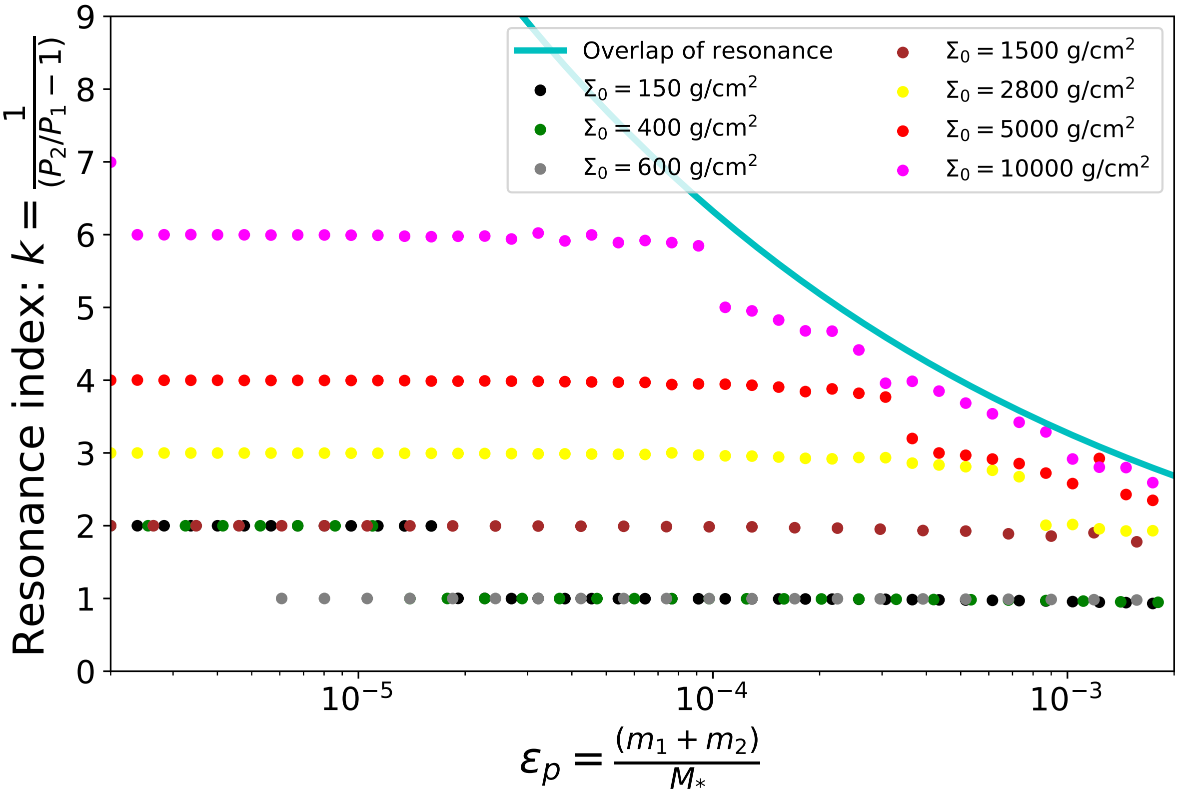

Figure 5.2: Resonance index at which a system with different ϵ_p value is captured, for five different values of Σ_0, $m_1 = m_2$ and the inner planet fixed at the inner disk edge.

Firstly, Σ_0 has a strong impact on capture into MMR as expected, since it affects the migration timescale. This was confirmed by Papaloizou and Szuszkiewicz (2005), where surface density was also varied over a few different values. High surface density leads to capture into higher k, since τ_a is then short. However, Ataiee and Kley (2021) found that higher Σ_0 only speeds up the evolution of the system, it does not affect the final configuration. However, they only test two values of surface density $2 \cdot 10^{-4}$ and $4 \cdot 10^{-4} \mathrm{M}_\odot/\mathrm{AU}^2$, which is not a large difference, and they use two nonequal mass planets. Whereas, in this project I vary Σ_0 over a wide range for two equal mass planets, and so it is not a direct comparison with Ataiee and Kley (2021) or an indication that they disagree with my findings. In my simulations, increasing Σ_0 in general leads to capture into higher resonance index similar to decreasing τ_a in the constant setting. Secondly, when Σ_0 is small, $< 1500\mathrm{g/cm}^2$, there is an indication of weak mass dependency. Such values result in a long τ_a, which as we saw in the controlled setting means low k-values for all ϵ_p. For such Σ_0 in this case only the 2:1 and 3:2 MMRs are occupied. The controlled setting showed that even if the inner planet is fixed at the inner disk edge where τ_{lib} is shorter, the highest occupied k is still higher than two. Thus, this must be further investigated to see the power law and determine if any over effects are at play.

On the other hand, as Σ_0 is increased above 600 g/cm^2, there is no mass dependency. All ϵ_p values fall into the same higher k MMRs, unlike the controlled setting. Here, decreasing τ_a does not mean more systems in different higher k. This is a surprising finding since mass also affects migration timescale and other studies have not seen lack of dependency on ϵ_p. Moreover, this contradicts the adiabatic condition. As seen in Subsection 2.4.1 the adiabatic condition suggests that the mass dependency for type I migration is $\Sigma_0 \propto \epsilon_p^{1/3}$. According to Batygin (2015) the condition cannot be satisfied if Σ_0 is large, because such Σ_0-values mean fast migration rate. Thus, the time it takes to cross the resonance width is much shorter than the libration timescale.

A similarity with the controlled setting in Chapter 4 is that decreasing τ_a again means capture into higher k and more chaotic motion due to overlap of resonances. We see the impact of overlap for larger masses and the higher Σ_0 values. These are the systems close to the overlap curve that bend over or disconnect from the rest of the systems, for the four largest Σ_0 values. This is because overlap of resonances still depends on the mass and the spacing between the planets. When Σ_0 is at such high values, the systems move closer even for large ϵ_p. Thus, not even the outermost MMR is safe from overlap, such systems are chaotic and not in a MMR.

5.1 2D grids

The first simple tests with 1D plots give clues about what is happening in terms of how ϵ_p and Σ_0 affect capture, as well as how Type I migration, a realistic prescription, compares to the controlled setting with constant migration. However, to properly see all the trends one must go about it the same way as in Chapter 4 and use 2D grids.

5.1.1 Capture at inner disk edge

The first 2D grid, presented in Figure 5.3, shows a controlled case where the inner planet is trapped at the inner disk edge. The ϵ_p range is the same as in previous chapter, while Σ_0 is varied between $400 - 50000$g/cm^2, roughly $\tau_a = 10^5$ to 10 years. Thus, the full dynamical range is visible as for the controlled setting. This grid shows how Σ_0 and ϵ_p relate to each other and impact capture into MMR. The lower limit of Σ_0 is no longer 150 g/cm^2, since as seen in the 1D plots, the lower values of Σ_0 all show the same trend over a wide range. This way we can see all tendencies without integrating many systems with such long τ_a, to save computational time.

Note also that the chaotic and unstable systems were excluded with the same criterion as in the other grids. We always use the final values, at the end of integration, to apply the criteria and exclude unstable systems. Moreover, the Hill unstable systems were also directly excluded using the same arguments and criterion as shown in Section 4.2. These exclusions were supported by the 1D plot, where we see these type of systems to be unstable or chaotic.

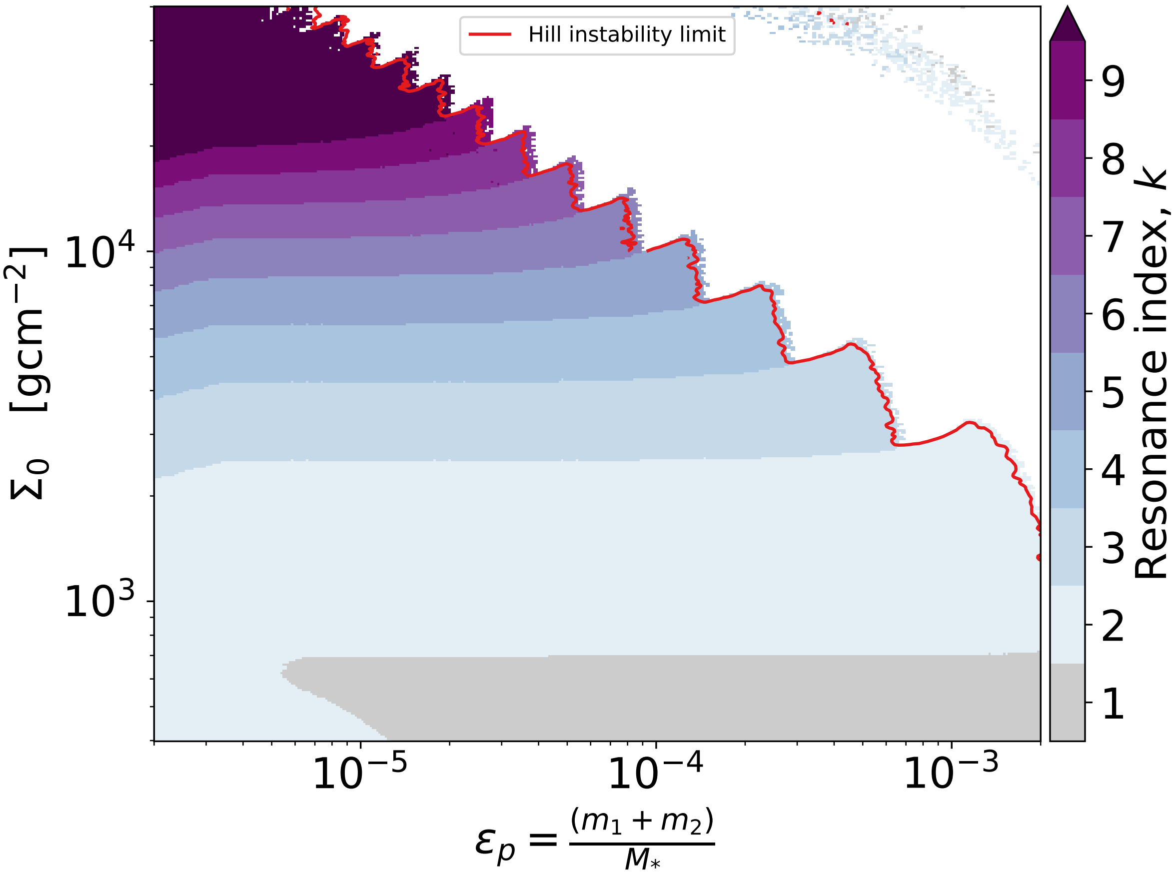

Figure 5.3: A 2D grid of Σ_0 as function of ϵ_p, where the inner planet is fixed at the inner disk edge and the outer migrates via Type I migration. The level curve in red marks out the Hill stability limit, showing which systems have been excluded. Note that the systems, in the top right corner are discussed later in the text.

Firstly, we see that the trend for all Σ_0 values is constant in ϵ_p when ϵ_p is above a certain value. Instead of a power law trend in ϵ_p, here we see that for a given Σ_0 all systems fall into the same MMR. Note that it might seem as though there is a shallow slope for higher k, but that is due to low resolution, and it is difficult to investigate it further since it is at high k where other mechanisms are involved; close to the Hill instability limit and the chaotic zone. For the smallest masses there is a non-constant trend with a positive slope and lower value than seen in Figures 4.5 and 4.6. In Subsection 2.4.1 it was shown that $\Sigma_0 \propto \epsilon_p^{1/3} k^{14/9}$ (Batygin, 2015). Fitting this trend in the same way as shown in Section 4.3, see Figure A.13 in Appendix A.3, we see that the slope is $A_k \approx 0.2$. This value for the slope is close to the one from the adiabatic condition and matches well with the results from Chapter 4 as we expect. Moreover, again I fit the coefficient B_k as function of k and get a slope of $b \approx 1.24$, which is also close to the one from the adiabatic condition. Overall, the errors for the fits in this section are only slightly larger than for the constant migration trend, $10^{-4} - 10^{-3}$, but that is still low and not a concern. Note also that a non-constant trend seems to be present for large ϵ_p. However, this shift in slope is simply due to the proximity to the Hill instability limit, as we have seen to occur in the constant migration case too.

Table 5.1: Fitted coefficients of the dependency between Σ_0 and ϵ_p, for each resonance index $2 \geq k \leq 9$, for the 2D grid 5.3.

Fixed inner planet			
k	MMR	A_k	$\log_{10} B_k$
2	3:2	0.21	4.57
3	4:3	0.21	4.78
4	5:4	0.20	4.89
5	6:5	0.20	5.04
6	7:6	0.20	5.12
7	8:7	0.20	5.22
8	9:8	0.20	5.30
9	10:9	0.20	5.39

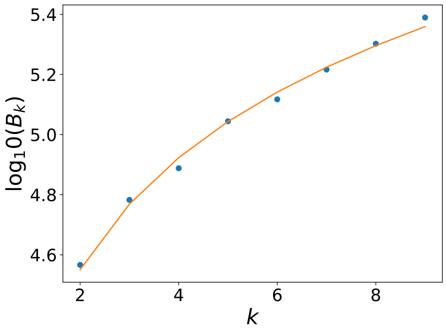

Figure 5.4: B_k as function of k in logarithmic scale, where we get the separation between resonances and how B_k depends on k.

Lastly, the non-linear small transition visible between 2:1 and 3:2 for low Σ_0 values does not follow any trend. The belief is that this is overstability for the 2:1 MMR not another mass dependency trend; systems with a certain mass and smaller escape from 2:1 and into 3:2. Looking at a few systems in this region we confirm that this is indeed the overstable region (see Figure A.9 in Appendix A.2). These type of systems will be discussed more in connection with the next grid where they are more pronounced. Moreover, there are a few systems of large ϵ_p and Σ_0 which are not cut out by any of the criteria. These are systems that at the end of integration time fulfill the Hill stability criteria as they are at large periods with large enough separation. Moreover, they were close to a commensurate period ratio and as such were averaged to the closest integer k, posing as systems captured into a low k MMR. The simulation outputs for a set of systems in this region (see Figure A.6 in Appendix A.1) show that they are chaotic and that the period ratio varies slightly with time even at the end of integration. Thus, they are not systems that are in MMR or that will remain stable.

5.1.2 Capture while migrating

The second grid in Figure 5.5 shows a case where both planets migrate from [0.5, 0.85] AU. Here Σ_0 is varied from 700 g/cm^2 or roughly $\tau_a = 10^5$ years to the same upper limit at ≈ 50000 g/cm^2. The outer planet here is twice as massive as the inner, so that it moves faster and the same type of convergent migration as in the controlled setting can happen: both planets migrate inwards, where the inner planet reaches close to the inner disk edge or at the inner disk edge, while the outer catches up and is captured into a MMR. Again, the chaotic systems due to overlap of resonances and the Hill unstable systems are directly removed.

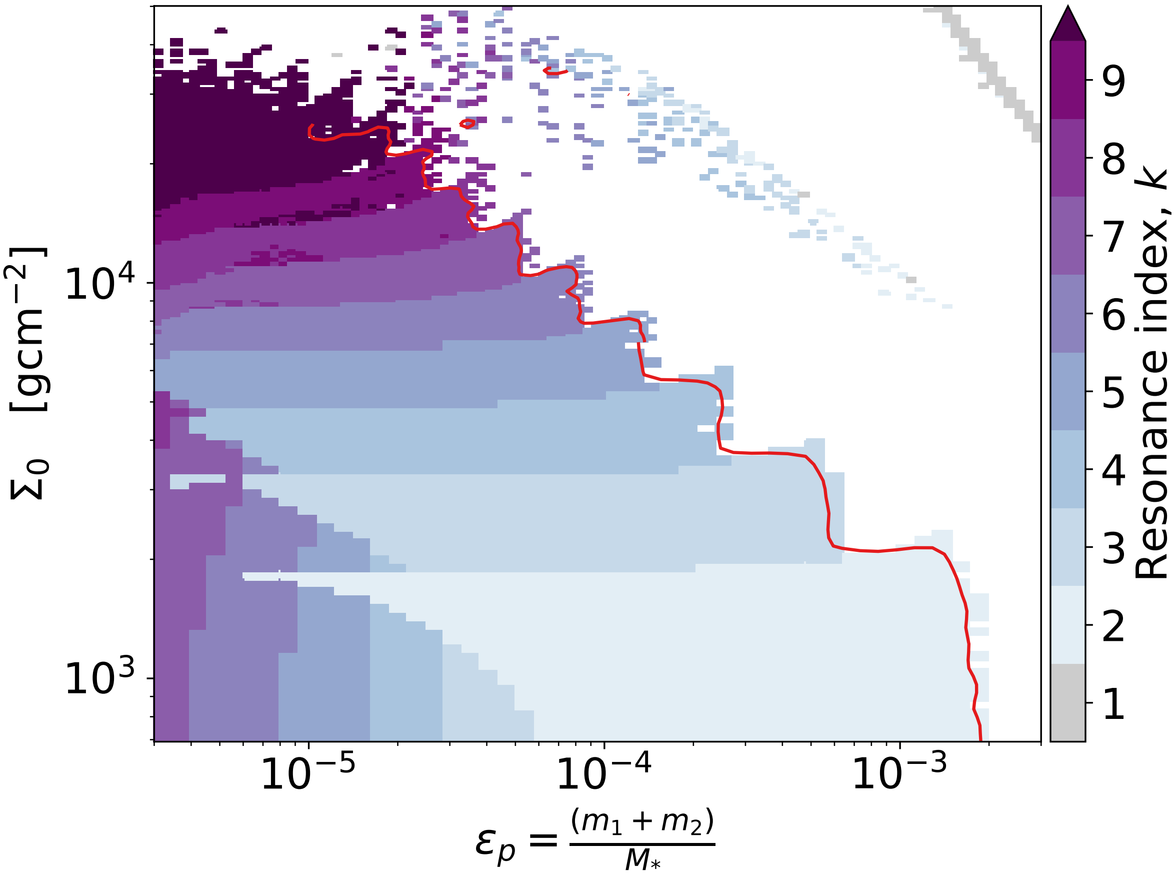

Figure 5.5: A 2D grid of Σ_0 as function of ϵ_p. Where both planets migrate via Type I migration. The level curve in red again marks out the Hill unstable region. Those systems that are Hill stable past the instability limit will not remain stable as discussed for the previous grid.

Firstly, we confirm the trend of no mass dependency for larger ϵ_p values. Again, the only non-constant trend is at small ϵ_p and $\Sigma_0 > 7000$g/cm^2. However, unlike in the fixed inner planet case, here this trend is harder to see and fit (mostly because of the low resolution).

Moreover, we again see outliers that are the result of scattered systems that are Hill stable at the end of this integration time but do not remain so. Same as in the previous grid these systems are also averaged to the closest integer k posing to be in MMR, even though they are chaotic (see Figure A.7 in Appendix A.1).

A significant difference between this grid and the fixed inner case grid, is the strange behaviour at small ϵ_p and low Σ_0. It seems there is a vertical transition into different resonances of higher k with decreased mass. These systems are likely to be overstable, that is they show the tendency to escape MMRs one by one, after spending some time in the first encountered MMR that is natural for that combination of the parameters. As explained in Deck and Batygin (2015) this behaviour occurs for nonequal mass planets as is the case here. Overstability depends on mass and k, smaller masses will escape from and to higher k than slightly larger overstable planets. This is why we see so many transitions in the overstability regime instead of just one as in the fixed inner planet case, where overstability is only present for the 2:1 MMR. This behaviour was not investigated in detail in this thesis, but a quick test was done to show so is the case here, see Figure A.10 in Appendix A.2.

Even here, we also confirm that when located closer to the star, as is the case in Figure 5.3, more systems are captured into lower k MMRs compared to when the planets are captured into a MMR further from the star as in Figure 5.5. The adiabatic condition is easier to satisfy for higher k when the periods are smaller. Additionally, the chaotic motion that leads to unstable systems for largest values of Σ_0 and smallest masses (upper left corner) is not visible when the inner planet is fixed. Nonetheless, one can keep in mind one small detail: in reality even gas rich disks can with time reduce in surface density during disk lifetime, at which point the adiabatic condition can be satisfied for the systems that are first scattered and start their migration process all over.

5.2 Observational implications

The results of this project can be applied to observations, to find connections between the final state of a planetary system and its early evolutionary environment. Moreover, the results of this chapter have shown that MMR capture is consistent with Type I migration. Thus, strongly indicating that Type I migration exists and is vital for MMR capture, which is indeed observed among exoplanets.

Investigating capture into MMR with different initial conditions on planetary mass and surface density with a realistic migration model as done here, has shown what to expect in terms of final architecture for given initial conditions. In observations, we most often observe the final state of a system, which we can then connect to initial conditions by consulting the findings in this project. For example, the general trends suggest that a two-planet system observed in a low k MMR, likely has large mass planets or the planets migrated very slowly. Moreover, this suggests that the disk was either thick and so provided enough material for the formation of large planets and fast migration, or the disk was thin and so did not provide an environment for sufficient migration.

Furthermore, observations of exoplanetary systems show that most resonant planets are in 2:1 and 3:2 MMR, and some in 4:3. There are few systems in closer resonances, MMRs with $k > 3$ are rare. In all the grids it was confirmed that most occupied MMRs are the 2:1, 3:2 and 4:3. The higher k MMRs require high disk surface densities. Thus, if compact MMRs are rare, then in general disks with $\Sigma_0 > 4000\text{g/cm}^2$ are also rare. According to this, systems found in $k > 4$ would have: 1) Planets with masses over a large range that evolved in a gas rich disk, $\Sigma_0 > 6000\text{g/cm}^2$ (as suggested by the constant trend portion of the grid in Figures 5.3 and 5.5). 2) Planets with small mass and high Σ_0 which provided fast migration (suggested by the non-constant trend in the same grids). A real case example is the Kepler 50 system with two similar mass planets (roughly 8.2 and 8.9 $\text{M}_\oplus$ or $2.7 \cdot 10^{-5}$ and $2.5 \cdot 10^{-5}\text{M}_\odot$) near a 6:5 MMR, with a period ratio of 1.205 (Steffen, 2013). Knowing the mass of the planets gives a good idea of what the surface density in the young PPD they formed and evolved in could have been. Assuming both planets migrated towards the inner disk edge, the general trend of the 2D grid 5.5 suggests a surface density range of roughly $5000 < \Sigma_0 < 6000\text{g/cm}^2$.

Moreover, the 2D grids of type I migrating systems show that for $1000 < \Sigma_0 < 3000$, taken as realistic values of surface density for a young PPDs in many papers, show indeed that such disks provide less migration. Thus, the systems end up in 2:1, 3:2 and 4:3 if initial position of the outer planet was just outside the 2:1 MMR. If initial position was closer to the star (outside a higher k MMR instead) it is possible that for the same Σ_0 range a system can end up in a 5:4 or 6:5 MMR instead. Higher Σ_0 does naturally result in more compact MMRs in our results, but such values are either rare for PPDs or even unrealistically high. A $\Sigma_0 > 10000\text{g/cm}^2$ is too high even for young PPDs. Further, suggesting that the rare but observed systems in compact MMRs more likely started migrated from smaller distances to the host star, or with smaller initial separation, rather than migrating fast in a very dense disk. If they started with an initial separation just outside the 2:1 MMR, then for the same range, $1000 < \Sigma_0 < 3000$, they would not have migrated as close. The general trends from the grids say that stable capture would in such case happen at a lower k MMR for any planetary mass.

The take home message is that for any two equal-mass planet system observed in our Universe, if in a MMR we can find out what range of values Σ_0 could have had in the PPD these planets formed and evolved. If we are also able to infer the planetary mass to an acceptable accuracy, it will be possible to provide specific values or a narrow range of values for Σ_0, which can be used to find other properties of the PPD. An insight in the properties of the PPD is invaluable, because it can provide important knowledge that can help constrain formation and evolution models. The goal is still to correctly predict observational outcomes of MMR using theoretical models.

Chapter 6 - Conclusions

In this project I have simulated the co-planar three body system, undergoing convergent inwards migration, with a wide range of values for the damping timescale of the semi-major axis and initial planetary masses relative to the central star. The investigation was divided into two parts, the first using constant damping timescales and the second using Type I migration. Within each part I have studied how capture depends on these parameters for a controlled setting where the inner planet is fixed at the inner disk edge, and where both planets migrate.

To identify at which MMR the planets with each combination of the parameters investigated are trapped, I used the resonance index, a function of orbital period ratio. Thus, when plotting resonance index as function of parameters, the systems will fall into integer values of k by definition. The results from constant migration show that the transition between capture into two different index MMRs follows a relationship between τ_a and ϵ_p, with a power law of $\tau_a \propto \epsilon_p^{-1.2}$. The slope of the power law relationship is thus slightly lower than that proposed analytically in Batygin (2015) and supported by other works from the literature, which is $\tau_a \propto \epsilon_p^{-4/3}$. Additionally, I show that for these simulations $\tau_{lib}/\Delta t \lesssim 1$ does not fit all transitions in k. Instead, when using the lower power law value found by fitting the 2D grids and $\tau_{lib}/\Delta t \lesssim 0.75$, the adiabatic condition fits all simulations well. The general trend says that overall longer τ_a or larger ϵ_p means capture at outermost MMRs, while the opposite holds for shorter τ_a and smaller ϵ_p.

In the case of Type I migration, we have seen from other sources, the adiabatic model in Batygin (2015) and just by looking at the definition of the Type I migration timescale, that both Σ_0 and ϵ_p should impact capture into MMR. We do see that Σ_0 has a strong impact on capture. It can be increased to high values before all systems become unstable, and higher Σ_0, longer τ_a, leads to capture in higher resonance index. The numerical simulations also show a significantly different qualitative behaviour for larger masses; there is no mass dependency. This unexpected result is in tension with the proposed quantitative analytical models. The solution might lie in the theory, thus motivating the need to revisit the analytical model. Moreover, from the results in the controlled case, the non-constant trend is positive with a power law of $\Sigma_0 \propto \epsilon_p^{0.2}$, which is again close to the one suggested by the adiabatic model in Batygin (2015). This result was also expected from the first results with constant migration in Chapter 4.

In both settings we saw that many systems become unstable due to overlap of resonances at closely spaced resonances, and chaotic at MMRs with larger separations. These systems are not in a MMR. Moreover, we observed that there were vertical transitions at shorter τ_a (higher Σ_0), which we confirmed to be due to Hill instability. Beyond these points in terms of ϵ_p the power law trend cannot be maintained. Instead, the systems are in the Hill unstable regime where only ϵ_p and the spacing between the planets matter. The arguments of overlap of resonances and Hill instability and their impact are valid for Type I migration as well. In these grids we again see that some systems are not in a MMR or stable and do not follow the trends of the stable systems. Thereby, observed systems with combinations of parameters in this regime can be concluded to be chaotic or unstable, thus not expected to be in a MMR after disk removal or at all. Whereas, for systems stable and in outermost MMRs, we expect stability over a wide range of ϵ_p and τ_a, since the outermost MMRs are in general easier to be trapped into and most systems occupy these MMRs. This presents a small clue as to why 2:1 and 3:2 are the most common MMRs among observed exoplanets. We also confirm that capture into MMR occurs for many systems and early on, when using the model of convergent migration. Moreover, we have seen that when both planets migrate, thus have nonequal mass, there is a regime of overstability for small ϵ_p- and Σ_0-values (the vertical transitions in Figure 5.5). That is, temporary capture in the first encountered MMR followed by escape to closely spaced MMRs. Overstability is expected to exist for such values of the parameters, when the planets have nonequal masses (Deck and Batygin, 2015). Overstability is of value but due to limited time it was not investigated in detail here.

From all the results we can in general conclude that systems observed at tighter MMRs either started with wide separations but migrated too fast, or were too small to be captured into outermost MMRs. Even if not directly tested here, we can say from the trends that tighter MMRs can also be a result of a system formed at a smaller period ratio, which migrated slowly or had large planetary mass. Such a system is naturally captured at one of the first outermost MMRs, not 2:1, it encounters during inward migration.

In summary, both settings show that some systems are chaotic or unstable instead of in a MMR, and the most occupied are the 2:1, 3:2 and 4:3 MMRs over a wide range of values. Moreover, realistic values of τ_a or Σ_0 lead to capture into the outermost MMRs. With the findings here, about how these initial conditions impact capture into MMR, we can constrain theoretical models even better. Additionally, taking into account both instability criteria presented in this project and other mechanisms that break resonance from works in the literature, we will be able to correctly represent observations of MMRs in the future.

Furthermore, these results can provide information, a sort of reference guide if you will, that can connect the final state of a system with a similar setup, to its evolutionary environment and history. In other words, we can place the final state of an observed system in the context of this project and get insight into the disk properties that governed the evolution of the planets and so the final architecture, whether the system ended up stable in a MMR or not.

Equal mass studies like this one to better understand the impact of initial conditions are important, because such systems exist in observations. Super-Earth systems, the most common planet in multi-planetary systems, are cases of comparable mass planets

(Weiss et al., 2018). Nonetheless, to complete this study and utilize all the information to better understand observations and connect to initial environment of these systems, future work could be to look at various mass ratios of the planets. Doing so would reveal if the qualitative behaviour is the same and, whether the other aspects of MMR dynamics have a stronger overall impact than we have seen here. Moreover, it would be of interest to set the inner disk edge further away at various distances to see if the trends change in any way, and how important the period dependency is for τ_{lib}. After all, we see indications of different outcomes already when both planets migrate and capture occurs at distances further away from the star. Lastly, it is important to also test different disk profiles to make sure this type of behaviour is seen for different type of migration environments. Especially, important is to show that the no-dependency on planetary mass for Type I migrating planets is not seen only when applying a static and simple disk profile. It is also worth noting that this work presents results for a three-body system only. Therefore, it is of interest to investigate the same set of initial conditions for a system with more planets in the same way, to see if the results differ and how. In this manner we will have a comprehensive numerical insight that can connect the final state of an exoplanetary system to the initial disk properties. Thus, revealing the evolutionary environment for a wide and diverse sample of real systems, to better understand their overall formation and evolution.

Bibliography

Armitage, P. J. (2010). *Astrophysics of Planet Formation.* Cambridge University Press, Cambridge.

Armitage, P. J. (2017). Lecture notes on the formation and early evolution of planetary systems. *ArXivastro-Ph0701485.*

Armitage, P. J. (2018). A brief overview of planet formation. *ArXiv180310526 Astro-Ph*, pages 2185–2203.

Armitage, P. J. (2020). *Astrophysics of Planet Formation.* Cambridge University Press, second edition.

Ataiee, S. and Kley, W. (2021). Pushing planets into an inner cavity by a resonant chain. *A&A*, 648:A69.

Batygin, K. (2015). Capture of Planets Into Mean Motion Resonances and the Origins of Extrasolar Orbital Architectures. *ArXiv150501778 Astro-Ph.*

Batygin, K. and Adams, F. C. (2017). An Analytic Criterion for Turbulent Disruption of Planetary Resonances. *AJ*, 153(3):120.

Batygin, K. and Morbidelli, A. (2012). DISSIPATIVE DIVERGENCE OF RESONANT ORBITS. *AJ*, 145(1):1.

Batygin, K. and Morbidelli, A. (2013). Analytical Treatment of Planetary Resonances. *A&A*, 556:A28.

Bell, K. R., Cassen, P. M., Klahr, H. H., and Henning, T. (1997). The Structure and Appearance of Protostellar Accretion Disks: Limits on Disk Flaring. *ApJ*, 486(1):372–387.

Brasser, R., Matsumura, S., Muto, T., and Ida, S. (2018). Trapping low-mass planets at the inner edge of the protostellar disc. *ApJ*, page 8.

Cresswell, P. and Nelson, R. P. (2008). Three-dimensional simulations of multiple protoplanets embedded in a protostellar disc. *Astron. Astrophys.*, 482(2):677.

Danby, J. M. (1962). *Fundamentals of Celestial Mechanics.* Macmillan.

De Pater, I. and Lissauer, J. J. (2015). *Planetary Sciences*. Cambrige university press, second edition edition.

Deck, K. M. and Batygin, K. (2015). MIGRATION OF TWO MASSIVE PLANETS INTO (AND OUT OF) FIRST ORDER MEAN MOTION RESONANCES. *ApJ*, 810(2):119.

Deck, K. M., Payne, M., and Holman, M. J. (2013). First Order Resonance Overlap and the Stability of Close Two Planet Systems. *Astrophys. J.*, 774(2):129–129.

Delisle, J.-B. and Laskar, J. (2018). Tidal dissipation and the formation of Kepler near-resonant planets. *A&A*, 570:L7.

Delisle, J.-B., Laskar, J., and Correia, A. C. M. (2014). Resonance breaking due to dissipation in planar planetary systems. *A&A*, 566:A137.

Fabrycky, D. C., Ford, E. B., Steffen, J. H., Rowe, J. F., Carter, J. A., Moorhead, A. V., Batalha, N. M., Borucki, W. J., Bryson, S., Buchhave, L. A., Christiansen, J. L., Ciardi, D. R., Cochran, W. D., Endl, M., Fanelli, M. N., Fischer, D., Fressin, F., Geary, J., Haas, M. R., Hall, J. R., Holman, M. J., Jenkins, J. M., Koch, D. G., Latham, D. W., Li, J., Lissauer, J. J., Lucas, P., Marcy, G. W., Mazeh, T., McCauliff, S., Quinn, S., Ragozzine, D., Sasselov, D., and Shporer, A. (2012). TRANSIT TIMING OBSERVATIONS FROM *KEPLER* . IV. CONFIRMATION OF FOUR MULTIPLE-PLANET SYSTEMS BY SIMPLE PHYSICAL MODELS. *ApJ*, 750(2):114.

Fabrycky, D. C., Lissauer, J. J., Ragozzine, D., Rowe, J. F., Steffen, J. H., Agol, E., Barclay, T., Batalha, N., Borucki, W., Ciardi, D. R., Ford, E. B., Gautier, T. N., Geary, J. C., Holman, M. J., Jenkins, J. M., Li, J., Morehead, R. C., Morris, R. L., Shporer, A., Smith, J. C., Still, M., and Van Cleve, J. (2014). Architecture of Kepler's Multi-Transiting Systems. II. New Investigations with Twice as Many Candidates. *Astrophys. J.*, 790(2):146–146.

Fressin, F., Torres, G., Charbonneau, D., Bryson, S. T., Christiansen, J., Dressing, C. D., Jenkins, J. M., Walkowicz, L. M., and Batalha, N. M. (2013). THE FALSE POSITIVE RATE OF *KEPLER* AND THE OCCURRENCE OF PLANETS. *ApJ*, 766(2):81.

Gladman, B. (1993). Dynamics of Systems of Two Close Planets. *Icarus*, 106:247–263.

Goldreich, P. and Sciama, D. W. (1965). An Explanation of the Frequent Occurrence of Commensurable Mean Motions in the Solar System. *Monthly Notices of the Royal Astronomical Society*, 130(3):159–181.

Goldreich, P. and Tremaine, S. (1980). Disk-satellite interactions. *ApJ*, 241:425.

Haisch, Jr., K. E., Lada, E. A., and Lada, C. J. (2001). Disk Frequencies and Lifetimes in Young Clusters. *Astrophys. J.*, 553(2):L153–L156.

Izidoro, A., Bitsch, B., Raymond, S. N., Johansen, A., Morbidelli, A., Lambrechts, M., and Jacobson, S. A. (2019). Formation of planetary systems by pebble accretion and migration: Hot super-Earth systems from breaking compact resonant chains. *arXiv e-prints*, 1902:arXiv:1902.08772.

Izidoro, A., Ogihara, M., Raymond, S. N., Morbidelli, A., Pierens, A., Bitsch, B., Cossou, C., and Hersant, F. (2017). Breaking the chains: Hot super-Earth systems from migration and disruption of compact resonant chains. *Mon Not R Astron Soc*, 470(2):1750–1770.

Kepler, J. (1609). *Astronomia nova*. Pragae.

Lada, C. J. (1987). Star formation: From OB associations to protostars. 115:1.

Lambrechts, M. and Johansen, A. (2012). Rapid growth of gas-giant cores by pebble accretion. *A&A*, 544:A32.

Masset, F. S., Morbidelli, A., Crida, A., and Ferreira, J. (2006). Disk Surface Density Transitions as Protoplanet Traps. *ApJ*, 642(1):478–487.

Mayor, M., Marmier, M., Lovis, C., Udry, S., Ségransan, D., Pepe, F., Benz, W., Bertaux, J.-L., Bouchy, F., Dumusque, X., Curto, G. L., Mordasini, C., Queloz, D., and Santos, N. C. (2011). The HARPS search for southern extra-solar planets XXXIV. Occurrence, mass distribution and orbital properties of super-Earths and Neptune-mass planets. *ArXiv11092497 Astro-Ph.*

McNally, C. P., Nelson, R. P., Paardekooper, S.-J., Benitez-Llambay, P., and Gressel, O. (2020). Low-mass planet migration in three dimensional wind-driven inviscid discs: A negative corotation torque. *Mon. Not. R. Astron. Soc.*, 493(3):4382–4399.

Morbidelli, A. (2002). *Modern Celestial Mechanics: Aspects of Solar System Dynamics*. Taylor & Francis.

Mustill, A. J. and Wyatt, M. C. (2011). A general model of resonance capture in planetary systems: First and second order resonances. *Mon. Not. R. Astron. Soc.*, 413(1):554–572.

Mustill, A. J. and Wyatt, M. C. (2012). Dependence of a planet's chaotic zone on particle eccentricity: The shape of debris disc inner edges. *Monthly Notices of the Royal Astronomical Society*, 419(4):3074–3080.

Ogihara, M. and Kobayashi, H. (2013). Condition for Capture into First-order Mean Motion Resonances and Application to Constraints on Origin of Resonant Systems. *ApJ*, 775(1):34.

Papaloizou, J. C. B. and Szuszkiewicz, E. (2005). On the migration-induced resonances in a system of two planets with masses in the Earth mass range. *Monthly Notices of the Royal Astronomical Society*, 363(1):153–176.

Petigura, E. A., Marcy, G. W., Winn, J. N., Weiss, L. M., Fulton, B. J., Howard, A. W., Sinukoff, E., Isaacson, H., Morton, T. D., and Johnson, J. A. (2018). The California-Kepler Survey. IV. Metal-rich Stars Host a Greater Diversity of Planets. *Astron. J.*, 155:89.

Petit, A. C. (2019). *Architecture and Stability of Planetary Systems.* PhD dissertation, PSL university, Paris.

Pichierri, G., Morbidelli, A., and Crida, A. (2018). Capture into first-order resonances and long-term stability of pairs of equal-mass planets. *Celest Mech Dyn Astr*, 130(8):54.

Ramos, X. S., Charalambous, C., Benítez-Llambay, P., and Beaugé, C. (2017). Planetary migration and the origin of the 2:1 and 3:2 (near)-resonant population of close-in exoplanets. *A&A*, 602:A101.

Ramos, X. S., Correa-Otto, J. A., and Beaugé, C. (2015). The Resonance Overlap and Hill Stability Criteria Revisited. *Celest. Mech. Dyn. Astron.*, 123(4):453–479.

Rein, H., Hernandez, D. M., Tamayo, D., Brown, G., Eckels, E., Holmes, E., Lau, M., Leblanc, R., and Silburt, A. (2019). Hybrid symplectic integrators for planetary dynamics. *Mon. Not. R. Astron. Soc.*, 485:5490–5497.

Rein, H. and Liu, S.-F. (2012). REBOUND: An open-source multi-purpose N-body code for collisional dynamics. *Astron. Astrophys.*, 537:A128.

Rein, H. and Spiegel, D. S. (2015). IAS15: A fast, adaptive, high-order integrator for gravitational dynamics, accurate to machine precision over a billion orbits. *Mon. Not. R. Astron. Soc.*, 446:1424–1437.

Rein, H. and Tamayo, D. (2015). WHFAST: A fast and unbiased implementation of a symplectic Wisdom-Holman integrator for long-term gravitational simulations. *Mon. Not. R. Astron. Soc.*, 452:376–388.

Sarma, R., Baruah, K., and Sarma, J. K. (2006). IAU PLANET DEFINITION: SOME CONFUSION AND THEIR MODIFICATIONS. In *IAU Planet Definition*, page 8, Prauge.

Steffen, J. H. (2013). Kepler's missing planets. *Mon. Not. R. Astron. Soc.*, 433(4):3246–3255.

Tamayo, D., Rein, H., Shi, P., and Hernandez, D. M. (2020). REBOUNDx: A Library for Adding Conservative and Dissipative Forces to Otherwise Symplectic N-body Integrations. *Mon. Not. R. Astron. Soc.*, 491(2):2885–2901.

Tanaka, H. and Ward, W. R. (2004). Three-dimensional Interaction between a Planet and an Isothermal Gaseous Disk. II. Eccentricity Waves and Bending Waves. *ApJ*, 602(1):388–395.

Ward, W. R. (1997). Protoplanet Migration by Nebula Tides. *Icarus*, 126:261–281.

Weiss, L. M., Marcy, G. W., Petigura, E. A., Fulton, B. J., Howard, A. W., Winn, J. N., Isaacson, H. T., Morton, T. D., Hirsch, L. A., Sinukoff, E. J., Cumming, A., Hebb, L., and Cargile, P. A. (2018). The California-Kepler Survey. V. Peas in a Pod: Planets in a Kepler Multi-planet System Are Similar in Size and Regularly Spaced. *AJ*, 155(1):48.

Winn, J. N. and Fabrycky, D. C. (2015). The Occurrence and Architecture of Exoplanetary Systems. *Annu. Rev. Astron. Astrophys.*, 53:409.

Wisdom, J. (1986). Canonical Solution of the Two Critical Argument Problem. *Celest. Mech.*, 38:175–180.

Wisdom, J. and Holman, M. (1991). Symplectic maps for the N-body problem. *Astron. J.*, 102:1528–1538.

Wolszczan, A. and Frail, D. A. (1992). A planetary system around the millisecond pulsar PSR1257 + 12. *Nature*, 355(6356):145–147.

Xuan, J. W. and Wyatt, M. C. (2020). Evidence for a high mutual inclination between the cold Jupiter and transiting super Earth orbiting π Men. *Mon. Not. R. Astron. Soc.*, 497:2096–2118.

Zhu, W. and Dong, S. (2021). Exoplanet Statistics and Theoretical Implications. *ArXiv210302127 Astro-Ph*.

Zhu, W., Petrovich, C., Wu, Y., Dong, S., and Xie, J. (2018). About 30% of Sun-like Stars Have Kepler-like Planetary Systems: A Study of Their Intrinsic Architecture. *Astrophys. J.*, 860:101.

Appendix A - More interesting plots

Figures A.1 and A.2 are similar to Figures 4.3 and 4.4 in Chapter 4, but here for both planets migrating. The qualitative behaviour is the same. But migrating from further away from the star means the adiabatic condition is not satisfied at the same indices for the same ϵ_p as in the figures in Chapter 4. Again, we see that the adiabatic condition fails to fit the transitions, even with larger value for $c = \tau_{lib}/\Delta t$, until it no longer becomes reasonable to increase c further even if it might be arbitrarily chosen.

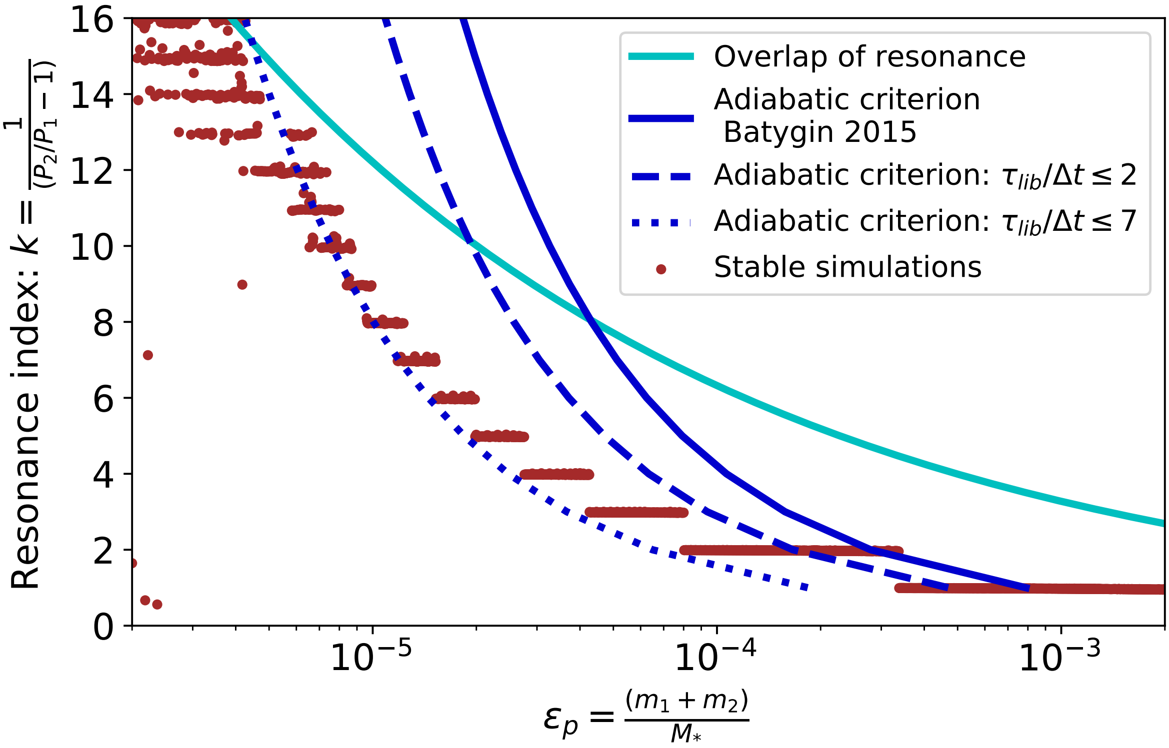

Figure A.1: MMR index into which each system is captured as a function of ϵ_p. This is the case where the damping timescale is $\tau_a = 20$kyr and both planets are migrating from $a = [0.5, 0.85]$.

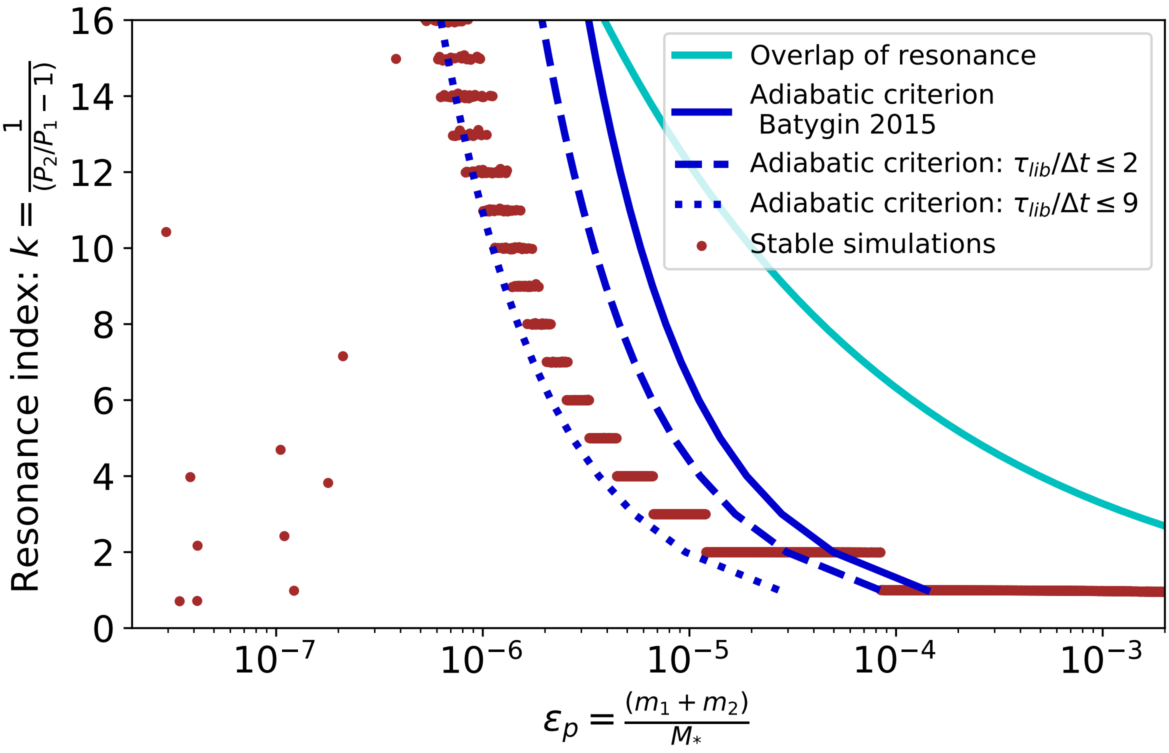

Figure A.2: MMR index into which each system is captured as a function of ϵ_p. Same case as above but for a shorter damping timescale $\tau_a = 2$kyr.

A.1 Examples of the behaviour of the outliers

The figure below shows an example of the two cases of outliers seen in the 1D plots of k as function of ϵ_p in the above plots and those in Chapter 4. I simply located a few examples in the region of outliers and plotted their period ratio evolution over time, the snapshots are thus less than in the other example figures which were reintegrated systems from the region of outliers with more integration snapshots. The blue curve here is an example of a chaotic system that enters and escapes different MMRs and will continue to do so if integrated longer i.e. not a stable system. The orange curve is an example of a system that migrated directly to a high k MMR only to scatter back to larger periods and capture at a lower k MMR.

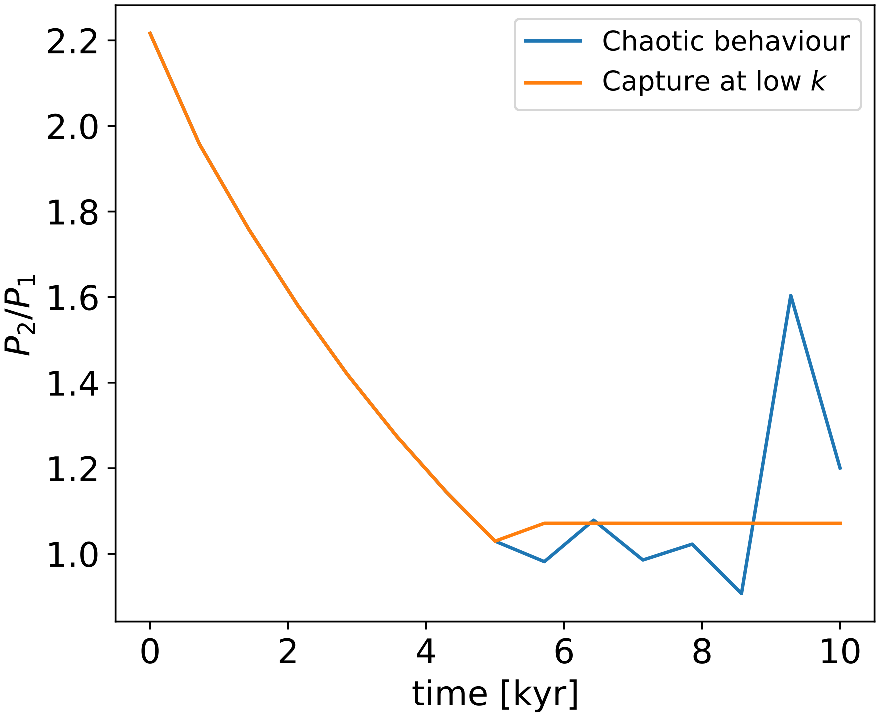

Figure A.3: The evolution of the period ratio for two cases of outliers seen in Figure 4.3, just to show some examples. These outliers behave in the same way in the other 1D plots.

The figure below is another test of outliers to see their behvaiour and confirm that they are chaotic or experience scattering towards larger periods leading to capture at lower k at the end of integration time. These are systems in a small portion of the region of interest in the 2D grid 4.5, reintegrated to be able to save 500 integration snapshots instead of 15 as done for all the plots shown previously. Same as in the previous plot above, we have the blue curve which is a chaotic system where the planets have been captured at a lower

k MMR after scattering to larger periods due to experienced overlap at a higher k MMR. Although, its overall chaotic motion suggests that it might not stay in this MMR with longer integration time and probably would not survive disk removal. The orange curve is a chaotic system that is not captured into any MMR but is near an integer value and not directly unstable by our instability criteria, thus it is averaged to an integer k.

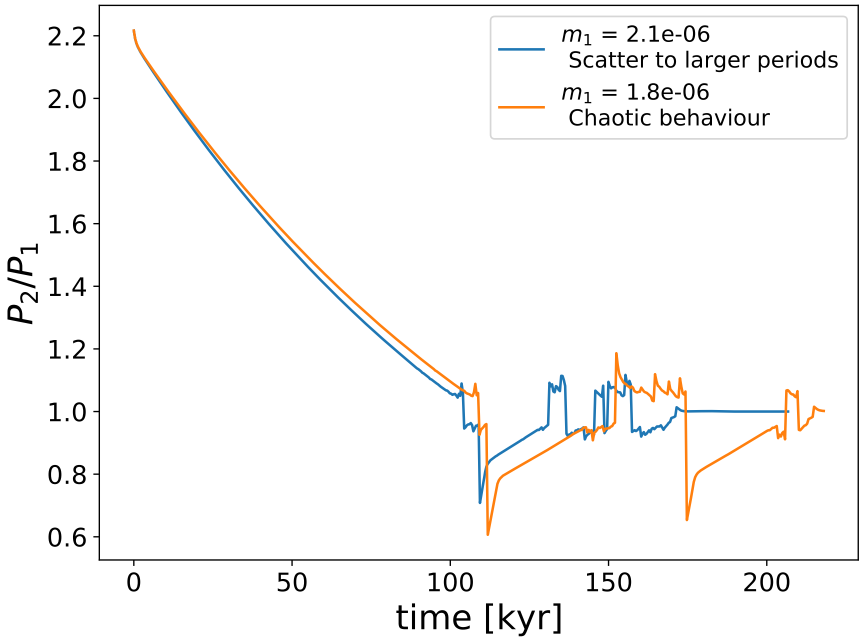

Figure A.4: The evolution of the period ratio for outliers seen on the 2D grid 4.5, to show some examples.

Figure A.5 is similar to the previous figure, but here we have examples of the outliers seen in the 2D grid 4.6. These systems first migrate to high k MMRs as expected, then scatter to larger periods before they again migrate to higher k. The blue and orange curve are more chaotic than the green, they jump back and forth from large to small period ratio. Moreover, all the curves seem to be captured in a lower k MMR, but with small oscillations which suggest that these systems might not remain stable over time or would not survive disk removal. The orange curve ended up in the same k as first attempted, but not until after some scattering from and to larger periods.

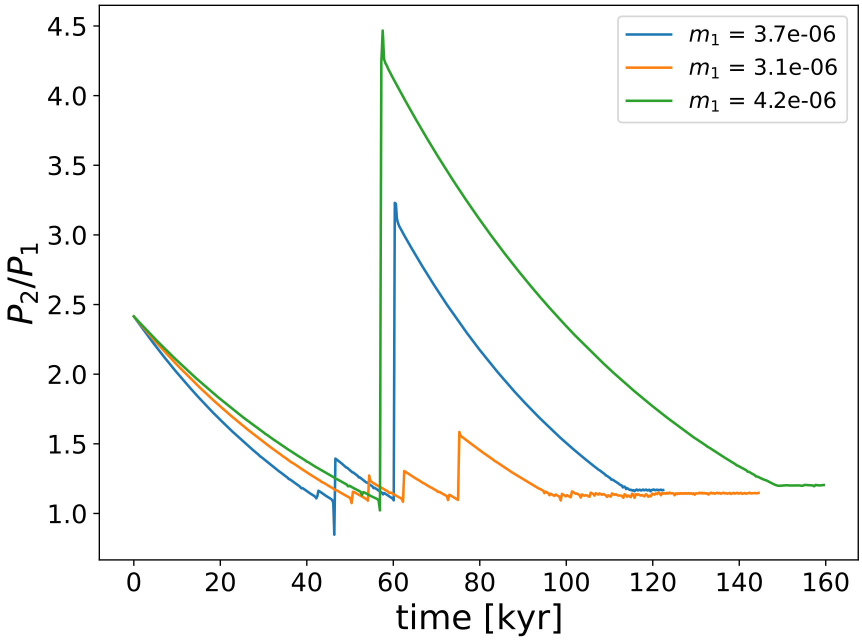

Figure A.5: The evolution of the period ratio for the outliers seen on the 2D grid 4.6 at shorter τ_a or smaller ϵ_p values.

The figure to follow shows examples of outliers in the 2D grid 5.3 in Chapter 5. These systems are found in a small portion of the upper right corner region of outliers, which are Hill stable due to larger period ratio and separation at the end of integration. However, as one can see in this figure the behaviour of these systems is indeed chaotic. If integrated longer they would at a given time not pass the Hill stability criterion. Moreover, as seen on the grid the period ratio of these systems was averaged to an integer k, only because the period ratio was close to a commensurate period ratio at the end of integration time, but it is certain that they are not in a MMR.

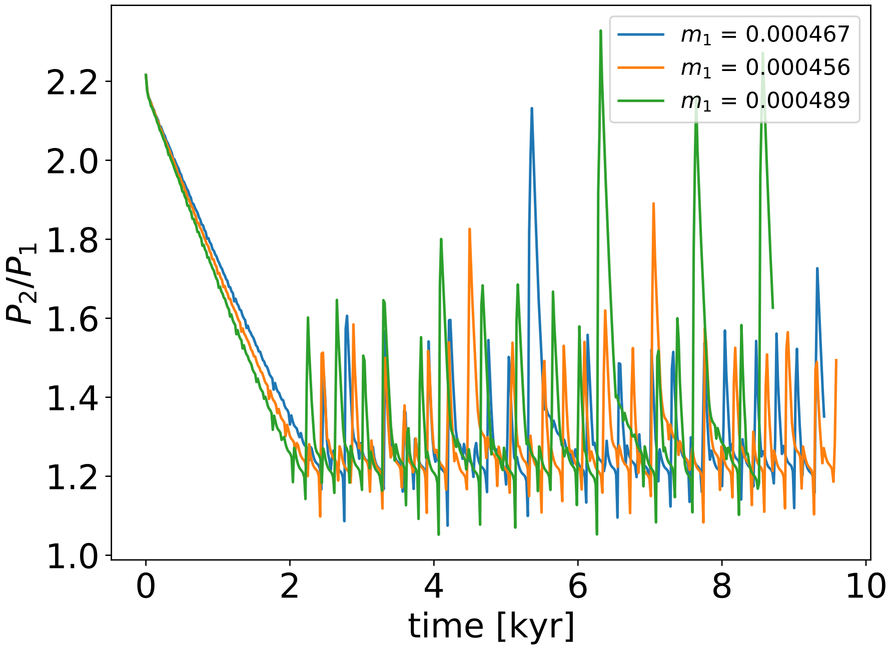

Figure A.6: The evolution of the period ratio for outliers seen on the 2D grid 5.3 in the upper right corner.

The last figure for this section shows examples of the outliers found in the 2D grid 5.5 at various k closer to the Hill instability limit. Here we see that these systems did reach rather high k values and stayed there, but with large oscillations. These systems are thus not stable in a MMR, they just happen to be Hill stable and near a MMR at the end of integration. Therefore, as in other similar cases they passed the stability criterion, and their resonance index was averaged to an integer value. The outliers in the upper right corner, are the same as the outliers found for the same set of combinations of Σ_0 and ϵ_p in the grid 5.3 and shown examples of in Figure A.6.

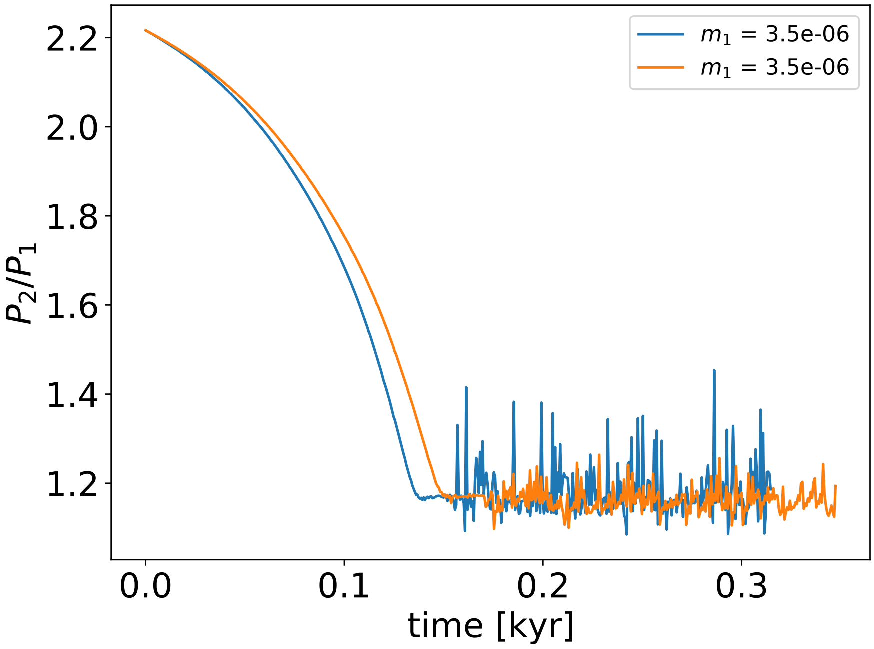

Figure A.7: The evolution of the period ratio for outliers seen on the 2D grid 5.5 at various k close to the Hill instability limit and at higher Σ_0 values.

A.2 Examples of overstability

Figure A.8 presents three examples of systems in the vertical transition between the MMRs 2:1 and 3:2 at long τ_a in Figure 4.6, which indeed exhibit overstability. These systems spend some time in the 2:1 MMR before suddenly escaping it and capturing in the 3:2 MMR.

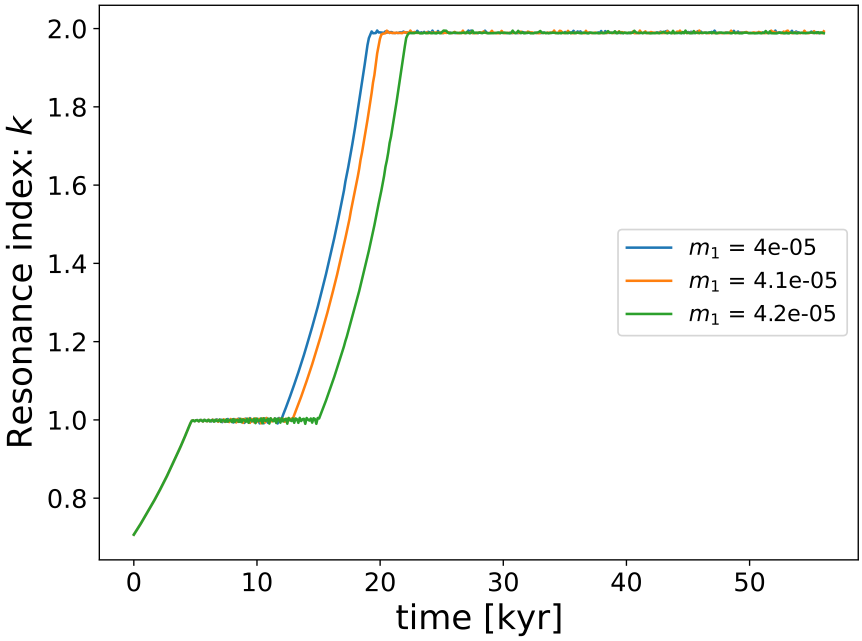

Figure A.8: The evolution of the resonance index over time for the potentially overstable systems at the vertical transition for long τ_a in Figure 4.6.

The figure below shows a test for potentially overstable systems in the grid 5.3. These systems do escape the 2:1 MMR and capture into the 3:2 MMR, similar to the previous example above for constant migration. How fast the escape occurs depends on τ_a, which would explain the small bend to this transition slope.

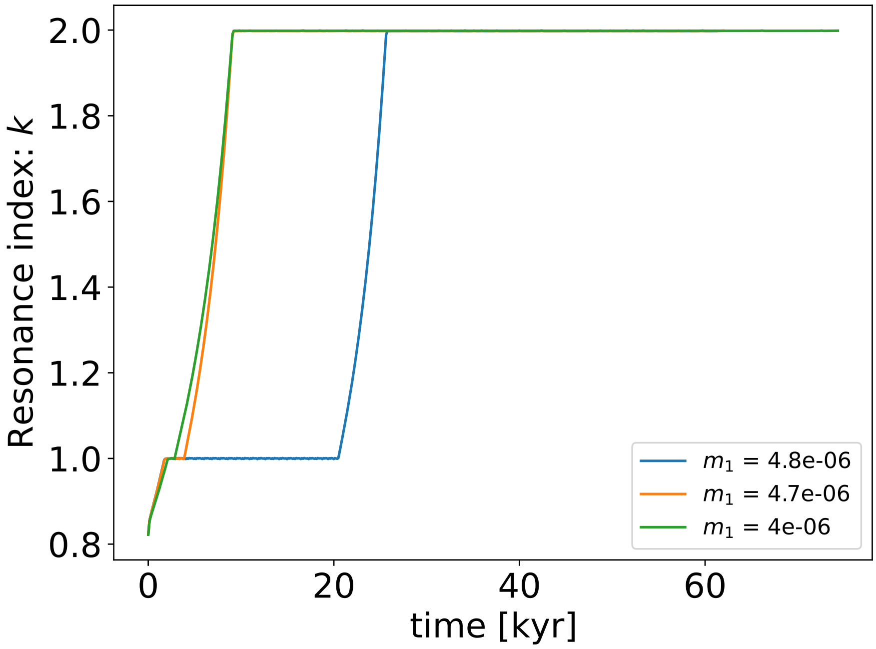

Figure A.9: The evolution of the resonance index over time for the potentially overstable systems at 2:1 MMR in Figure 5.3.

The last figure below shows a test for potentially overstable systems in the grid 5.5. These systems indeed escape through many MMRs before being captured into a higher k MMR. Thus, confirming that these are overstable systems as suspected and that overstability is more pronounced when the planets are of nonequal mass.

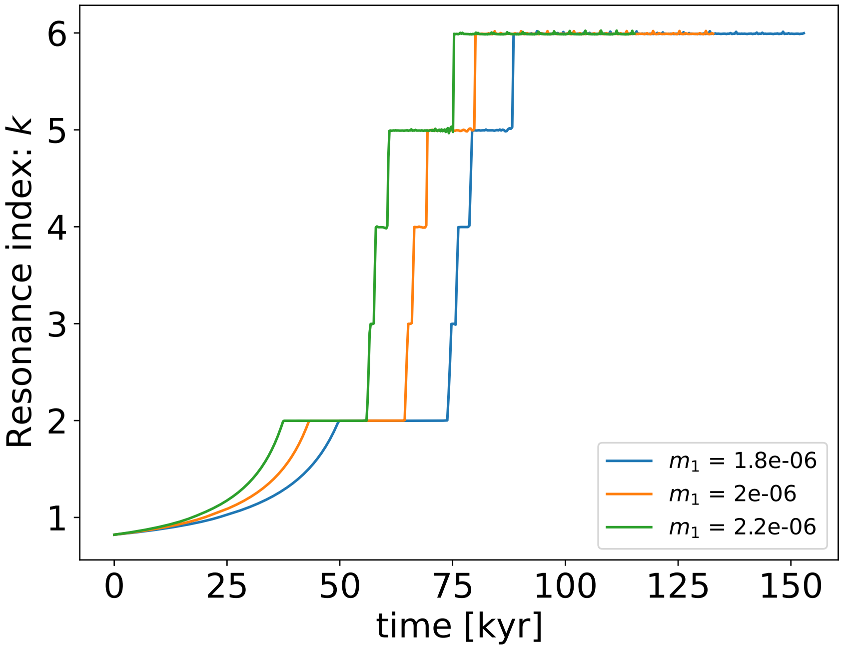

Figure A.10: The evolution of the resonance index over time for the potentially overstable systems at smaller ϵ_p in Figure 5.5.

A.3 Fitting the grids

The figures below show where the different grids have been fitted, starting with the constant setting and the case where the inner planet is fixed at the inner disk edge. The fit was done by first finding the values of ϵ_p and τ_a or Σ_0, where a transition between adjacent MMRs occurs. We do so by finding the largest value of ϵ_p where k transitions and filter the other parameters accordingly. For example, for transition $k = 1$ to $k = 2$ we find the largest ϵ_p where $k < 1.5$, above 1.5 the resonance index is rounded to two. These transitions were then fit using a least-square polynomial fit (`polyfit`) to get the slope at each k, and as such the relationship between ϵ_p and τ_a, or Σ_0 in the case of Type I migration. Of cource, for the transitions at probabilistic capture the largest value of ϵ_p is not on a clear line, since it is a messy region, which also explains why the fit for these k-transitions is less good.

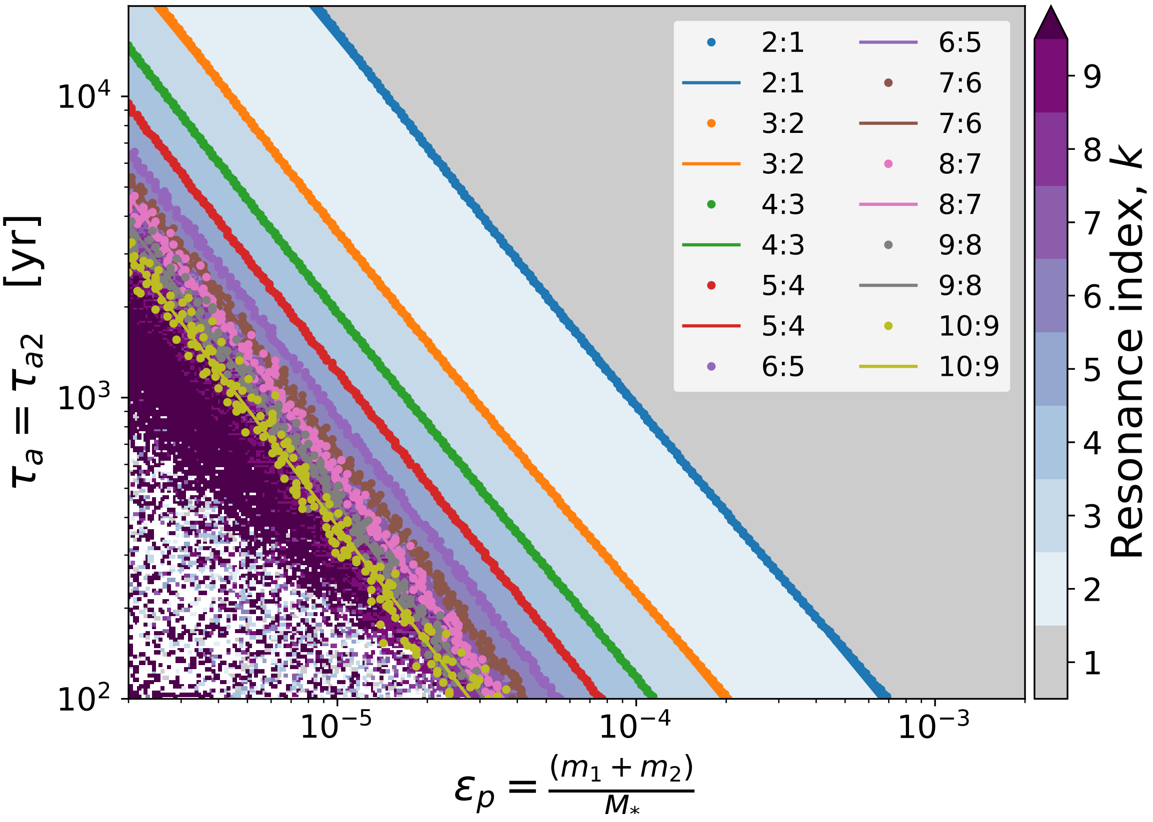

Figure A.11: This figure shows the same grid for the fixed inner planet case as Figure 4.5, but here the fitted lines at each k transition are displayed.

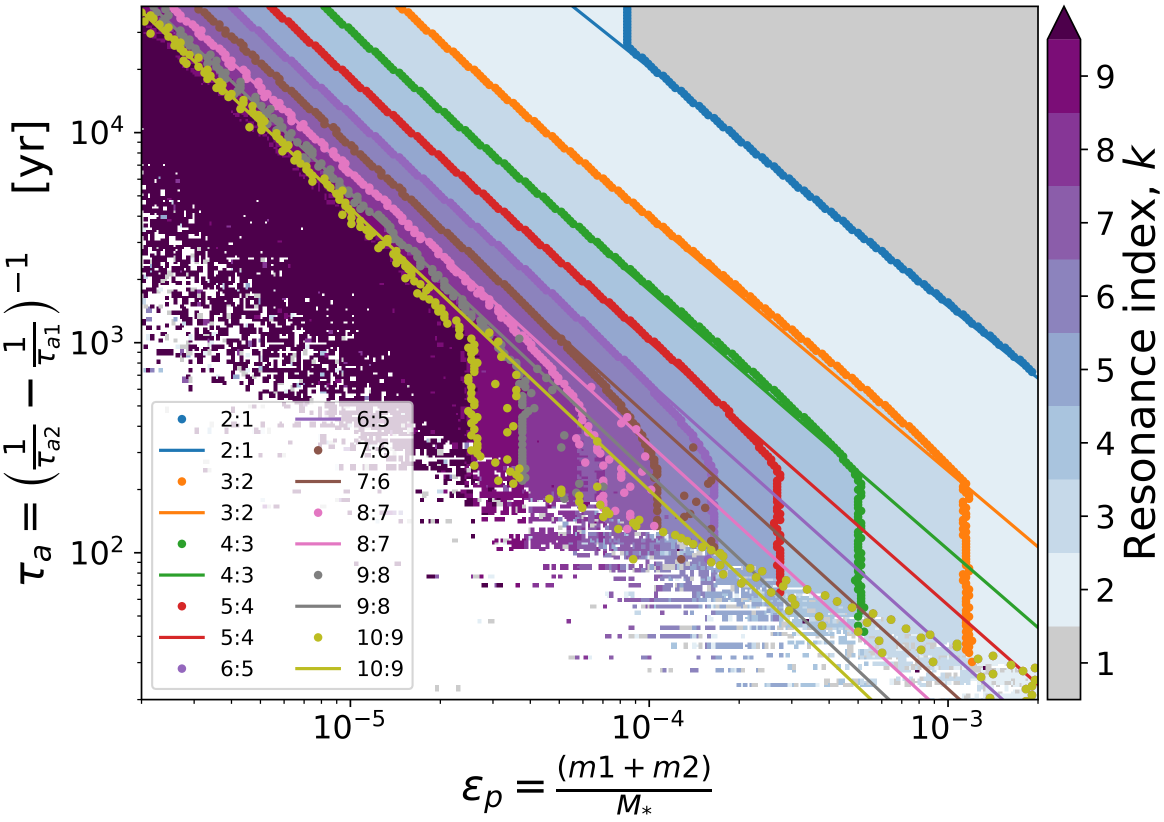

Figure A.12: This figure shows the same grid for migrating planets as Figure 4.6, but here the fitted lines at each k transition are displayed.

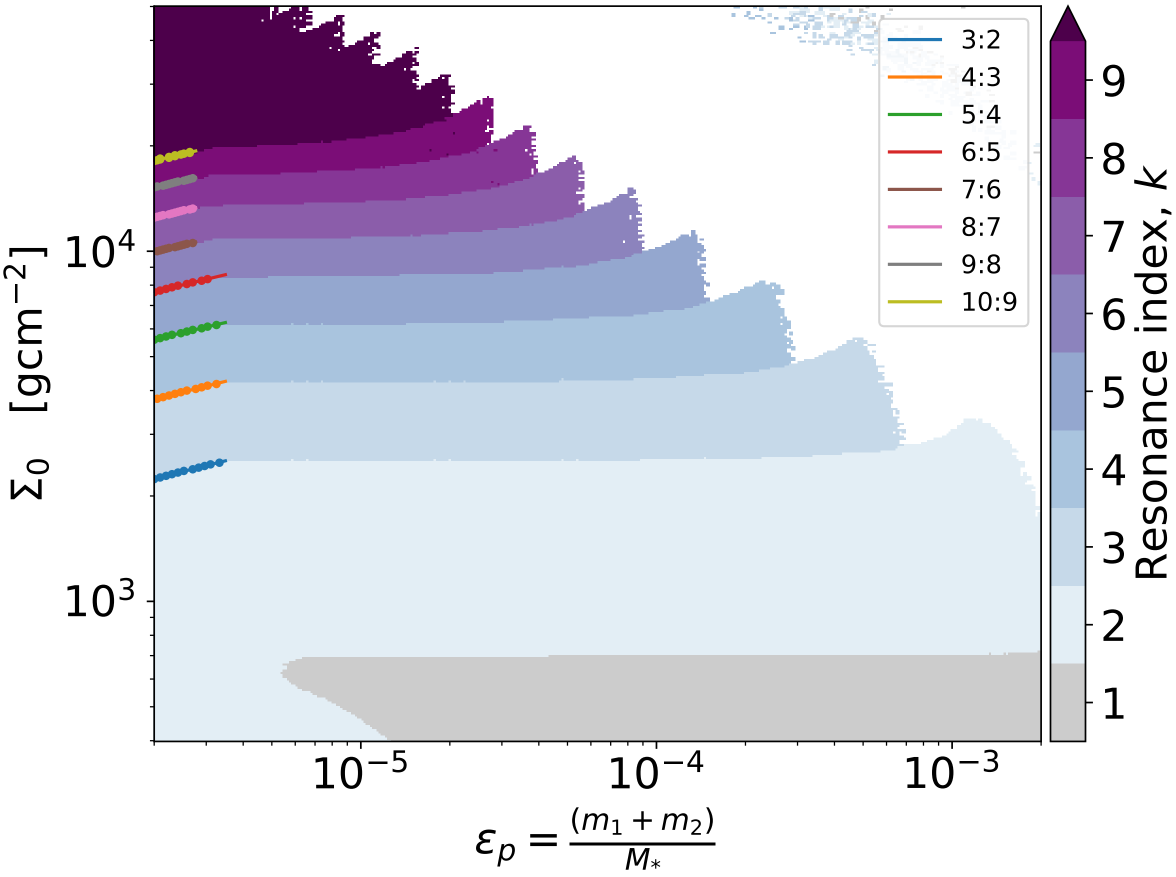

Figure A.13: This is the same grid as in Figure 5.3, but here I have fitted along the slope of positive noon-constant trend for the smallest ϵ_p-values at k transitions.

A.4 Overstability

As a last test it was interesting to see what happens when the outer planet migrates faster, with $\tau_a = 10$kyr and $m_2 = 2m_1$, to see if there are any differences in the case of constant migration. Figure A.14 shows the results of such a simulation.

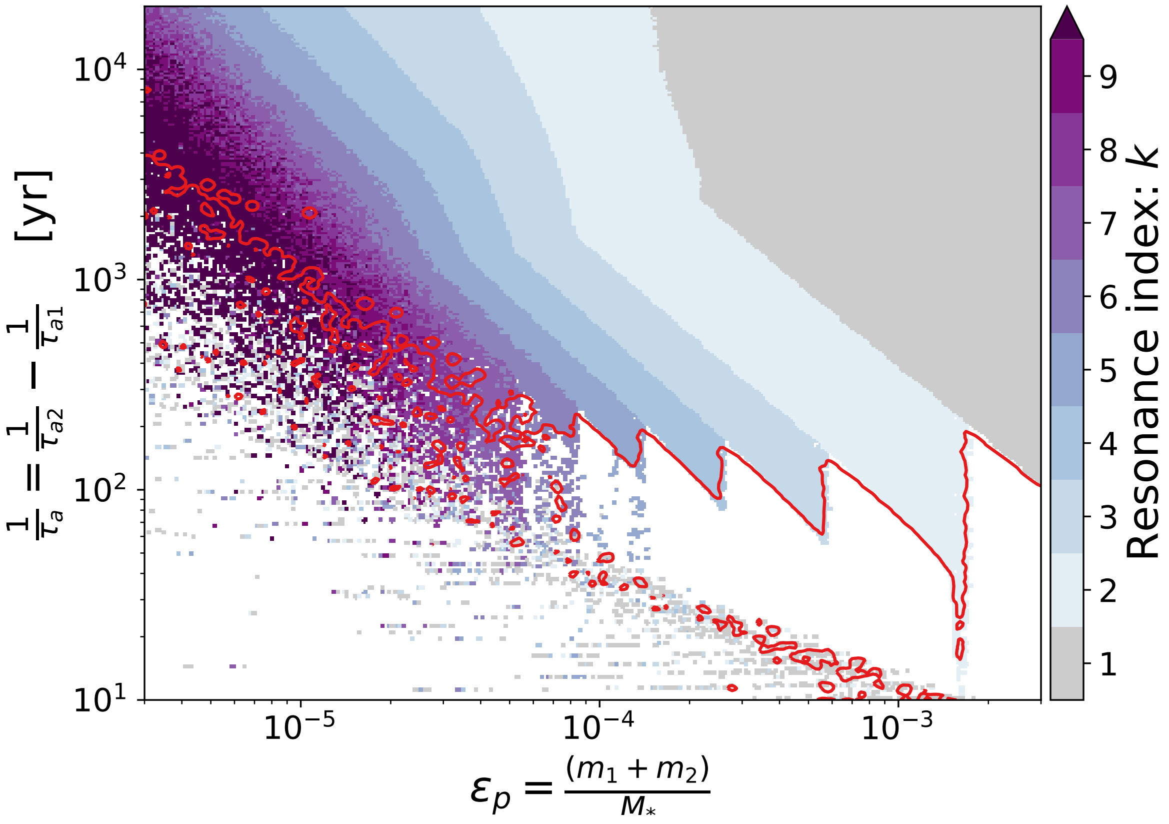

Figure A.14: This 2D grid is similar to Figure 4.6, showing how τ_a affects MMR capture with respect to ϵ_p. But here the outer planet is migrating faster, with the same relative migration.

We directly notice the linear trend between τ_a and ϵ_p, the outliers and the vertical transitions as in the previous grids. The latter two are explained by overlap of resonances and Hill instability in the same way as in Chapter 4. Therefore, here I have just removed those systems directly and marked out the level curves of each criterion as shown in Figure A.14, similar to the 2D grids in Chapter 5.

One difference with both planets moving case in the grid 4.6 is the strange transitions at longer τ_a over a wide range of ϵ_p. These transitions are believed to be systems that become overstable due to the fixed point becoming unstable. That is, for each k there is a mass value where the system becomes overstable and escapes the MMR after some time, even if the adiabatic condition has been satisfied (Deck and Batygin, 2015). That occurs if the planets do not have equal mass, as they do not in this case of migrating planets. This was also seen for the same parameter regime in the Type I migration setting. To investigate this possibility a few systems with selected mass, every 20th ϵ_p-value (40th to 200th), were reintegrated with $\tau_a \approx 2700$ yr for $k > 1$ to before the chaotic zone. The discrete masses are also marked out in Figure A.15, to clearly show their location on the grid.

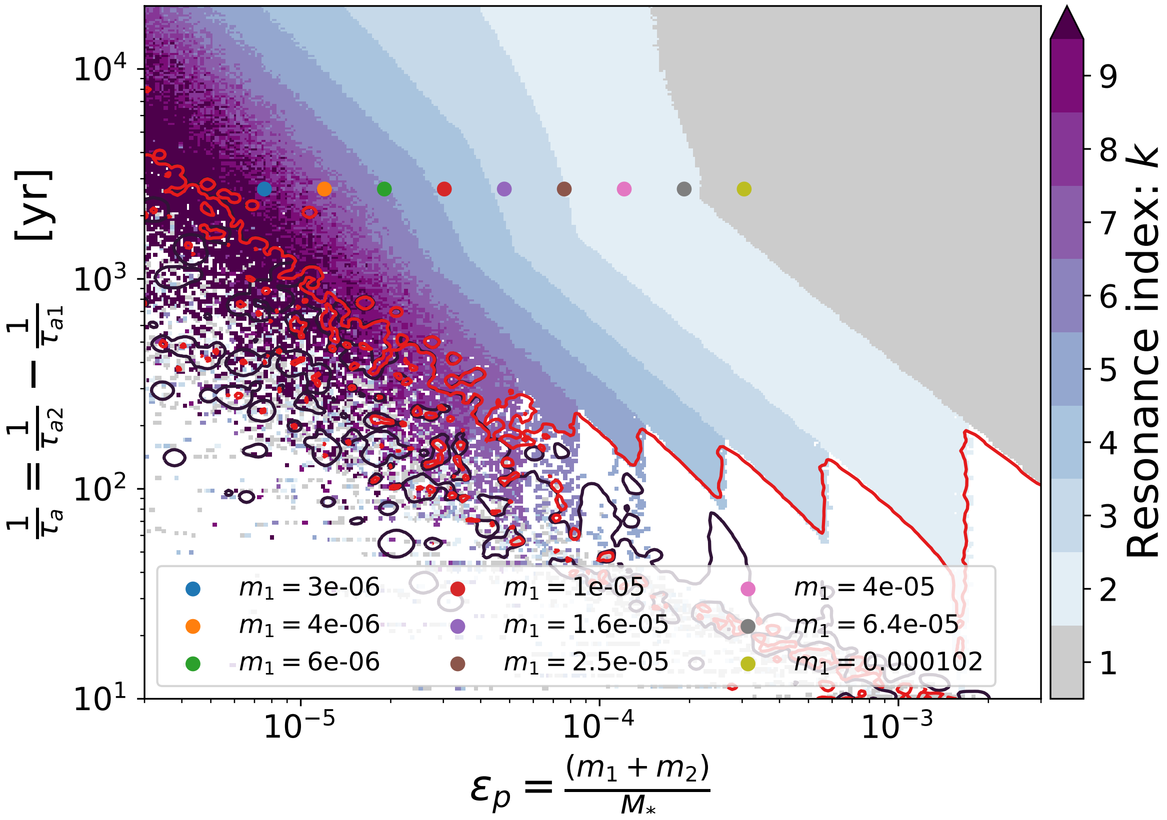

Figure A.15: This 2D grid is same as Figure A.14, but here the masses investigated for overstability are included.

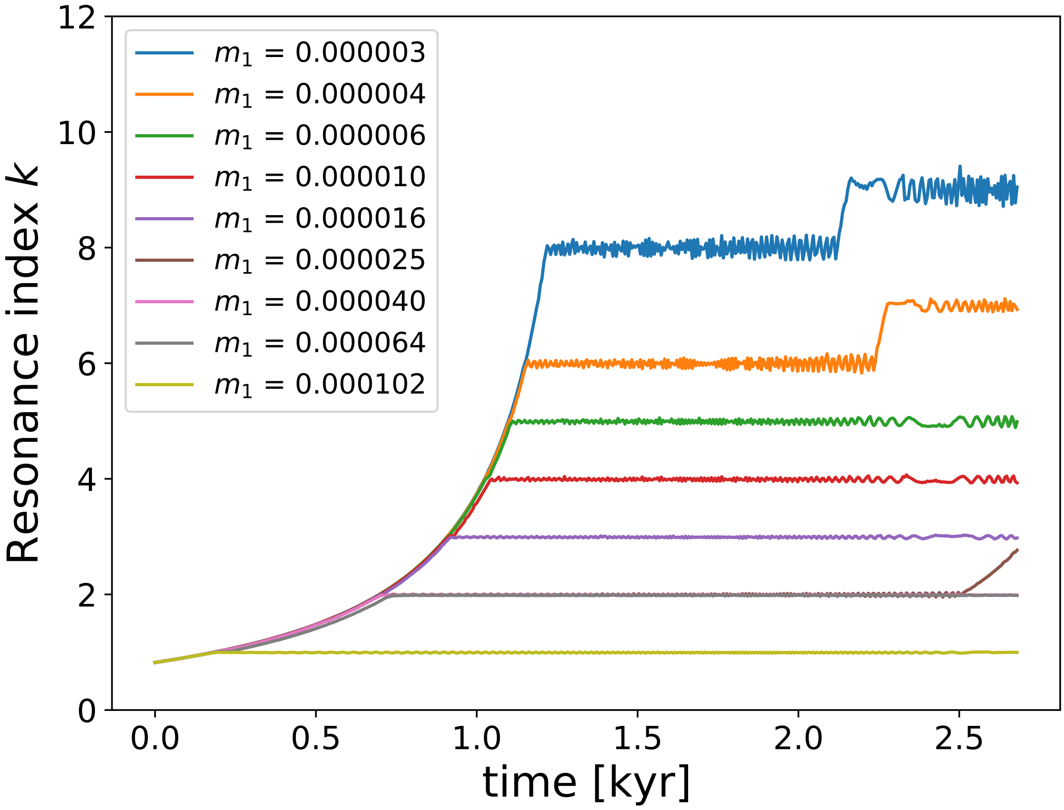

Figure A.16: Evolution over time of the resonance index, continuous period ratio variable, for nine different masses with $\tau_a \approx 2700$. This investigation was done to see if in any case a MMR that is stable is exited due to overstability.

Figure A.16 shows that the systems with the largest masses, which in Figure A.14 fall in the grey area, are not overstable; as expected they are stable in 2:1. Whereas, the systems with masses that fall in the regime of suspected overstability, after some time all escape from the first MMR encountered. Additionally, they seem stable in the last MMR at the end of integration time but might escape that too, as indicated by the small oscillations. Due to overstability the trends these systems follow is naturally not the same as that which the systems not affected by overstability follow. That is, the general linear trend suggesting that the planets usually pass quickly through MMRs if the mass is too small or τ_a is too short to be captured, until a higher k where the adiabatic condition is satisfied, as seen in Figure 4.1. For example, the dark purple, red and green, curves happen to be such cases; the planets migrate directly to $k = 3$, $k = 4$ and $k = 5$ respectively. I have not included a case of smaller ϵ_p values that are in the chaotic zone, because these will be chaotic and not overstable. Another reason why planets would escape a MMR is due to adiabatic growth of eccentricity if the migration proceeds, but this is not true for systems that experience eccentricity damping as is the case here. Thus, it is worth mentioning but not relevant in this project.

In summary, the region at $\tau_a \gtrsim 3000$ is governed by overstable systems similar to the case with planets migrating via Type I migration, Figure 5.5. Overstability is more common for systems near the disk edge and for larger initial surface densities (or lower aspect ratio) (Tanaka and Ward, 2004; Ataiee and Kley, 2021).

Lastly, also fitting the grid as shown in Figure A.18 gives the following results for the coefficients, given in Table A.1. $A_k \approx 1.2$, if we look only at the best fit of the transition into 3:2 MMR. And B_k as function of k in Figure A.17 has a slope of -4.11. This is in general the worst fit, but it is not surprising due to the different trends that overlap and worse resolution. However, the errors of the fits themselves are only slightly larger than in the other cases. Whereas, the error for the slope in A.17 is actually larger than in the other grids presented in the main text, which explains why in this case the value of the k dependency exponent disagrees by much more with the findings in Batygin (2015). This is not concerning though since the main reason is the bad resolution, and difficulty of fitting at the transitions between k as one can see in Figure A.18.

Table A.1: Fitted coefficients of the dependency between τ_a and ϵ_p, for each resonance index up to index $k = 9$, for grid A.14.

Fixed inner planet			
k	MMR	A_k	$\log_{10}(B_k)$
1	2:1	−1.23	−1.12
2	3:2	−1.44	−2.59
3	4:3	−1.58	−3.56
4	5:4	−1.63	−4.06
5	6:5	−1.65	−4.42
6	7:6	−1.66	−4.64
7	8:7	−1.60	−4.48
8	9:8	−1.42	−3.78
9	10:9	−1.30	−3.22

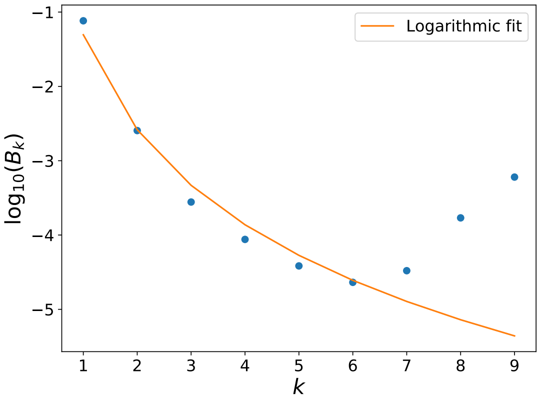

Figure A.17: B_k as function of k, where we get the separation between resonances and how k depends on ϵ_p.

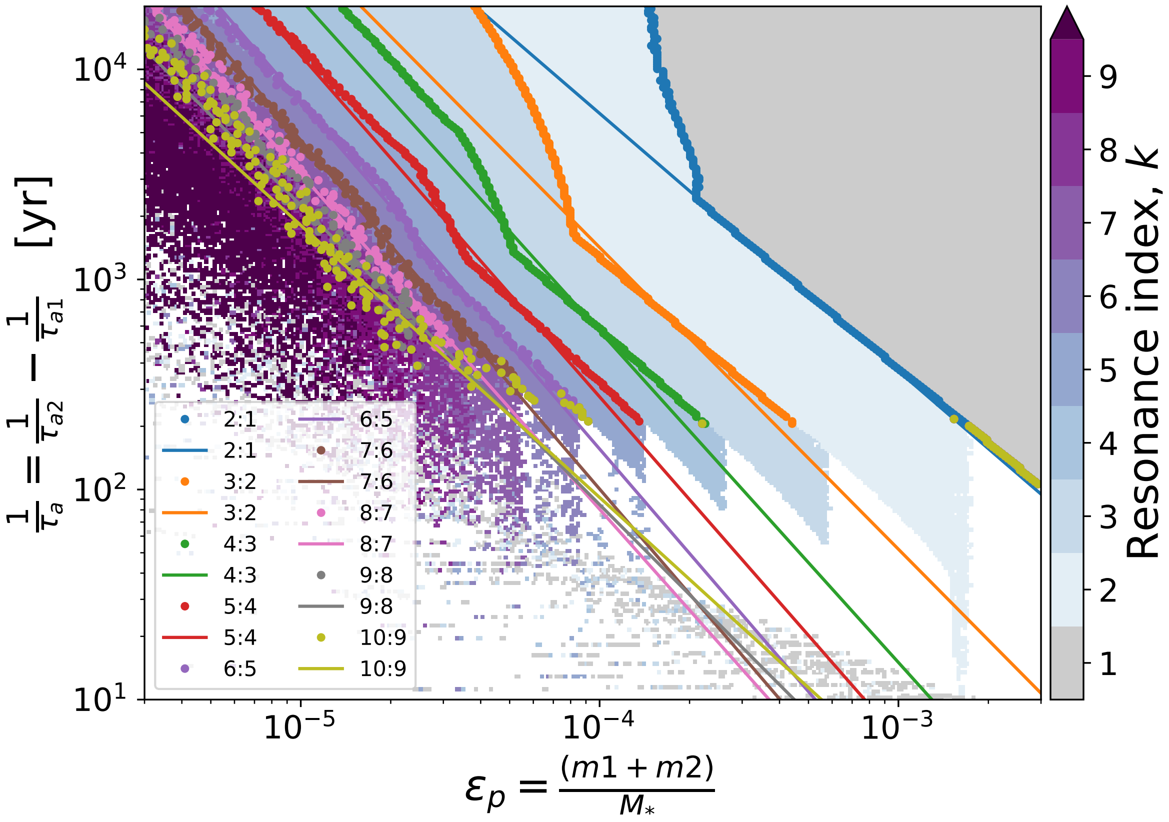

Figure A.18: This figure shows the same grid for migrating planets as Figure 4.6, but here I have fitted along the slope at each k transition.